

**DEVELOPMENT OF THE ULTRASHORT PULSE NONLINEAR OPTICAL  
MICROSCOPY SPECTRAL IMAGING SYSTEM**

A Dissertation

by

ANTHONY CHIEN-DER LEE

Submitted to the Office of Graduate Studies of  
Texas A&M University  
in partial fulfillment of the requirements for the degree of

DOCTOR OF PHILOSOPHY

August 2011

Major Subject: Biomedical Engineering

Development of the Ultrashort Pulse Nonlinear Optical Microscopy Spectral Imaging  
System

Copyright 2011 Anthony Chien-der Lee

**DEVELOPMENT OF THE ULTRASHORT PULSE NONLINEAR OPTICAL  
MICROSCOPY SPECTRAL IMAGING SYSTEM**

A Dissertation

by

ANTHONY CHIEN-DER LEE

Submitted to the Office of Graduate Studies of  
Texas A&M University  
in partial fulfillment of the requirements for the degree of

DOCTOR OF PHILOSOPHY

Approved by:

Chair of Committee,	Alvin T. Yeh
Committee Members,	Andreas Holzenburg
	Kristen Maitland
	Kenith Meissner
Head of Department,	Gerard Coté

August 2011

Major Subject: Biomedical Engineering

## ABSTRACT

Development of the Ultrashort Pulse Nonlinear Optical Microscopy Spectral Imaging System. (August 2011)

Anthony Chien-der Lee, B.S., The University of Texas at Austin

Chair of Advisory Committee: Dr. Alvin T. Yeh

Nonlinear Optical Microscopy (NLOM) has been shown to be a valuable tool for noninvasive imaging of complex biological systems. An effective approach for multicolor molecular microscopy is simultaneous excitation of multiple fluorophores by broadband sub-10-fs pulses. This dissertation will discuss the development of two spectral imaging systems using the principles of nonlinear optical microscopy for pixel-by-pixel spectral segmentation of multiple fluorescent spectra. The first spectral system is reliant on a fiber-optic cable to transmit fluorescent signal to a spectrometer, while the second is based on a spectrometer with an aberration-corrected concave grating that is directly coupled to the microscope. A photon-counting, 16-channel multianode photomultiplier tube (PMT) is used for both systems.

Custom software developed in LabVIEW controls multiple counter cards as well as a field-programmable gate array (FPGA) for 1 Hz acquisition of 256x256x16 spectral images. Biological specimens consisting of multicolor endothelial cells and zebrafish will be used for experimental verification. Results indicate successful spectral

segmentation of multiple fluorophores with a decrease in signal-to-noise ratio in the FPGA-based imaging system.

## ACKNOWLEDGEMENTS

First and foremost, I would like to thank my committee chair, Dr. Yeh, for his support throughout my time here in the biomedical engineering department. He has guided me through a research project which I initially thought to be beyond my abilities.

I would also like to thank Dr. Vitha of the Microscopy and Imaging Center. My results would not have been possible without his assistance in the development of the optical hardware for the second spectral system. His technical knowledge in optics has been invaluable as well.

Last but not least, I would like to thank the rest of my committee, the department faculty, my friends, and family for being here during my Ph.D. and providing an unforgettable experience at Texas A&M University.

**NOMENCLATURE**

CFP	Cyan Fluorescent Protein
CW	Continuous Wave
DAQ	Data Acquisition
DIO	Digital Input/Output
DMA	Direct Memory Access
EC	Endothelial Cell
ECFP	Enhanced Cyan Fluorescent Protein
EYFP	Enhanced Yellow Fluorescent Protein
FPGA	Field-programmable Gate Array
FWHM	Full-width at Half Maximum
GFP	Green Fluorescent Protein
HDL	Hardware Description Language
IPL	Inner Plexiform Layer
KLM	Kerr Lens Mode-locking
NA	Numerical Aperture
NI	National Instruments
NLOM	Nonlinear Optical Microscopy
NOMS	Nonlinear Optical Microscopy System
NOMSIS	Nonlinear Optical Microscopy Spectral Imaging System
NOMSISv1	Nonlinear Optical Microscopy Spectral Imaging System Version 1

NOMSISv2	Nonlinear Optical Microscopy Spectral Imaging System Version 2
PMT	Photo-multiplier Tube
RTSI	Real-time Systems Integration
SHG	Second Harmonic Generation
SNR	Signal-to-noise Ratio
TPF	Two Photon Fluorescence
TTL	Transistor-transistor Logic
UI	User Interface
VISA	Virtual Instrument Software Architecture
YFP	Yellow Fluorescent Protein



## TABLE OF CONTENTS

		Page
ABSTRACT .....		iii
ACKNOWLEDGEMENTS .....		v
NOMENCLATURE .....		vi
TABLE OF CONTENTS .....		viii
LIST OF FIGURES .....		x
LIST OF TABLES .....		xiii
CHAPTER		
I	INTRODUCTION .....	1
II	THEORY OF NONLINEAR OPTICAL MICROSCOPY .....	6
	2.1 Lasers .....	6
	2.2 Nonlinear Optical Signals .....	10
III	NONLINEAR OPTICAL MICROSCOPY SYSTEM .....	15
	3.1 NOMS System Setup .....	15
	3.2 Laser Scanning .....	18
	3.3 Photon Counting .....	21
	3.4 Software Development .....	22
IV	NONLINEAR OPTICAL MICROSCOPY SPECTRAL IMAGING SYSTEM .....	33
	4.1 Fiber-based Spectral Assembly .....	33
	4.2 Software Development .....	36

CHAPTER	Page
4.3	Limitations of Spectral Acquisition ..... 42
4.4	Directly-coupled Spectral Assembly..... 43
V	FIELD-PROGRAMMABLE GATE ARRAYS..... 46
5.1	Field-programmable Gate Array Basics..... 46
5.2	Software Development..... 48
VI	EXPERIMENTAL VALIDATION ..... 56
6.1	Optical Collection Efficiencies ..... 56
6.2	Noise Removal ..... 62
6.3	In Vitro Imaging of an Angiogenic System ..... 64
6.4	Spectral Analysis of Multicolor Zebrafish..... 67
VII	CONCLUSION AND RECOMMENDATIONS..... 72
	REFERENCES..... 74
	APPENDIX A ..... 78
	APPENDIX B ..... 131
	APPENDIX C ..... 139
	VITA ..... 149

## LIST OF FIGURES

FIGURE	Page
2.1 Schematic of a standard laser .....	7
2.2 Energy diagram of absorption and emission .....	8
2.3 KLM setup for a pulsed laser .....	10
2.4 Quantum well diagram for two photon excitation fluorescence .....	11
2.5 Calculated $T(\omega)$ for a 10-fs (blue) and 100-fs (red) pulse.....	13
2.6 Integrated two-photon power spectrum versus pulse duration.....	14
3.1 NOMS system setup.....	16
3.2 NOMS microscope setup .....	17
3.3 3D mouse tail tendon.....	18
3.4 Laser scanning patterns using (a) raster and (b) triangle waveforms.....	19
3.5 Mouse tail imaging using (a) raster and (b) triangle scanning patterns .....	20
3.6 Counter timing example .....	22
3.7 NOMS state chart .....	24
3.8 State machine template.....	25
3.9 Stage initialization code .....	26
3.10 UI event handler example.....	27
3.11 Open channels state S2.....	28
3.12 Acquire data state S3.....	30
3.13 Analyze data state S4 .....	31

FIGURE	Page
3.14 Save data state S5 .....	32
4.1 NOMSISv1 system setup .....	34
4.2 NOMSISv1 optical setup with (a) schematic of the changes made within the microscope and (b) spectrometer setup.....	35
4.3 Channel activation.....	37
4.4 Data processing .....	38
4.5 Wavelength selection and graph configuration .....	39
4.6 Nonlinear Optical Microscopy Spectral Imaging System interface.....	41
4.7 NOMSISv2 spectrometer setup.....	44
5.1 FPGA trigger detection .....	49
5.2 FPGA counting channels.....	50
5.3 FPGA data storage .....	52
5.4 Reading from FIFO .....	55
6.1 System comparisons .....	60
6.2 Noise removal .....	63
6.3 Collected (a) pre-processed and (b) post-processed data .....	64
6.4 TPF spectra for CFP, GFP, and YFP .....	65
6.5 Spectral analysis of endothelial cells .....	66
6.6 Spectral graph of zebrafish eye .....	68
6.7 Discrete masking of the zebrafish eye.....	69
6.8 Spectral subtraction to isolate (a) EYFP and (b) ECFP .....	70
6.9 Autofluorescence of wild-type zebrafish .....	70

FIGURE	Page
6.10 Multicolor zebrafish eye expressing ECFP and EYFP with a view (a) of the whole eye and (b) zoomed into the retina .....	71

**LIST OF TABLES**

TABLE	Page
4.1 Dispersion of Horiba concave grating.....	45
5.1 Pulse transitions.....	51
6.1 Experimental configurations with calculated SNR. ....	61

## CHAPTER I

### INTRODUCTION

Nonlinear Optical Microscopy (NLOM) systems provide a non-invasive method of imaging dynamic and complex biological processes over a period of time. Using femtosecond pulses, nonlinear signals can be collected from endogenous and exogenous markers by means of two photon excitation and second harmonic generation. Two-photon excitation spectra can be calculated as

$$T(\omega) = \left| \int_0^{\infty} E\left(\frac{\omega}{2} + \Omega\right) E\left(\frac{\omega}{2} - \Omega\right) d\Omega \right|^2, \quad (1.1)$$

where  $E(\omega)$  represents the pulse electric field in the frequency domain and  $\Omega$  is the iterative variable for integration across all frequency components. By overlapping the two-photon excitation spectra with the molecular two-photon absorption of an excitable fluorophore  $\gamma(\omega_0)$ , two-photon transition probability can then be represented as a proportional relationship,

$$\Gamma \propto \int_0^{\infty} \gamma(\omega_0) \left| \int_0^{\infty} E\left(\frac{\omega_0}{2} + \Omega\right) E\left(\frac{\omega_0}{2} - \Omega\right) d\Omega \right|^2 d\omega_0, \quad (1.2)$$

where  $\hbar\omega_0$  is the transition energy. Two-photon transition probability represents the likelihood of nonlinear signal generation. Therefore, maximizing this value is highly desirable to enhance NLOM signals.

---

This dissertation follows the style of Optics Express.

The calculation shows that optimizing two-photon transition involves broadening of the spectral profile for the pulses, which occurs as the pulse is shortened in the time domain. The condition can be met with pulses in the fs range, typically 100 fs for standard NLOM systems. As pulse duration further decreases towards a magnitude of 10, spectral bandwidth increases respectively because of the Fourier relationship. This broadening allows for simultaneous excitation of multiple fluorophores, a characteristic which does not exist in 100 fs pulses [1,2]. When applied to an NLOM laser pulsed at sub-10 fs, the spectral bandwidth is broadened to ~125 nm, allowing for a time-efficient spectral imaging modality with no detrimental effect to image quality [1]. By using detectors and optical filters, fluorescent and second harmonic signal can be transferred and separated in imaging software to display individual components of a biological sample[3]. Ultimately, NLOM imaging provides a fast and efficient way to generate two and three dimensional images quickly and noninvasively.

The usage of ultrashort pulses also benefits from an improvement in depth-based NLOM imaging. Three-dimensional NLOM imaging depth is typically limited by the generation of out-of-focus fluorescence at the surface of the sample as laser power intensity is increased [4,5]. When the sample's fluorescent signal degrades as the laser focuses into the sample due to scattering, the fluorescence intensity at the focus approaches that of the fluorescence intensity generated at the surface. This limitation exists for transform-limited 100 fs pulses used with most NLOM lasers. By introducing dispersion and generating a sub-10 fs chirped pulse with an ultrashort-pulse laser, the



highly concentrated fluorescent signal at the focus is expected to significantly reduce depth limitation of NLOM imaging due to the dispersive characteristics of ultra-short pulses [6].

Present-day NLOM systems typically use individual photomultiplier tubes set at specific wavelengths to detect fluorescent signal. In order to collect signal at different wavelengths, either the optical filter needs to be adjusted manually or an additional detector needs to be used in conjunction. Additionally, these systems use a laser with ~100 fs pulse width which have a much narrower excitation spectrum [1]. Tuning the laser to a new central wavelength is an additional requirement for spectral imaging [7]. The continuous tuning and calibration required for these systems makes spectral experimentation on living specimen a difficult and time-consuming task. Although useful for systems containing one or two fluorescent specimen, the information provides little insight to the emission spectra of samples containing multiple fluorophores. In order to understand the true chemical and biological composition of specimens, the system should detect signal with respect to emission wavelength using an ultrashort pulse laser. The ability to distinguish between spectral characteristics of specimens with closely related emission spectra is also highly desired.

The solution is to design a multi-channel detection system using a detector capable of acquiring signal across a large spectrum, an ultrashort pulse laser allowing for broadband excitation, and National Instruments (NI) hardware to perform high-speed data

acquisition. The primary goal of the dissertation is the design of a high-speed 16-channel NLOM system using a sub-10 fs laser.

In order to begin development of the 16-channel imaging system, a two-channel imaging system must be designed capable of acquiring images matching that of the lab's current imaging software. Images acquired with this software could then be used as a reference for verification of the new imaging system. Known as the Nonlinear Optical Microscopy System (NOMS), the system is a fully functional 2-channel imaging system capable of acquiring a 3-dimensional stack of images automatically. The data may be saved in binary format for ease of analysis using third-party programs such as MATLAB. Additionally, NOMS can open saved files to review images that have been previously acquired. After completion, the system can be expanded for 16-channel multispectral NLOM imaging, resulting in the Nonlinear Optical Microscopy Spectral Imaging System (NOMSIS).

LabVIEW is the chosen form of programming for NOMSIS development because of its ability to communicate between the hardware and software with ease. Unlike standard text-based programming languages such as C and Java, LabVIEW uses a graphical programming language known as "G" which follows a dataflow programming architecture. Graphical programming is much like writing out an algorithm on paper. By laying out functional "blocks" which perform a specific task and connecting them with "wires," the software can directly convert the layout to machine code for execution.

This leads to a quick and easy solution to tasks which would normally take many lines of typed code. Additionally, graphical programming allows for multiple starting points where data execution begins. Computers equipped with multi-core processors can automatically take advantage of this implementation and load-balance the instructions between multiple threads. Because text-based programming languages execute using the top-to-bottom approach, writing a program to take advantage of multi-core processors is much more difficult. LabVIEW usage has grown significantly in the years as it proves capable of creating complex programs to solve modern engineering problems [8-10].

After development, verification and comparison of the systems are performed.

Experimental datasets verify spectral delineation of multiple fluorophores, as well as provide an insight to the optical collection efficiencies of the designs.

## CHAPTER II

### THEORY OF NONLINEAR OPTICAL MICROSCOPY

Background and theory behind the principles of operation of the system is discussed in Chapter II. Principles of laser operation are reviewed in Section 2.1, and theory behind nonlinear optical signals is discussed in Section 2.2.

#### 2.1 LASERS

Due to the necessity of using lasers in NLOM, understanding their basic principles is essential. The term laser was initially derived as an acronym from *Light Amplification from Stimulated Emission of Radiation*. Stimulated emission, or highly organized emission of light, is the key concept in the term which leads to the generation of laser light.

A typical laser is generated from a highly reflective cavity containing two mirrors, one fully reflective while the other is semi-reflective. A gain medium, the Ti:Al<sub>2</sub>O<sub>3</sub> crystal, within the cavity is excited via a pump source. The pump can vary from sources such as an external light, a secondary laser, or an electrical current. For our lab, the pump source is another laser, an Nd:YVO<sub>4</sub>. As seen in Figure 2.1, the pump source excites the molecules from the gain medium into a higher energy level through absorption.

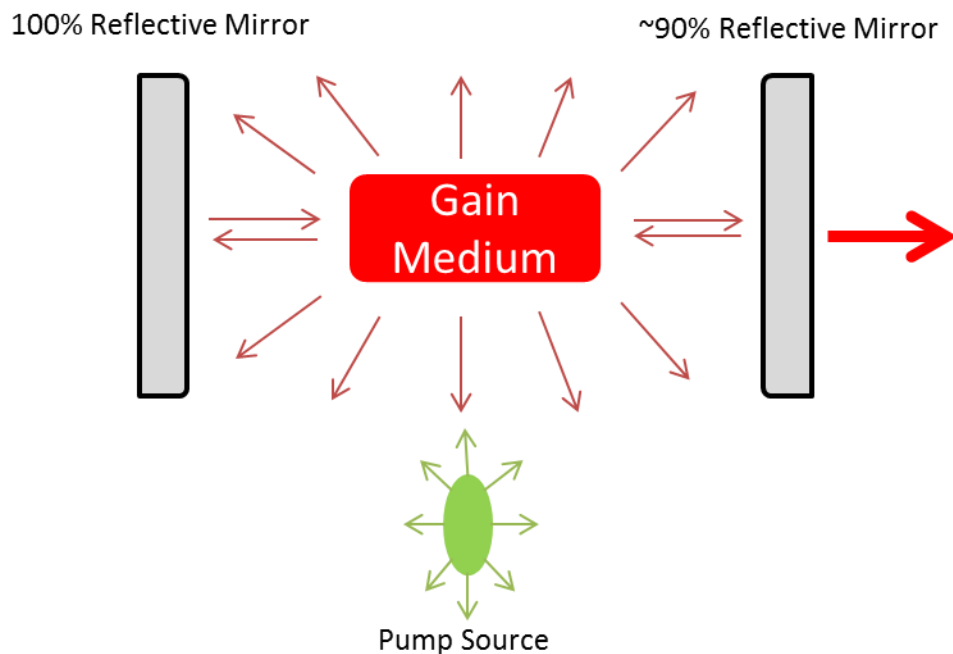


**Figure 2.1. Schematic of a standard laser.**

When the molecules return to ground state, spontaneous emission of a photon of lesser energy is generated as illustrated in Figure 2.2. This photon is at 800 nm for our system. Spontaneous emission lacks a uniform direction; however a few of the photons will be emitted at a direction parallel to the cavity. This means the photon will bounce back from the mirror and return to the gain medium, allowing for what is known as stimulated emission. Stimulated emission takes place when an emitted photon collides with an electron already in an excited state. The electron will fall to ground state and generate an additional photon. Without the mirrors within the cavity, stimulated emission would cause a quick depletion of excited molecules.

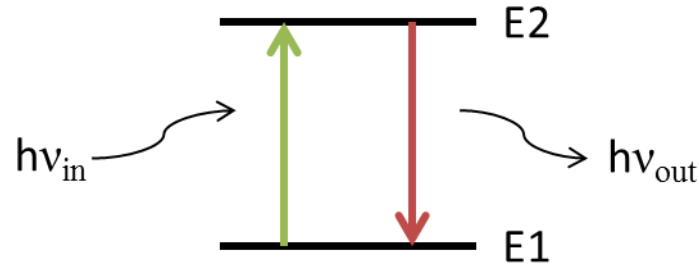


**Figure 2.2. Energy diagram of absorption and emission.**

Population inversion, a state when more molecules are in the excited state than ground state, exists when the mirrors in the cavity reflect the photons to propagate a continuous cycle of stimulated emission. Finally, lasing occurs as the amplified light within the cavity exits through the semi-reflective mirror.

After establishing a continuous wave (CW) laser, we need to understand the mechanism known as mode-locking which generates a pulsed laser. The bandwidth of a laser pulse in the time domain is the Fourier transform of the spectral width in the frequency domain. Because of the inverse relationship between the time and frequency domains, a pulse with the broadest possible spectrum, or the greatest possible number of cavity modes, will also have the shortest possible time duration. The phases for each of the lasing cavity modes are locked. Constructive interference between the superposition of cavity modes creates a high-intensity pulse, whereas destructive interference cancels out the energy, allowing for a series of pulses.

Our lab uses a passive form of mode-locking known as Kerr Lens Mode-locking (KLM), where the Ti:Al<sub>2</sub>O<sub>3</sub> crystal acts as an artificial saturable absorber [11,12]. KLM relies on the nonlinear index of refraction of the medium, Ti:Al<sub>2</sub>O<sub>3</sub>, for mode-locking. The refractive index change is described as

$$n(I)=n_0+n_2I, \quad (2.1)$$

where  $n_0$  is the linear refractive index,  $n_2$  is the second-order medium-specific refractive index, and  $I$  is the intensity of the pulse. This creates a Kerr lens within the medium, allowing for self-focusing of the laser beam. The self-focused beam possesses a much narrower beam diameter than that of the CW laser.

The optical setup for the KLM laser is summarized in Figure 2.3. Adjustment of the curved focusing mirror M3 changes the beam to favor pulsed mode over CW mode. Once optimized for pulsed mode, mirror M1 is toggled to induce mode-locking, and the beam path transitions from CW shown in blue, to pulsed mode shown in red. The green beam represents the pump laser, Nd:YVO<sub>4</sub>.

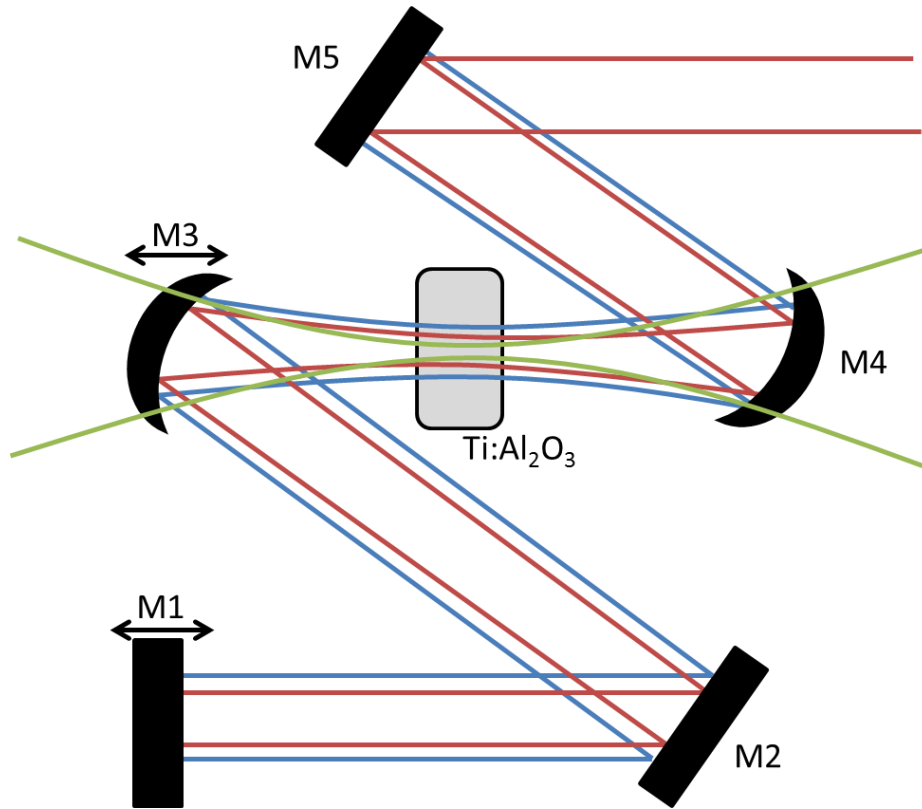


Figure 2.3. KLM setup for a pulsed laser.

## 2.2 NONLINEAR OPTICAL SIGNALS

The polarization of high-intensity pulses interacting with electric fields can be represented as

$$P_i = \chi_{ijk}^{(1)} E_j + \chi_{ijk}^{(2)} E_j E_k + \chi_{ijk}^{(3)} E_j E_k E_l + \dots, \quad (2.2)$$

which is the Taylor series expansion for the  $n^{\text{th}}$  order susceptibility of the sample,  $\chi^{(n)}$ .

Linear microscopy, such as one-photon confocal fluorescence, can be described by the  $\chi^{(1)}$  term. The remaining higher order  $\chi$  describes nonlinear effects. NLOM traditionally



relies on two principle theories: second harmonic generation arising from the  $\chi^{(2)}$  term, and two-photon fluorescence (TPF) arising from the  $\chi^{(3)}$  term.

Two-photon excitation microscopy relies on the simultaneous absorption of two photons and generation of fluorescent emission through molecular relaxation. As illustrated in Figure 2.4, a molecule absorbs two photons of low energy which satisfies the transition requirements to go from ground state E1 to excited state E2. The resulting output from intramolecular vibrational relaxation is an emission photon with energy greater than a single absorbed photon. For our system, the absorption will arise from the 800 nm ultrashort pulses.

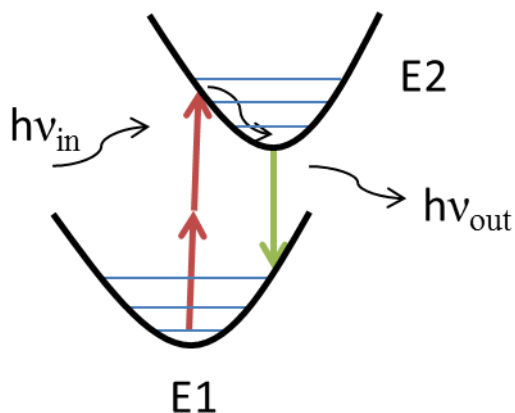


**Figure 2.4. Quantum well diagram for two photon excitation fluorescence.**

Second harmonic generation (SHG), also known as frequency doubling, arises from the unique nature of a specimen. Nonlinear interaction between the laser and a sample of non-centrosymmetric structure allow for effective combination of two incident photons,

generating a new photon of twice the energy and frequency, and at half the wavelength. Specimens which possess centrosymmetric structure have no SHG signal because of the non-zero second harmonic coefficient. SHG microscopy is prevalent in many biological studies, such as the cornea of the eye and collagen protein, both of which naturally possess the unique qualities required for SHG.

While TPF signal only originates from the molecular relaxation shortly after absorption, SHG signal is only generated when the pulse is actively hitting the sample. Because both TPF and SHG signals are derived from the same theory for nonlinear optics, no additional modification is needed in a nonlinear optical imaging system as long as the detection wavelengths are within range.

Nonlinear signal generation can be calculated as a relation to pulse duration,  $T_p$ . Using Equation 1.1, two-photon power spectrum  $T(\omega)$  is calculated using a duration-dependent Gaussian approximation for a transform-limited pulses as shown in Figure 2.5. Using 10 and 100 fs pulses for comparison, we observe a much broader waveform for the two-photon transition energy in the 10 fs pulse. The data indicates that the usage of a shorter pulse significantly increases two-photon excitation due to the increased bandwidth.

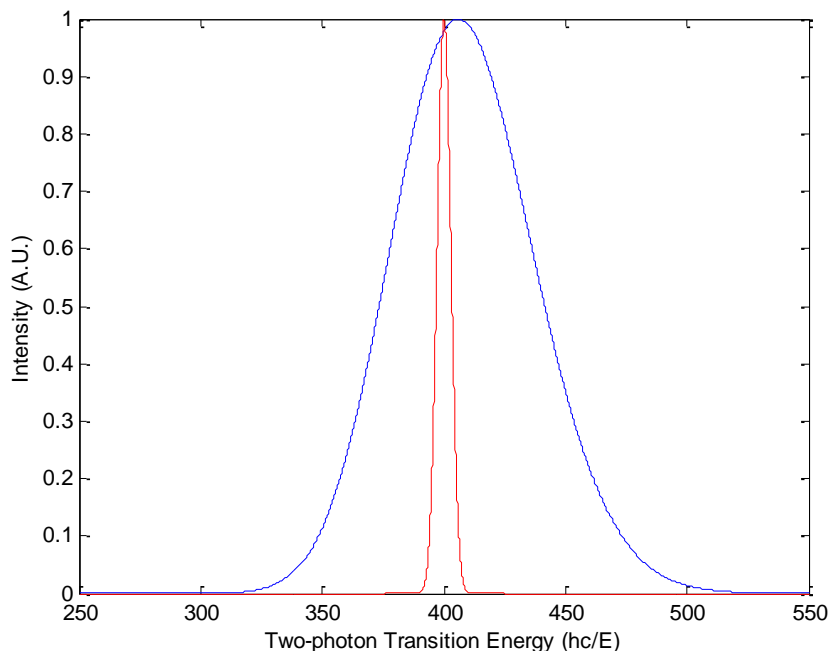


**Figure 2.5. Calculated  $T(\omega)$  for a 10-fs (blue) and 100-fs (red) pulse.**

The conclusion can be further validated by plotting two-photon power spectrum for multiple pulse durations. Shown in Figure 2.6, we observe a slope of -1 which indicates that two-photon transition probability will increase proportionally with  $1/T_p$ . At this point Equation 1.2 is limited by the pulse, thus shortening of pulse duration is ideal for maximizing nonlinear signals. However there are limitations as transition probability is not constricted to just the pulse, but also the molecular two-photon absorption.

Assuming a transform-limited infinitely short pulse, two-photon excitation becomes infinitely broad in the time domain. Because the molecular absorption profile is still Gaussian, the fluorophore is unable to absorb all frequency components of the laser.

This causes the transition probability of Equation 1.2 to yield diminishing returns as pulse duration becomes shorter [6].

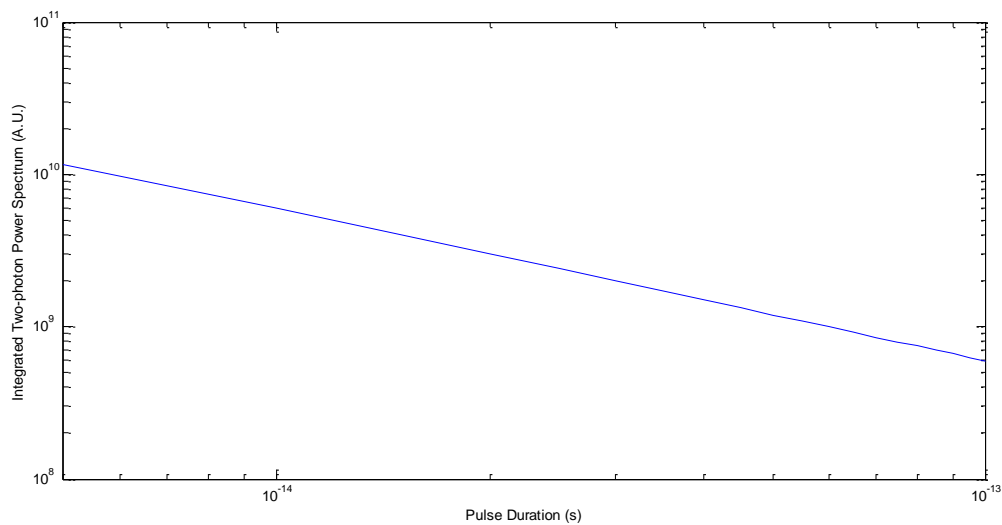


**Figure 2.6. Integrated two-photon power spectrum versus pulse duration.**

## **CHAPTER III**

### **NONLINEAR OPTICAL MICROSCOPY SYSTEM**

With the proper knowledge of NLOM principles, we can now develop an imaging system known as the Nonlinear Optical Microscopy System (NOMS). NOMS system development is discussed in Section 3.1. Section 3.2 describes the technique to control scanning mirrors. Section 3.3 discusses the photon counting procedure, and software development is examined in Section 3.4.

#### **3.1 NOMS SYSTEM SETUP**

NOMS hardware setup is illustrated in Figure 3.1. The laser first passes through dispersion compensation optics. Dispersion compensation mirrors are necessary to create negative dispersion in order to cancel out the positive dispersion induced by the microscope optics. This pre-compensation ensures a high peak power at the focus and prevents a loss in excitation and detection efficiencies. A neutral density filter (not shown in figure) can be placed anywhere along the laser pathway to attenuate power. The laser then passes through computer-controlled dual-axis galvanometers, which are further discussed in Section 3.2. Upon entering the microscope, the laser passes through a telescope which guides the laser to be imaged onto the back focal aperture of the objective lens as shown in Figure 3.2. The laser passes through the microscope, and signal from the sample returns through a dichroic short pass mirror. The mirror is

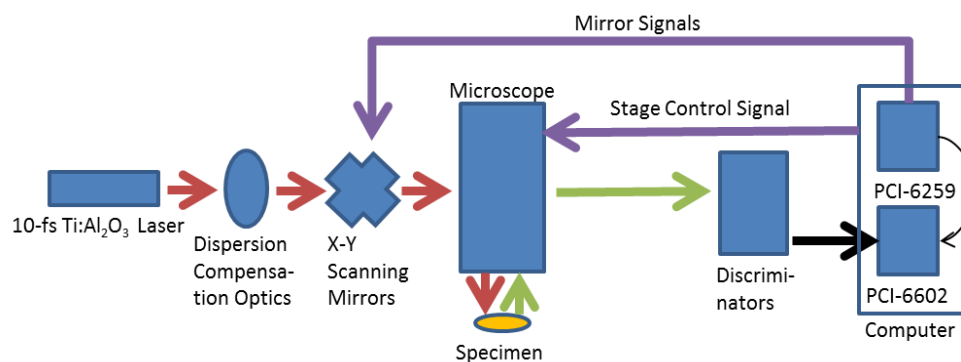


**Figure 3.1. NOMS system setup.**

chosen to be a 635 nm short-pass in order to minimize back-scattering of the laser into the detection optics, as desired signal NLOM signal for the system is not greater than 635 nm. The signal passes through a tube lens and two long-pass dichroic mirrors. These mirrors separate incoming signal into two channels, one channel for optical signal shorter than 430 nm, and one pathway for signal shorter than 620 nm but greater than 430 nm. Each channel enters selective band-pass mirrors which isolate desired wavelength pass-bands. Finally, focusing lenses are used for entrance into the photomultiplier tubes (PMT). The PMTs convert the optical signals into electrical signals and transfers the data into discriminators which further translate the electrical signal into transistor-transistor-logic (TTL) pulses. These pulses are counted and detected by the computer, as described in Section 3.3, finally rendering a working image. A stage-control signal sent by the computer allows for automated imaging in the z-dimension. The usb-controlled signal instructs the stage to change position with a precision up to  $1/20^{\text{th}}$  of a  $\mu\text{m}$ . By changing the focus of the sample and collecting a

series of images, a 3-dimensional image can be generated from a stack of 2-dimensional data.

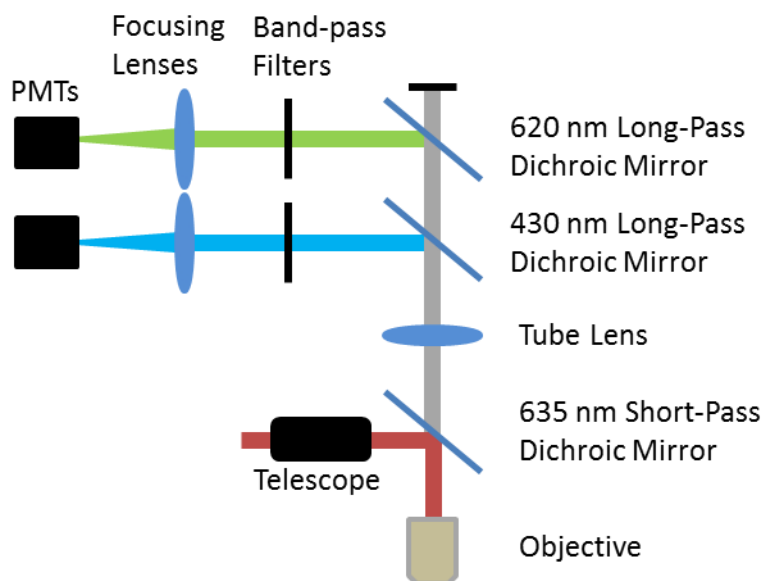


**Figure 3.2. NOMS microscope setup.**

Experimental validation is performed by acquiring SHG signal from a mouse tail tendon. Mouse tail tendons are an excellent sample to use for testing purposes in NLOM due to the ease of generating second harmonic signal. The tendon is placed under the objective and SHG signal is collected by NOMS. Using sawtooth scanning and voltage-guided mirrors, NOMS collects and saves a stack of 2-d images. Post-processing of the stack creates a working figure for the tendon as illustrated in Figure 3.3. The data concludes that NOMS is a capable method for non-invasive image generation of biological samples.

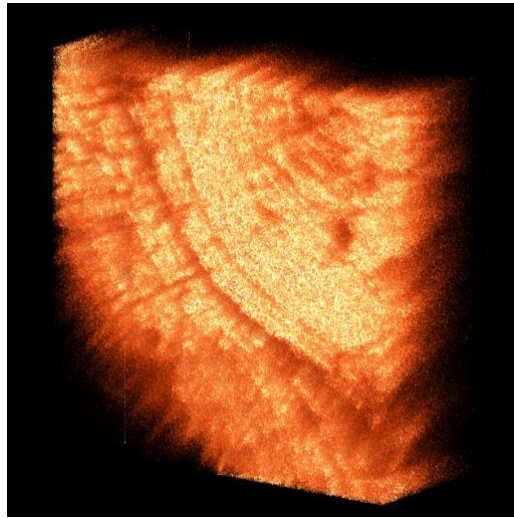


**Figure 3.3. 3D mouse tail tendon.**

### **3.2 LASER SCANNING**

Laser-guided scanning is a standard for modern optical imaging systems. In order to ensure the laser passes across all desired portions of a sample, various scanning patterns are used. For 2-dimensional X-Y galvanometer scanning, the most common forms are raster and triangle scanning. Raster scanning, shown in Figure 3.4(a), is a series of line scans originating from the same side and moving across the sample's X-axis. In Figure 3.4(b), triangle scanning moves the laser in reverse direction on every other line.



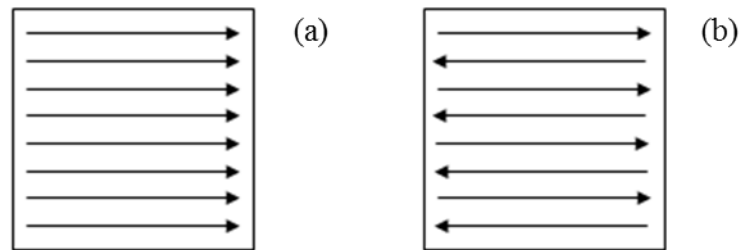


**Figure 3.4. Laser scanning patterns using (a) raster and (b) triangle waveforms.**

The scanning mirror galvanometers, are sensitive to electrical voltage, within a range typically  $\pm 15\text{V}$ . As the voltage changes, the mirrors move to corresponding positions with high accuracy and precision. This allows for voltage-based control to generate the desired scanning waveforms. Because guidance of the laser is limited to two mirrors, these scanning patterns need to be simulated as one continuous flow. The x-axis scanning is created using voltage generation of a sawtooth waveform for raster scanning, and a triangle waveform for triangle scanning. The y-axis scanning pattern is always a sawtooth waveform.

Although both patterns should theoretically generate the same images, minute differences still exist when data is acquired. Raster scanning of the tendon generates signal distortion at the left and right sides of the image as seen in the Figure 3.5(a). This is due to the sudden transition of the mirror's x-axis to return to the original location while signal collection and image processing continuously occurs. The issue can be reduced by increasing the scanning time which allows the mirror to move at a slower pace. As seen with the usage of triangle scanning in Figure 3.5(b), this distortion issue is

virtually eliminated. Because triangle scanning has the x-axis continue from the end of each line rather than returning to the original location, mechanically-induced distortion of the image is not an issue. However upon closer examination of the triangle-scanned tendon, there exists a slight discontinuity in the fibers which can be described as “jagged edges.” The issue comes from the small variations in the scanning pattern arising from the reverse-scanning of the sample on every return segment of the triangle waveform pattern. This discontinuity prevents images from being as clear as the datasets acquired from raster-scanning. Ultimately, a slow, raster-based scanning pattern would be the ideal form of laser-scanning for system development.

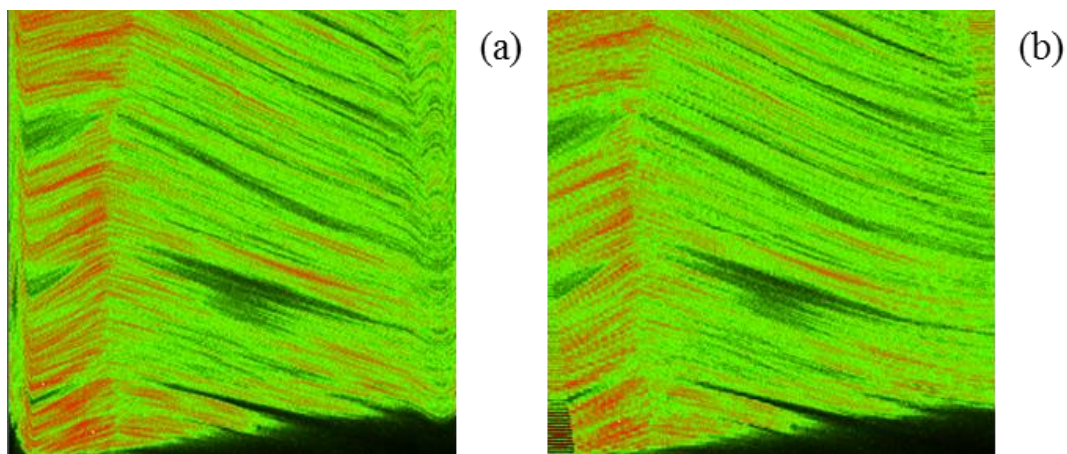


**Figure 3.5. Mouse tail imaging using (a) raster and (b) triangle scanning patterns.**

### 3.3 PHOTON COUNTING

In photon counting, signal from the sample is picked up by a PMT which creates a spike in its output signal. This output signal is in the form of an electrical current which is read by a preamplifier/discriminator (F-100T, Advanced Research Instruments Corp.). The discriminator generates a TTL pulse whenever the electrical current from the detector exceeds a manually specified threshold setting. The TTL pulses are counted directly and correspond to the intensity of a pixel on a grayscale intensity graph. Proper signal triggering and timing algorithms must be understood in order for photon counting to properly generate images. Figure 3.6 is an example of photon counting which is properly triggered and interpreted. By generating an internal clock signal corresponding to the desired scanning speed, it can act as both a starting trigger signal as well as a pixel divider. Although not shown on the figure, the X-Y scanning mirrors are also triggered with this signal. As photons are picked up and pulsed through the discriminator, the hardware will then count the pulses and store them within memory for image processing. The integer counts arrive into the computer as a series of arrays. NOMS rearranges the arrays as they arrive to create a final 256x256 image.

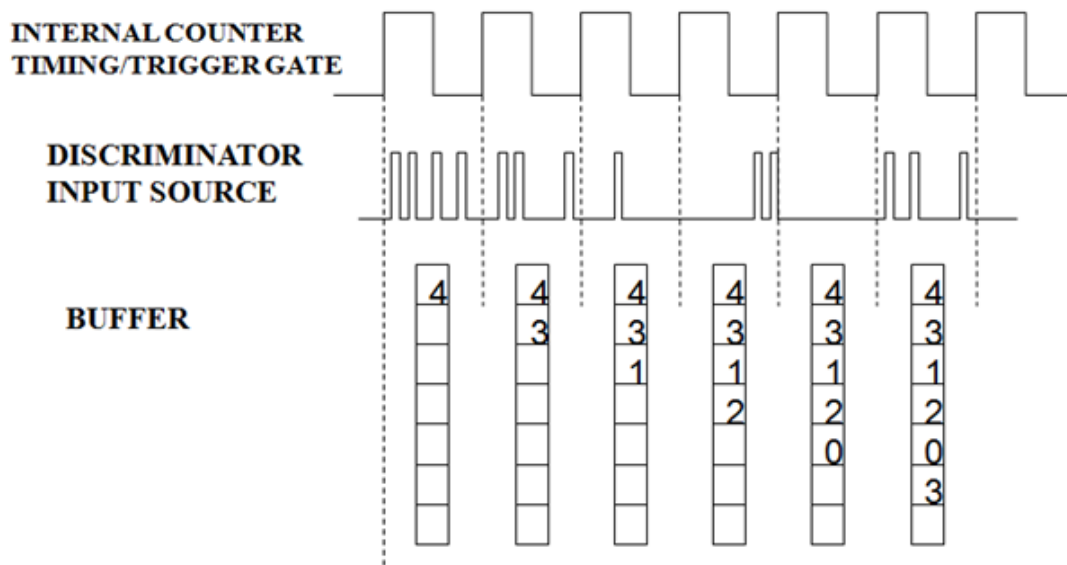


**Figure 3.6. Counter timing example.**

### 3.4 SOFTWARE DEVELOPMENT

NOMS takes advantage of two standardized LabVIEW programming algorithms: the Standard State Machine, and the User Interface (UI) Event Handler. The Standard State Machine operates on a process of dividing a program into various subsections, each of which runs a particular segment of code. The computer traverses between each subsection, known as a *state*, based on particular conditional events within the code or actions taken by the computer operator. Ultimately, the State Machine will loop back to the beginning to start once more, or end up at a STOP state which instructs the program to terminate. The UI Event Handler is the second LabVIEW programming algorithm used for NOMSIS. This algorithm is used when a program requires user input among numerous controls on the front panel, each of which performs a unique task. When a

task is completed, the program control returns to wait for the next UI command. If illustrated as a state machine, the UI Event Handler would be a single state which continuously returns to itself upon completion. By integrating both the Standard State Machine and the User Interface Event Handler algorithms, complex programs can be efficiently created within the LabVIEW software.

NOMS programming summary is divided into seven states as seen in Figure 3.7.

Initialization state S0 opens communication with the LUDL Electronics' MAC5000 stage controller for the microscope. In order for 3-dimensional data acquisition to work properly, NOMS must get a successful pingback from the stage controller indicating successful data initialization. This allows NOMS to send commands directly to the stage which controls vertical movement along the Z-axis. If the response has failed, the user can choose to check the connections and retry the initialization. The second option would be to continue with stack acquisition disabled, in which case NOMS will disable 3-dimensional imaging processes. This initialization state only needs to be run once during the operation of the software, which is why the state diagram does not return to the S0 state upon completion.

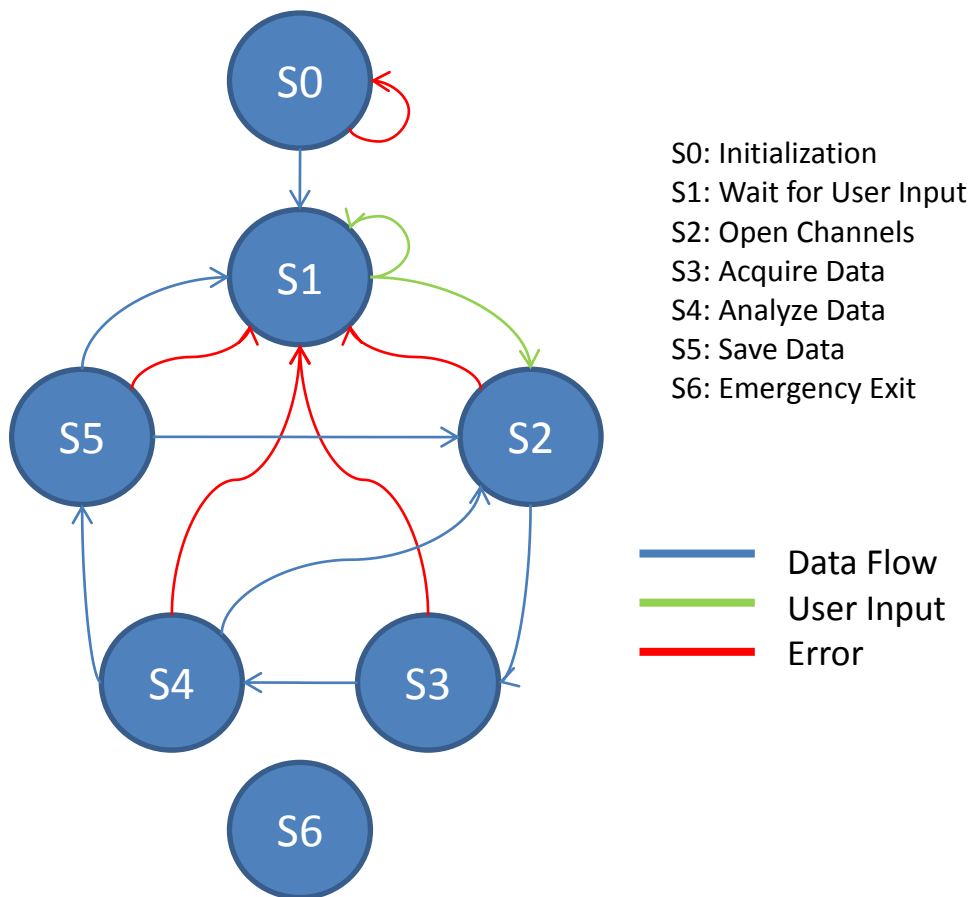


**Figure 3.7. NOMS state chart.**

Complete code for NOMS is too extensive for placement within text, so it may be referenced within Appendix A. Only the essential portions of NOMS for each state will be discussed within the chapters. LabVIEW implementation of the state machine architecture is simplified by usage of a template built into the software. By nesting a case structure within a while loop, a shift register may be used to determine transition states. Figure 3.8 shows the most basic layout of the State Machine template, with the Initialize state, corresponding to S0, set to execute first. When developing NOMS, the stage initialization driver provided by LUDL Electronics is placed inside the case

structure. LabVIEW then updates the next transition state and loops back to begin the next state.

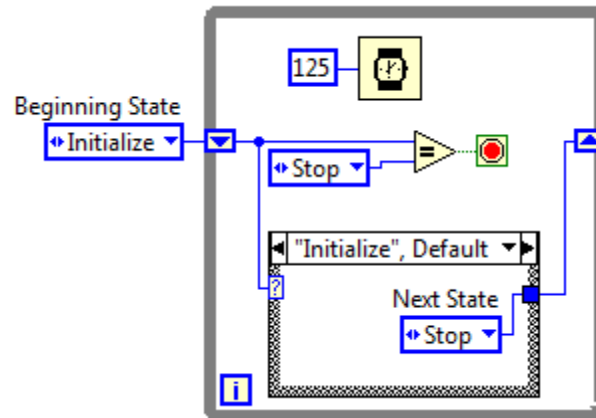


**Figure 3.8. State machine template.**

Implementation of state S0 requires the usage of drivers provided from LUDL Electronics. These drivers allow for the integration and detection of the microscope stage into the NOMS software. Figure 3.9 shows the code, which is used as a sub-vi, and placed inside the Initialize state of NOMS. By making use of NI Virtual Instrument Software Architecture (VISA), artificial drivers can be programmed for third-party hardware and become recognizable by LabVIEW.

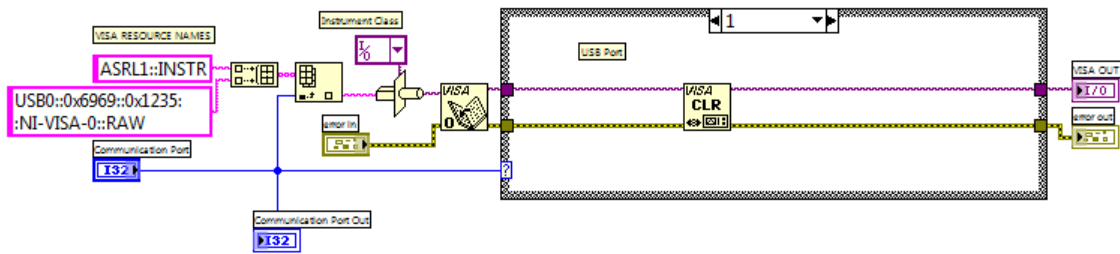


**Figure 3.9. Stage initialization code.**

The code uses the hardware address generated by NI VISA for USB-based initialization of the mechanical stage of the microscope. If the software executes without error, NOMS will transition to state S1. Failure to execute properly will allow the user to check for errors and retry, or simply continue without stage-controlled imaging.

User Interface state S1 is the primary state where user-controlled operations are controlled. This state checks which controls on the interface are being interacted with by the user. The majority of interactions will result in a small change to the front panel, such as “graying” out different locations, followed by the state returning to itself. Implementation is performed by using an Event Structure. The event structure is used to execute code when certain user-based events are executed. Figure 3.10 shows a simple UI Event Handler example if the “stop” button is pressed on-screen. The corresponding action is to stop the while loop. For NOMS, once the state detects the “Start” button being pressed, the computer proceeds to state S2.



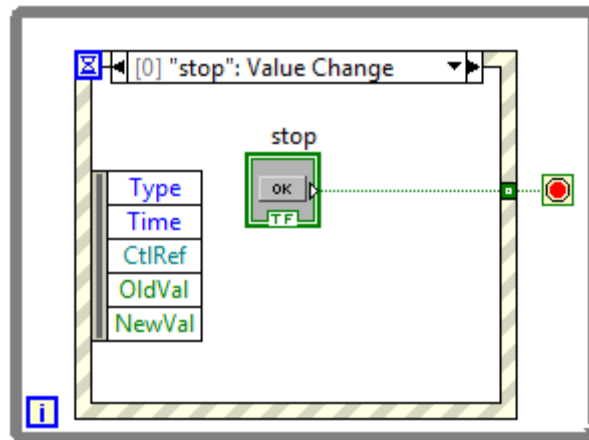


**Figure 3.10. UI event handler example.**

Open Channels state S2 is where the software directs the hardware to allocate specific resources to begin imaging according to the parameters transferred from S1. It then calculates the proper gate/trigger frequency for the DAQ card as well as generates the proper X-Y waveforms for the mirrors according to the specified scanning speed. This state also tells the on-board counters to activate and prepare for pulse counting. Figure 3.11 illustrates the necessary code for “Gate Initialization” which sets the parameters for the pixel clock, “Mirror Signal Output Generation” which creates the proper sawtooth amplitude and frequency waveforms for the scanning mirrors, and “Channel 1” which initializes the first counter channel for preparation in TTL pulse counting.

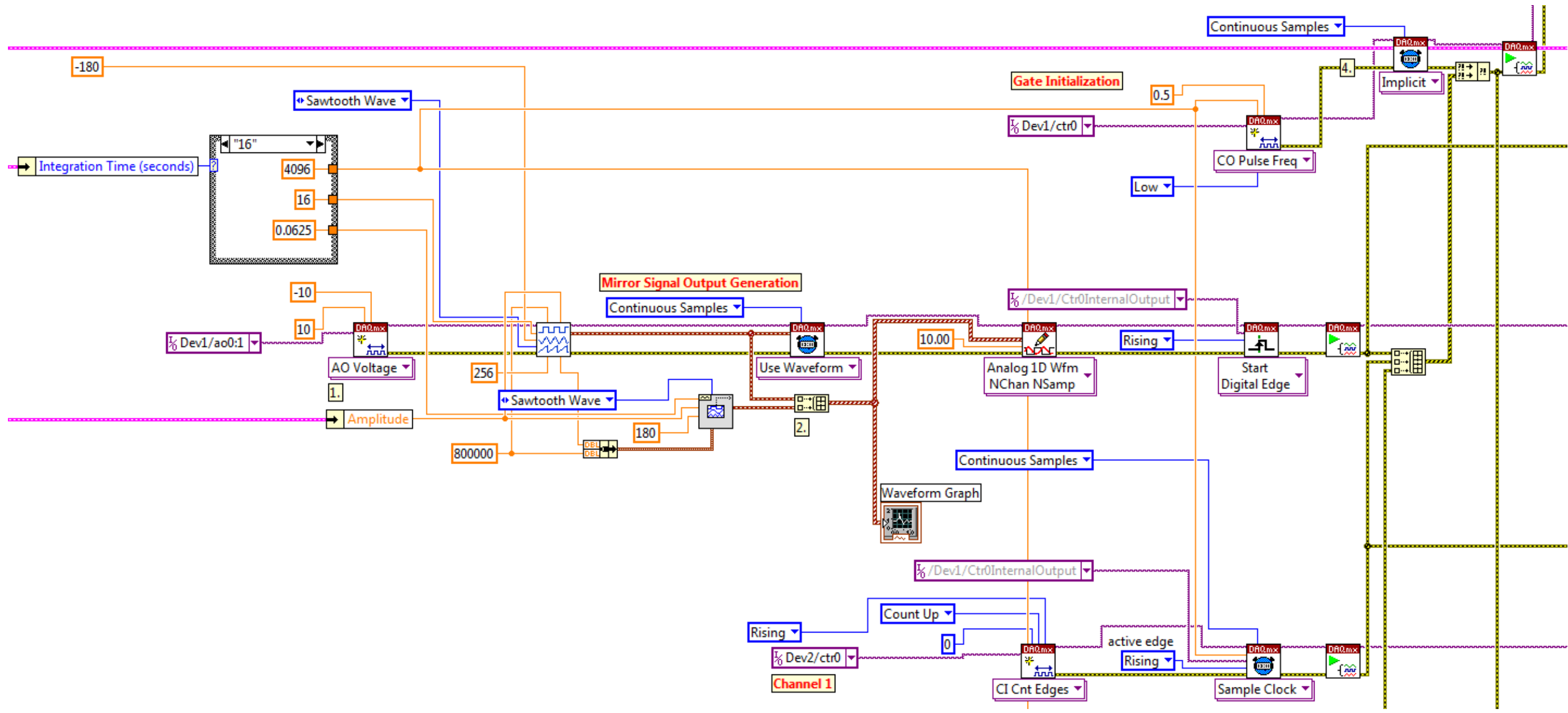
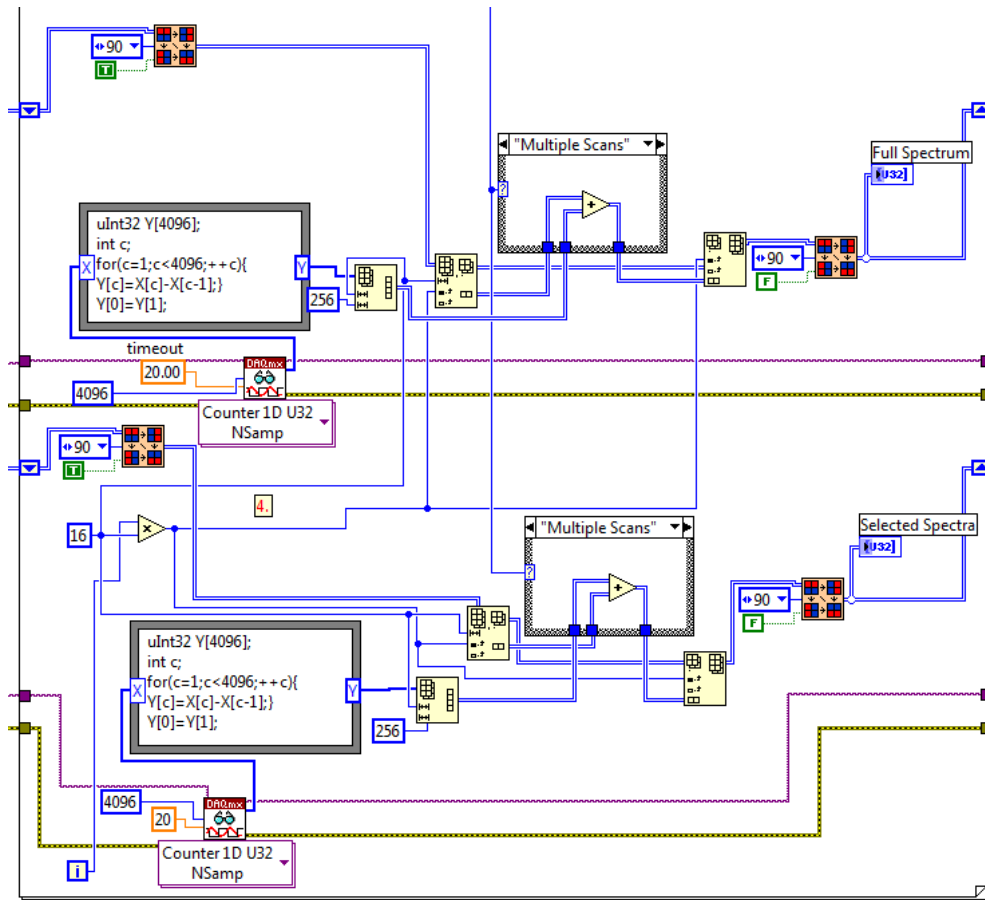


Figure 3.11. Open channels state S2.

Acquire Data state S3 is where actual imaging takes place. Data is received from the activated counter channels of S2 and split into segments of 4,096 pixels at a time as seen in Figure 3.12. Because the counter cards only count upward from pixel-to-pixel, subtraction must take place to determine the true count corresponding to each pixel. The short C script in the formula node performs this subtraction when the array is received from the counter. This data is then reshaped from a 1-dimensional array into an 8x256 pixel 2-dimensional array and displayed to the screen. The process is repeated 31 additional times to generate the entire 256x256 pixel image. When continuously scanning an image, the code takes the prior 8x256 array and replaces it with the updated array, allowing for smooth updating of the image. The counters are then deactivated, and the laser is then instructed to diverge from the sampling region.



**Figure 3.12. Acquire data state S3.**

Analyze Data state S4 is primarily for multiple-scanning calculations. Because many experiments desire the ability to rescan the area to improve signal-to-noise ratio within an image, a state must exist to determine whether additional scans are necessary to complete the acquisition of the current image layer. This check is performed in the sequence structure of Figure 3.13. An internal Scan Counter is used to determine whether the current scan number matches that of the user-specified value. If the value has not yet been reached, the software is instructed to return to state S2 to perform an

additional scan. The corresponding pixels in the new image are then directly added to the respective portion in the old one, creating a new image.

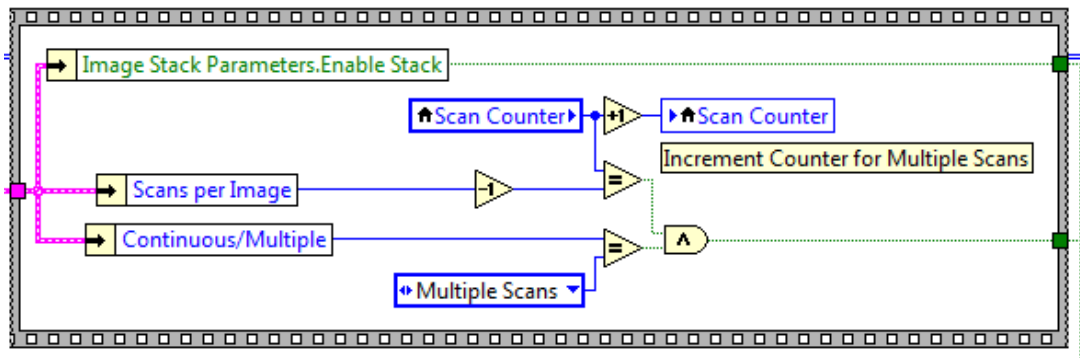


**Figure 3.13. Analyze data state S4.**

Save state S5 is used to transfer the data within the intensity images into readable files in the computer hard drive. The code, shown in Figure 3.14, concatenates the two images generated in NOMS as a 256x256x2 3-dimensional array, and saves the data as a binary file in little-endian format. The little-endian format stores data corresponding to the least-significant byte first. This characteristic is important as many computation applications such as MATLAB can only read data stored in little-endian format. Data stored in big-endian, with the most-significant byte first, will be loaded with corrupted data. State S5 also detects whether or not 3-dimensional stack acquisition has completed acquisition. If incomplete, a command is sent to the MAC5000 stage to move the stage along the Z-axis at the specified step size, and the system returns to state S2 to take the next image.

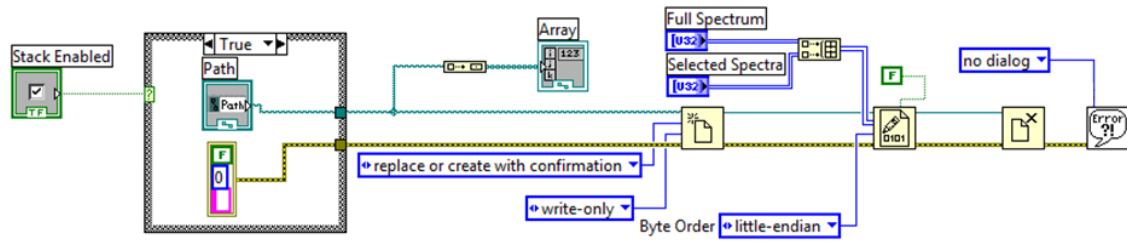


**Figure 3.14. Save data state S5.**

Exit state S6 exists strictly as a precautionary measure in case future program modifications require an emergency exit from the software. The present design of NOMS does not require such a state, but it has been added to the software if a need should arise in the future.

## CHAPTER IV

### NONLINEAR OPTICAL MICROSCOPY SPECTRAL IMAGING SYSTEM

Spectral acquisition of samples is important when given biological systems with multiple intrinsic and extrinsic fluorophores. This spectral data can be used for delineation and separation of colors, ultimately acting as a non-invasive method for separation of different biological components. The system has been named the Nonlinear Optical Microscopy Spectral Imaging System (NOMSIS). This chapter discusses the development of two variations of NOMSIS, to be referred as NOMSISv1 and NOMSISv2. The reasons for the development of two versions will be examined as well.

#### 4.1 FIBER-BASED SPECTRAL ASSEMBLY

Hardware development of NOMSISv1 is summarized in Figure 4.1. The optical setup is identical to that of NOMS up until detection. Instead of using the optical band-pass filters, fluorescent signal from the sample is directed through a tube lens coupled to an optical fiber and into a spectrometer housing containing a 16-channel PMT [13] as illustrated in Figure 4.2(a). The PMT then converts the optical fluorescence into sixteen channels of analog current. The electrical current is translated by an array of discriminators into 16-channel TTL pulses for photon counting.

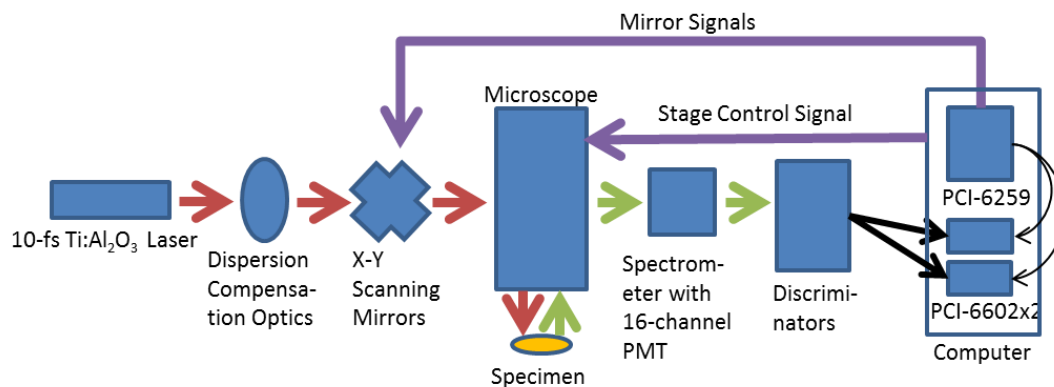


**Figure 4.1. NOMSISv1 system setup.**

Like NOMS, TTL pulses are detected by the NI PCI-6602 counter card, but two cards are used instead of one to accommodate all 16 channels. The software then uses the values of the counters and rearranges them as intensity pixels. Finally, LabVIEW renders a working image directly onto the front panel.

The multimode optical fiber with high numerical aperture ( $NA = 0.22$ ) with a large core ( $910 \mu\text{m}$ ) delivers fluorescent signal to the remotely located spectrometer optics. Within the spectrometer, NOMSISv1 incorporates a Czerny-Turner setup in a Littrow configuration for Figure 4.2(b). Exiting the fiber, the first optical component is an achromatic lens ( $d = 38.1 \text{ mm}$ ,  $f = 90.0 \text{ mm}$ ) for collimating divergent light. The light is then sent to a diffraction grating (53-067-455R, Richardson Grating) blazed at  $530 \text{ nm}$ . A focusing lens of  $f = 75.0 \text{ mm}$  is then used to demagnify the diffracted light onto the 16-channel detector (R5900U-00-L17, Hamamatsu).



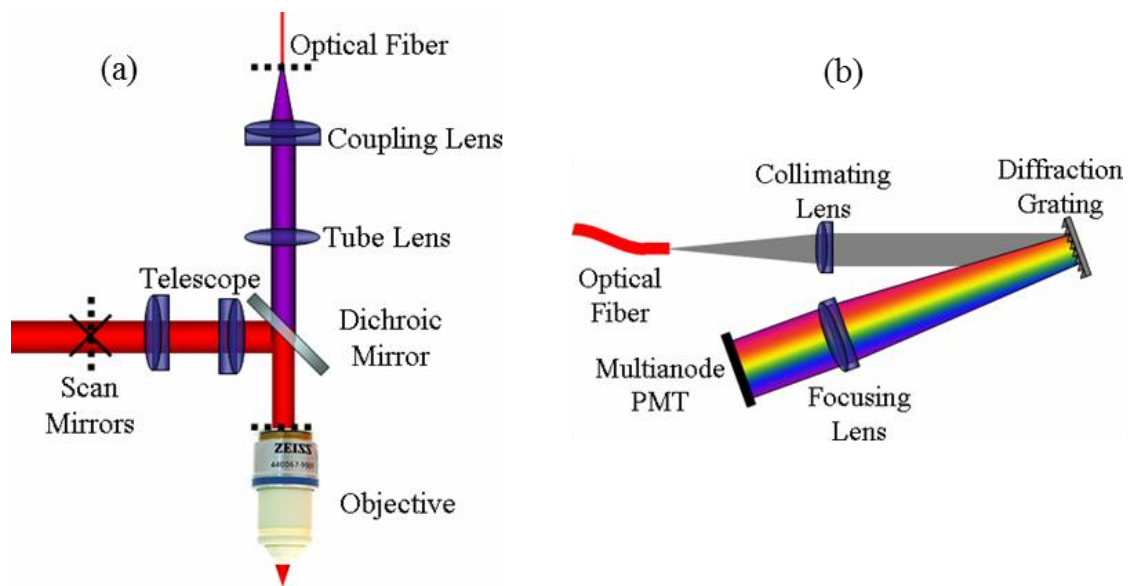


**Figure 4.2. NOMSISv1 optical setup with (a) schematic of the changes made within the microscope and (b) spectrometer setup.**

Linear dispersion of the diffraction grating represents the spectral extent per unit width. This dictates the spectral range that the spectrometer can detect. The formula for linear dispersion is represented as

$$\frac{d\lambda}{dx} = \frac{\cos(\beta)}{mdL_B} = 17.58 \text{ nm}, \quad (4.1)$$

where  $\beta$  is the diffraction angle,  $m$  is the diffraction order,  $d$  is the groove density of the grating, and  $L_B$  is the focal length of the focusing lens. Setting the central wavelength to 490 nm, we yield a spectral range of 350-630 nm, with each channel covering approximately 17.58nm of the spectrum.

## 4.2 SOFTWARE DEVELOPMENT

Modification of the user interface, as well as key components within NOMS source code is essential in making a working system for NOMSIS. The first portion of NOMS code requiring changes is the channel activation of the counters from S2 of the state diagram. Activation of each individual counting channel was expanded from simply 2 channels, to 16. Figure 4.3 illustrates the activation of channels 6-8. We can see that each channel possesses the same code for activation, with exception to the I/O input task which corresponds to the respective data line. The remaining channels not on the figure are activated in a similar fashion. One additional requirement is the modification of the counting mechanism from DMA to Interrupt, as seen in the invoke node.

State S3 requires modification as well. Figure 4.4 illustrates the processing of incoming pulses. The data is collected and subtracted from the previous element because of the upward counting of the individual counters. This separates the individual elements of the array as actual pulse counts. Once again, the code is duplicated and source code for all 16 channels can be implied from the figure.

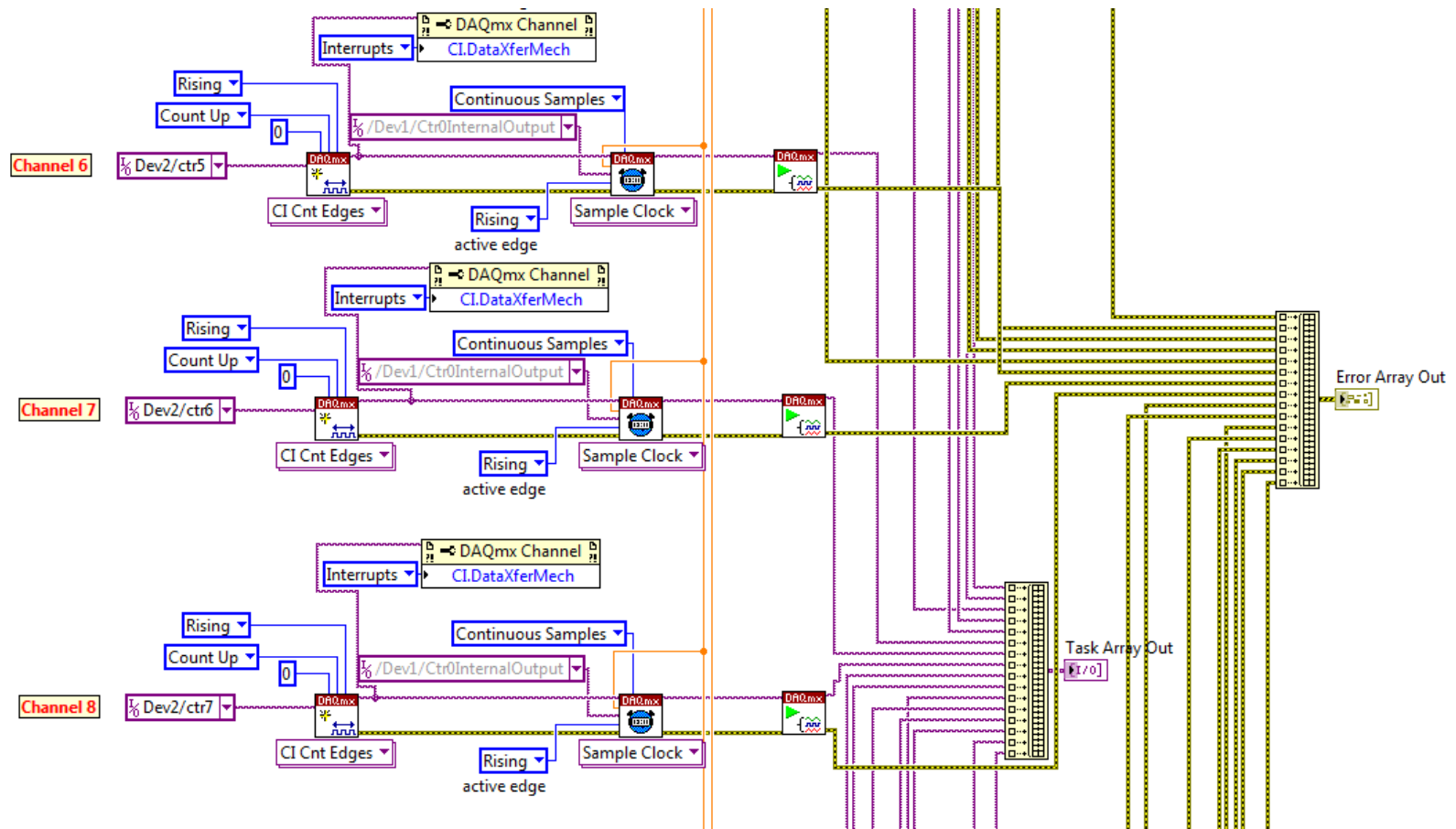


Figure 4.3. Channel activation.

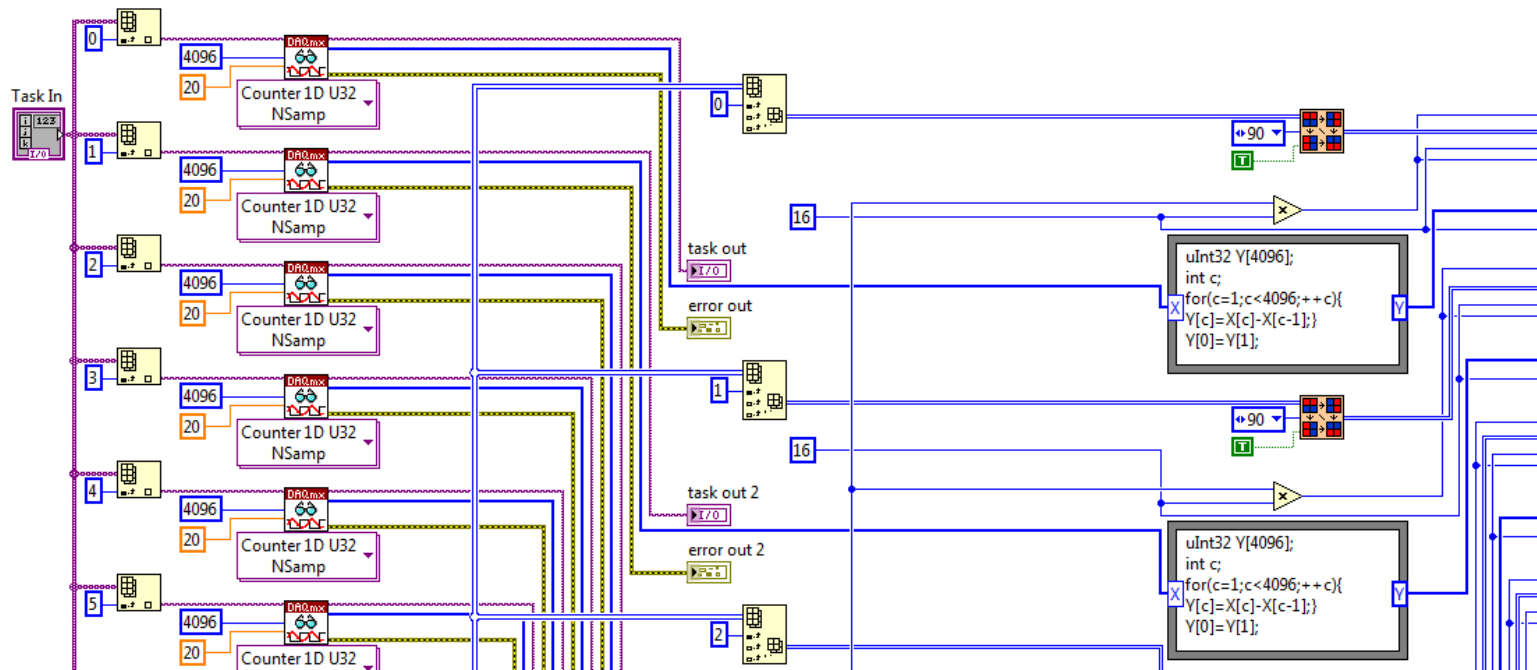
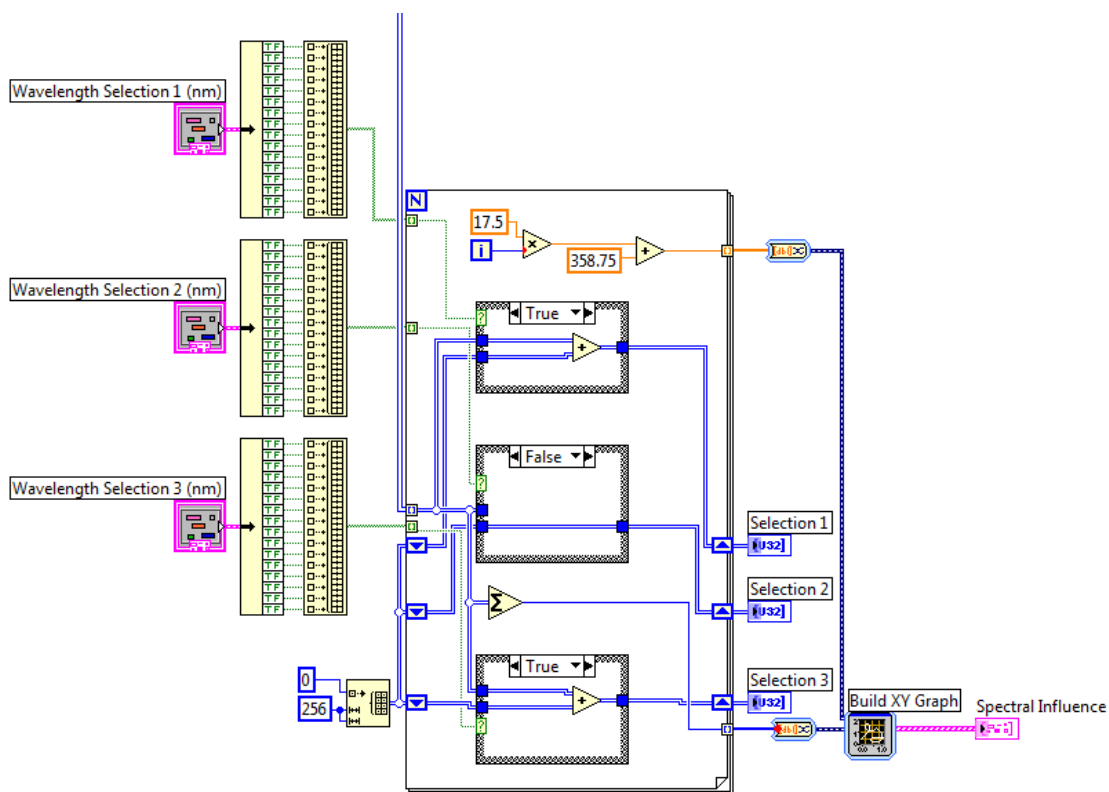


Figure 4.4. Data processing.

Significantly differing from NOMS, the code in Figure 4.5 is used for the front panel selection boxes, allowing for the on-off display of user-desired spectral channels. The series of Boolean selections are formatted into an array and processed by the for loop. The loop will sum together all of the individual 256x256 images that have been selected by the user on the front panel, creating a representative intensity image. The loop also generates the x-axis to be used for the spectral wavelengths of each channel.



**Figure 4.5. Wavelength selection and graph configuration.**

As seen in Figure 4.6, the NOMSIS software displays this array according to selected controls on the front panel. While actively collecting data, the imaging parameters are replaced by a spectral influence graph. This graph shows an on-the-fly spectral

representation of the sample as a whole by taking the summation of all the pixels in each corresponding channel. Each summation is representative of a single point on the spectrum and can be directly plotted onto the graph. The sample used in the image was endothelial cells expressing green fluorescent protein (GFP) embedded within a collagen matrix.

Selection 1 of Figure 4.6 shows the entire sample by selection of the channels corresponding to the peaks in the spectrum. We can clearly see both SHG signal from collagen and TPF of GFP from the cells. Selection 2 isolates the collagen by simply choosing the SHG channels, and selection 3 isolates the GFP signal from the cells. This effectively allows for quick spectral segmentation of biological specimen for uniquely different fluorescent markers.

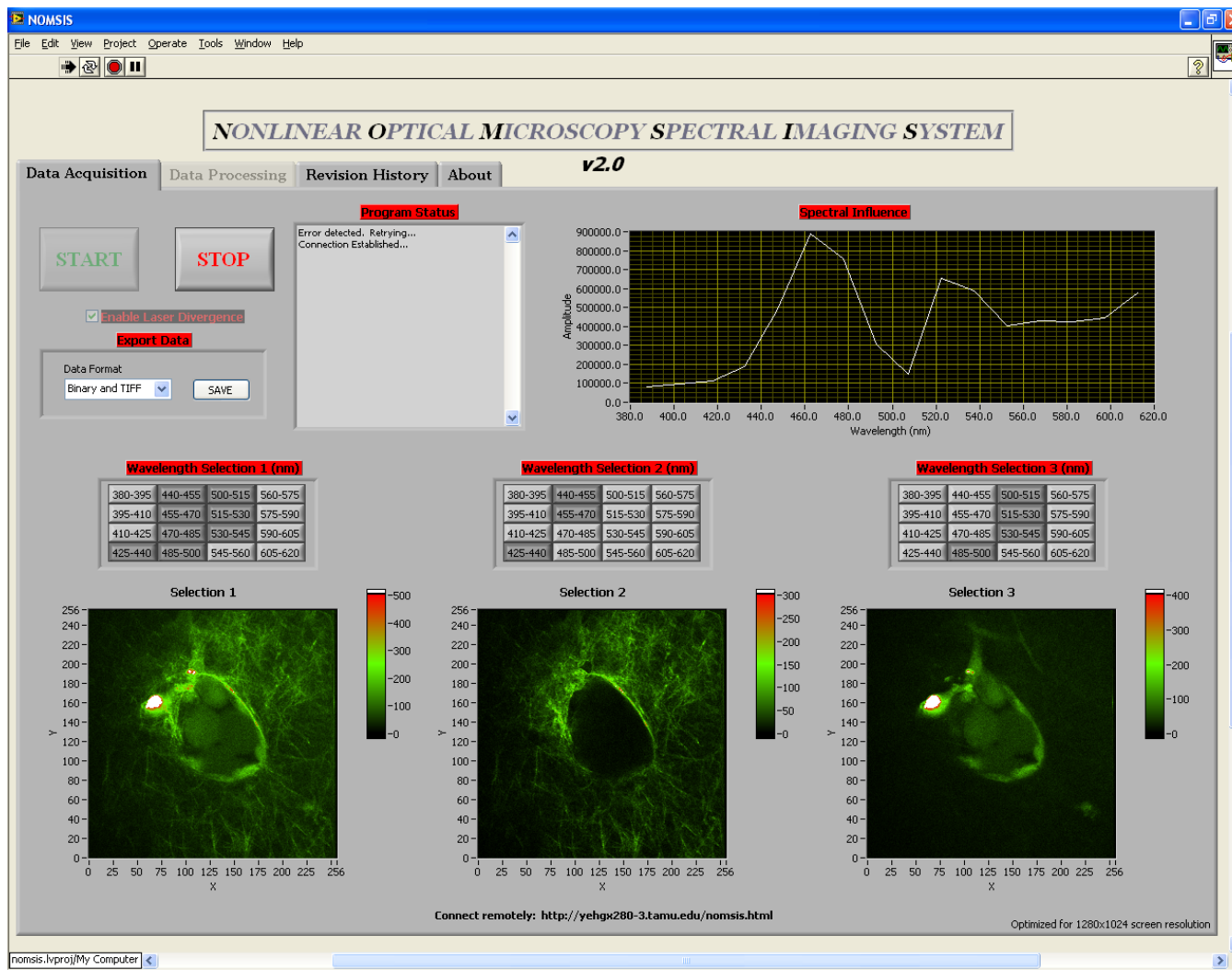


Figure 4.6. Nonlinear Optical Microscopy Spectral Imaging System interface.

### 4.3 LIMITATIONS OF SPECTRAL ACQUISITION

Upon completion of the initial 16-channel system, one significant limitation became apparent. The imaging speed must be greatly reduced in order to prevent an internal buffer error. Because the two NI PCI-6602 counter cards contain only three Direct Memory Access (DMA) channels per card, high-speed imaging is limited to a maximum of six channels at a time. DMA is a method used to transfer data into memory without involving the computer's CPU. Without enough DMA channels, counting mechanism is changed to Interrupt – a processing mechanism which requires the usage of the CPU for data transfer. Unfortunately in order to use all sixteen channels at once and prevent the buffer from overflowing, the imaging speed needs to be greatly reduced – the fastest possible speed being sixteen seconds per image. Because previous studies have shown that cellular migration can occur at a rate well over 1  $\mu\text{m}/\text{min}$  [14], sixteen seconds per image becomes insufficient for experiments collecting large quantities of data.

The alternative to this problem is to use a field-programmable gate array (FPGA) from National Instruments (PCI-7811R). Since an FPGA has much more memory, sixteen physical channels of data can be taken in a single high-speed DMA channel. This implementation should theoretically solve the issue with the counter cards and allow scanning frequency up to 1 image per second [15], and has motivated the need to create a new spectral system, NOMSISv2.



#### 4.4 DIRECTLY-COUPLED SPECTRAL ASSEMBLY

The system layout for NOMSISv2 is quite similar to NOMSISv1, with hardware changes made starting from the spectrometer. In addition to using FPGA, which will be discussed in detail in the following chapter, a more simplified approach to designing a spectrometer is desired as well.

Instead of using an optical fiber, NOMSISv2 directly couples the fluorescence detection optics to the microscope as seen in Figure 4.7. At the side port of the microscope, an achromat of  $f = 35.0$  mm will be used to demagnify the image of the exit aperture of the objective lens. An adjustable slit is used to control signal from the demagnifying lens. In order to mimic the optical fiber of NOMSISv1, the slit is open to the same distance as the diameter of the optical fiber. A mirror then directs this light onto an aberration-corrected concave holographic grating (533-01-370, Horiba) which can be directly transferred to the 16-channel detector (R5900U-200-L16, Hamamatsu). The use of a concave grating has been shown to simplify the optical setup for spectral imaging due to its unique shape, allowing for the input slit to be directly imaged onto a PMT [16].

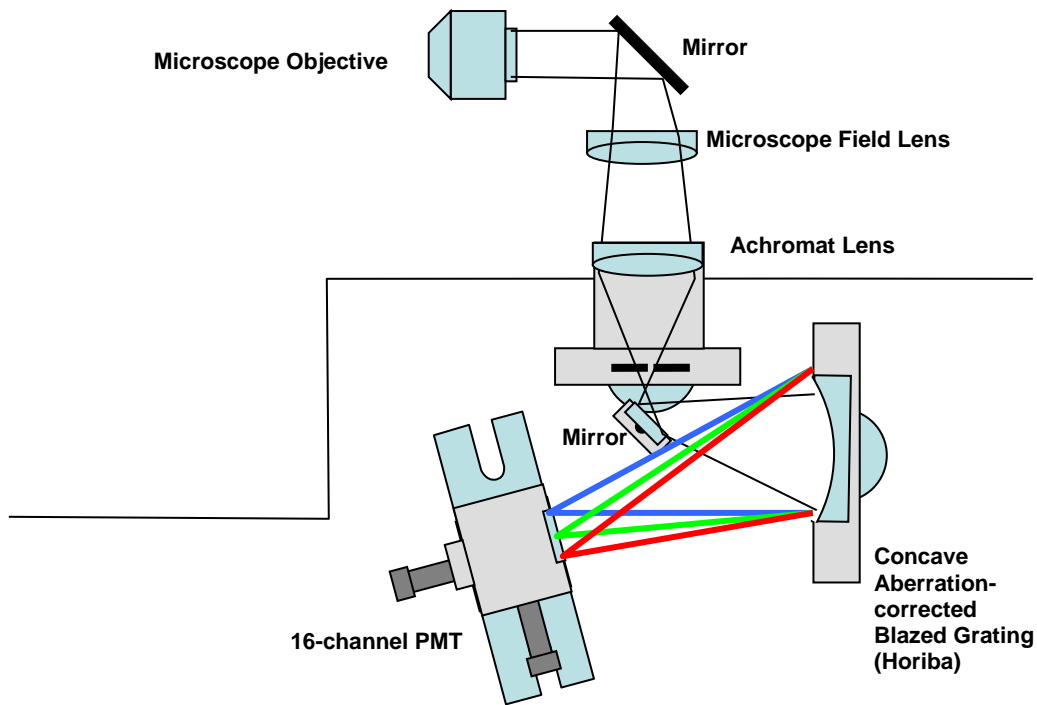


**Figure 4.7. NOMSISv2 spectrometer setup.**

The linear dispersion of the Horiba concave grating is

$$\frac{d\lambda_n}{dx} = \frac{10^6 \cos(\beta) \cos^2 \gamma}{knL_H}, \quad (4.2)$$

where  $\beta$  is the diffraction angle,  $\gamma$  is the tilt angle of the detector plane relative to the normal of the diffracted beam,  $k$  is the diffraction order,  $n$  is the groove density, and  $L_H$  is the effective focal length. Unlike the grating used in NOMSISv1, the concave grating has nonlinear dispersion, becoming shorter as the wavelength increases. Dispersions from the formula are summarized in Table 4.1 for the central wavelength of each channel of the detector.

**Table 4.1. Dispersion of Horiba concave grating.**

Channel Number	Dispersion (nm/mm)	Central Wavelength (nm)
0	21.4	350.7
1	21.1	371.8
2	20.7	392.5
3	20.4	412.9
4	20.0	432.9
5	19.7	452.7
6	19.4	472.0
7	19.0	491.0
8	18.7	509.7
9	18.3	528.0
10	18.0	546.0
11	17.7	563.7
12	17.3	580.9
13	16.9	597.9
14	16.6	614.4
15	16.3	630.7

The results show the corresponding dispersion, with the shorter wavelengths possessing a larger channel width. Varying slightly from NOMSISv1, the spectral range for NOMSISv2 is from 340-639 nm.

## **CHAPTER V**

### **FIELD-PROGRAMMABLE GATE ARRAYS**

A field-programmable gate array (FPGA) is used for many engineering applications to streamline signal processing and data analysis. To overcome the limitations of NOMSISv1, an FPGA is used to collect high-speed data. Section 5.1 provides a brief overview of FPGA technology, and Section 5.2 details the integration of FPGA code into NOMSISv2.

#### **5.1 FIELD-PROGRAMMABLE GATE ARRAY BASICS**

An FPGA is a programmable integrated circuit capable of running an instruction set, known as hardware description language (HDL), at speeds independent of the computer's clock speed. This allows a complex program to run on the oldest of computers while avoiding hardware speed issues. FPGAs can also interface with external systems, allowing for a smooth integration of FPGA into existing technology. As modern-day technology advances, more and more systems are incorporating the usage of FPGA hardware.

Inside the board, an FPGA consists of digital hardware known as logic blocks which are interconnected with one another. Once the HDL code is compiled and synthesized, the programmable interconnects turn on or off respectively, and a unique digital circuit is

then created to represent the desired system. The configuration is saved as a single bitfile which can be stored directly to a computer's hard drive. Analogous to a computer's executable file, a bitfile represents the set of HDL instructions that have been programmed by the user for the FPGA. This allows the FPGA to immediately configure the digital circuit without re-synthesis of HDL code.

HDL is a low-level programming language which directly interfaces with digital logic circuits and memory registers. To make FPGA programming as familiar as possible to the standard LabVIEW developer, NI created the FPGA Module which masks the complexity of writing HDL code. Users may program the FPGA with a specialized LabVIEW function set designed specifically for FPGA boards.

The NI PCI-7811R FPGA was chosen for photon counting implementation. The FPGA has an internal clock of 40 MHz. If each clock cycle is used to check on the High/Low status of an incoming pulse, it would take two clock cycles to determine a pulse has passed. This means photon counting can only be as fast as half the internal clock, 20 MHz. By default, the discriminators have a pulse width of 10 ns. Because the FPGA can only check the digital lines once every 25 ns, a 10 ns pulse may be completely missed by the FPGA. Therefore, the discriminators will need to have their pulses expanded to a value greater than or equal to 25 ns. With NOMSISv2, an adjustment of 30 ns pulse width will be used to be safe.

The 16-channel data is stored inside the FPGA's high-speed FIFO (first in, first out) memory stack. In the case of a 1-second scan, the FPGA would be configured to store data once every 15.26  $\mu$ s. From there, NOMSISv2 can pull the data at its own pace for image rendering. The FPGA software will have basic input/output elements. By using it as sub-element within the NOMSIS software, the FPGA code can be directly integrated into present LabVIEW code.

## 5.2 SOFTWARE DEVELOPMENT

FPGA code will replace the channel-activation sub-vi within state S2 for NOMSIS. To begin LabVIEW FPGA-based photon counting, the FPGA requires some form of starting signal to act as the trigger. For this, we can use the same pixel clock as generated for NOMSISv1 by interconnecting the signal into an FPGA input channel. Using the FPGA palette, the corresponding data channel can be placed within a while loop to continuously poll the input until the signal has arrived.

FPGA trigger detection code is shown in Figure 5.1. Because the pixel clock acts as a trigger mechanism for photon counting, the signal must pass directly to the FPGA for activation of the counting channels. The signal enters the FPGA board via the *Real-time System Integration* (RTSI) cable internally attached to the data acquisition board within the computer. RTSI buses act as the interconnection for different hardware systems, in this case the FPGA board and the data acquisition board. The while loop will

continuously check the status of the RTSI channel until it receives a digital high value, thus exiting the loop and entering the counting portion of code.

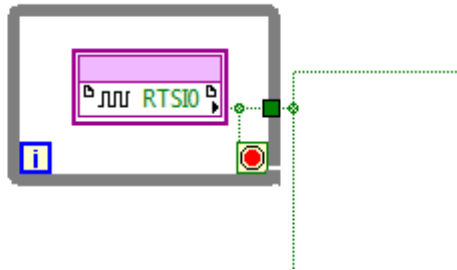


**Figure 5.1. FPGA trigger detection.**

FPGA counting consists of two portions: pulse counting, and data storage. Figure 5.2 demonstrates the code required for the pulse counting to take place. The green logic line entering from the left is from the trigger detection output. Once the trigger gives the active signal to begin counting, the internal 40 MHz clock of the FPGA is activated for a single-cycle timed while loop, meaning it executes the code within the loop on every rising edge of the clock.

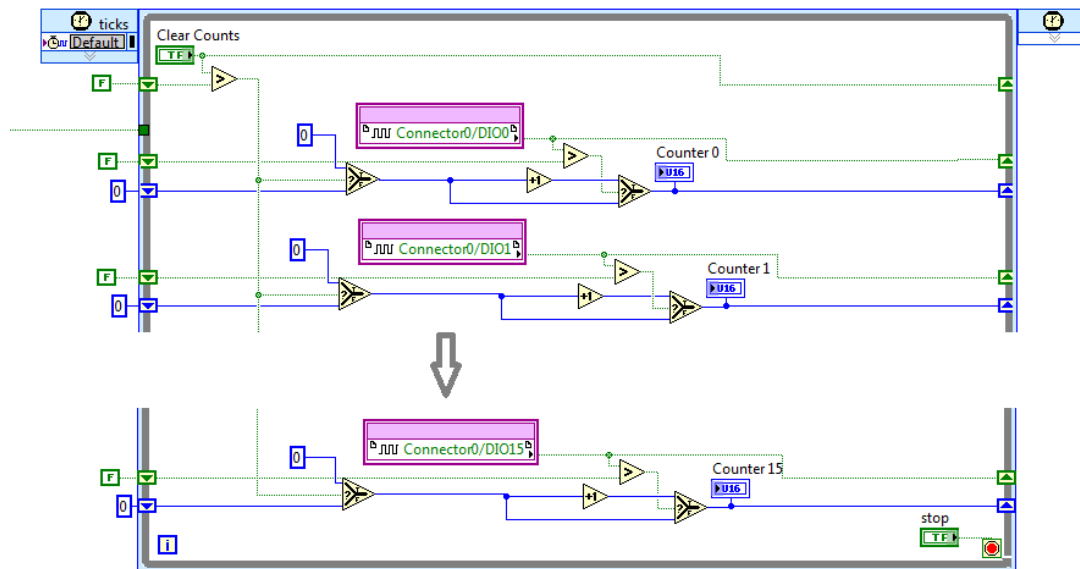


**Figure 5.2. FPGA counting channels.**

The code first checks if *Clear Counts* control is 1 or 0. Initially it will always begin as 0, then checks the signal lines of each respective digital input/output (DIO) channel. If the DIO channel transitions from 0 to 1, then the counter will increment itself. Any other combination will leave the counter unchanged, as care must be taken to not increment the counter until the entire pulse has been detected and passed through the channel.

Table 5.1 demonstrates this behavior of the counters as the FPGA takes measurements from each DIO. Action will only be taken when pulse transitions are detected. Once *Clear Counts* changes to a 1, every counting channel will reset itself to zero counts.

This acts as a reset mechanism to restart the counting at the beginning of each pixel.



**Table 5.1. Pulse transitions.**

<b>Status</b>	<b>Old Value</b>	<b>New Value</b>	<b>Transition Detected</b>
<b>No Pulses</b>	0	0	No
<b>Pulse Received</b>	0	1	Yes
<b>Pulse Still Active</b>	1	1	No
<b>Pulse Exit</b>	1	0	No

Data storage for the FPGA is seen in Figure 5.3. FPGAs have a built-in stack for temporary memory storage. This stack is known as a *first-in, first-out* (FIFO) stack. In memory systems, FIFO stacks are beneficial when receiving large blocks of data on a continuous basis. This data can be removed and processed from the stack by the computer starting from the element that came first, as the name FIFO implies. If data arrives faster than the computer can process, FIFO stacks are typically implemented. In the case of high-speed photon counting, FIFO is essential. The FIFO buffer will store incoming photon counts and remove them when the computer has caught up to the remaining data elements to be processed.

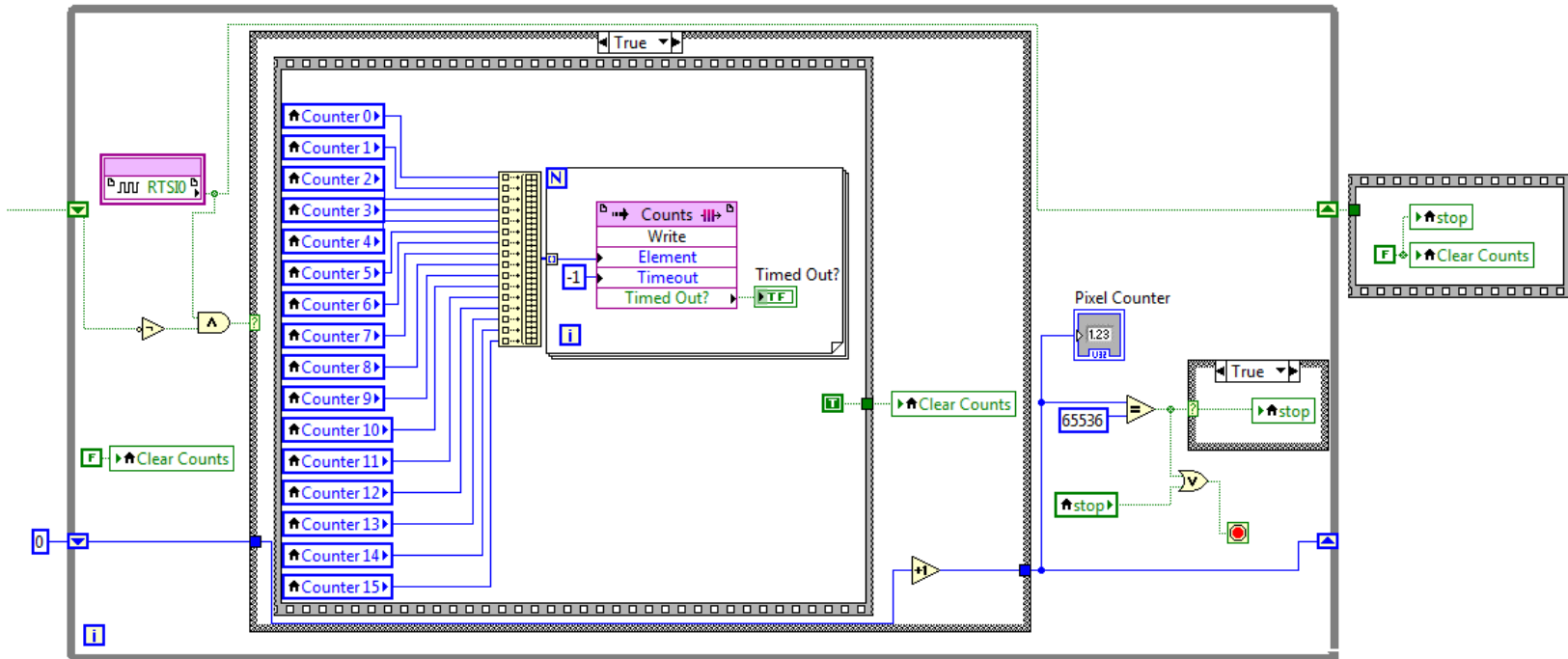


Figure 5.3. FPGA data storage.

Similar to detection of pulse transitions in FPGA photon counting, the loop begins with pulse transition detection of the pixel clock. The system needs to know when each pixel has passed, and therefore needs to check for pulse transitions of the RTSI channel using the same scheme as Table 5.1. Pulse transition of the RTSI implies the end of a pixel and to write out the counts stored in the counting channels into the FIFO. In the case of a 1-second scan of a 256x256 pixel image, transitions are detected at a rate of 65,536 Hz. Within the case structure, 16 channels worth of counting data is compiled into a single array of integers. The *Write* function sends this data into the FIFO and then *Clear Counts* is set to 1. This tells the FPGA to reset the counters according to the code from Figure 5.2. Afterwards, error-checks are implemented to ensure the system does not exceed the end of the image. Particularly, a 256x256 pixel image should not have more than 65,536 elements. The indicator *Pixel Counter* is used for this verification.

The code from Figures 5.1, 5.2, and 5.3 represent the code to be compiled into HDL. Complete, unmodified FPGA code can also be seen in Appendix C. Upon compilation, an FPGA reference can be opened within the NOMSIS software to run the bitfile that has been synthesized from the FPGA source code. A special sub-vi must be used to reference the FIFO.

The sub-vi for FIFO extraction is shown in Figure 5.4. Because the data for each set of pixels is stored as a 1-dimensional array of 16 elements, FIFO data must be pulled at a multiple of 16 elements per execution. For example, two pixels of data are stored in the

FIFO as a series of integer elements from [E0, E1, E2, ..., E31]. E0-E15 represents the first pixel, while E16-E31 represents the second. To reduce strain on the CPU, 1024 pixels are acquired at once, meaning *Number of Elements* is set to 16,384. The invoke node pulls all of the elements from FIFO using *Counts.Read*, and immediately reprocesses the data from a 1-dimensional 1x16384 element array into a 3-dimensional 16x4x256 array using LabVIEW's built-in array functions. The loop afterwards prepares this array for insertion directly into the front panel of NOMSIS as a processed image. This process is repeated 64 more times until the entire 256x256x16 image has been fully acquired. The code is placed as a sub-vi within S3 of the state machine algorithm.

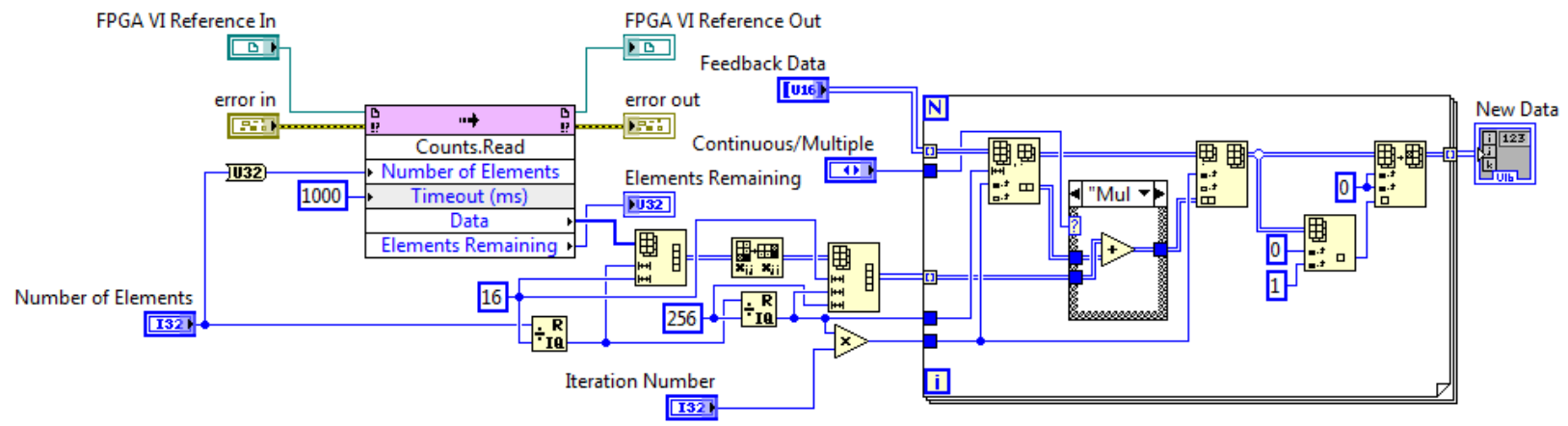


Figure 5.4. Reading from FIFO.

## **CHAPTER VI**

### **EXPERIMENTAL VALIDATION**

With two NLOM spectrometers, we need to compare the two setups and determine which design produces the ideal signal collection, as well as provide datasets as validation of working systems. Section 6.1 discusses the theoretical and experimental comparisons between NOMSISv1 and NOMSISv2. Section 6.2 explains data processing method for noise removal. Sections 6.3 and 6.4 describe experiments for using NOMSIS as a valid method of spectral imaging and analysis.

#### **6.1 OPTICAL COLLECTION EFFICIENCIES**

Optical collection efficiency refers to the ability of the collection optics to detect signal from incoming fluorescent photons. This limitation is primarily based on the least-efficient optical component in the detection pathway. Fluorescent signal collection for the NOMS system is strictly limited by the numerical aperture of the objective. Signal collection for NOMSISv1 is limited to the numerical aperture of the fiber, whereas signal collection for NOMSISv2 is limited to the numerical aperture of the optical grating.

By recording depth-resolved three-dimensional data, a comparison can be made by observing both of the spectral systems' image stacks with respect to NOMS data at its

specified filter settings and laser power. Because each individual pixel represents an integer photon count, collection efficiency can be directly measured as the summation of the pixel intensities across the entire image. There are several important characteristics which can be derived from this data.

As images are collected with depth into a biological sample, the collection efficiency will decrease due to scattering [17]. Scattering occurs because the specimen introduces deviations in the optical pathway for signal collection. As depth of imaging becomes greater, so does optical scattering. In order to characterize this behavior, direct measurements of depth-resolved photon counting may be used. This signal decline is expected to follow an exponential decay [18,4], however the usage of a sub-10 fs laser should theoretically increase depth penetration allowing for a much slower rate of decline due to the lack of surface background fluorescence [6]. By using the decay model and calculating signal-to-noise ratios (SNR), we can quantitatively determine which system performs best. Ultimately, this experiment will provide insight as to how an optical fiber-based spectral imaging system compares to that of a directly-coupled spectral system. Additionally, a standardized model for comparing multiphoton imaging systems can be determined. The results are expected to provide insight to the relationship between ultrashort-pulse two-photon imaging to that of fluorescent scattering and depth-resolved imaging efficiencies.

The optical collection efficiency can be quantitatively represented as the spectrometer's etendue, which characterizes the ability of a system's acceptance of light. Geometric etendue, represented as  $G$ , is a function of the area  $S$  representing the source of light and the numerical aperture  $NA$  expressed as

$$G = \pi S(NA)^2. \quad (6.1)$$

In an ideal system with perfect transmission of light, two optical systems can be directly compared by taking their ratio of etendue, or

$$\frac{G_2}{G_1} = \frac{\pi S_2(NA_2)^2}{\pi S_1(NA_1)^2} = \frac{S_2(NA_2)^2}{S_1(NA_1)^2}. \quad (6.2)$$

Because the optical setup for NOMSISv1 and NOMSISv2 use the same geometric area, the etendue ratio can be further simplified to

$$\frac{G_2}{G_1} = \frac{(NA_2)^2}{(NA_1)^2} = \frac{(0.25)^2}{(0.22)^2} = 1.29, \quad (6.3)$$

which implies the etendue of NOMSISv2,  $G_2$ , is 29% more efficient than  $G_1$ , the etendue of NOMSISv1. The calculation is based on the assumption of 100% transmission of light through all optical components, which is not the true representation of the optical setup. By factoring in the transmission efficiencies of optical components such as the gratings and mirrors, a more accurate representation is

$$\frac{G_2}{G_1} = \frac{(NA_2)^2 T_1}{(NA_1)^2 T_2 T_3 T_4 T_5} = \quad (6.4)$$

$$\frac{(0.25)^2 * 0.65}{(0.22)^2 * 0.6 * 0.98 * 0.98 * 0.98} = 1.48,$$

where  $T_1$  represents the average transmission efficiency of the concave grating,  $T_2$  is the average transmission efficiency of the linear grating, and  $T_3$  through  $T_5$  represent the



transmission through the coated lenses. Ultimately, the optical setup of NOMSISv2 should theoretically be 48% more efficient than that of NOMSISv1.

Unfortunately this calculation also assumes ideal photon collection of the electrical components with equivalent SNR. As mentioned in Chapter IV, several counting electronics were modified in order to fit the parameters required for FPGA counting in NOMSISv2. Direct comparison through theoretical equations is limited because of the manual thresholding required of the discriminators. The only way to fully compare the two systems is experimentally through analysis of the data stacks and raw photon counts.

The experiment is performed on the upright microscope using a green fluorescent slide and imaged in software to collect the raw photon counts. The fluorescent slide is imaged completely through top to bottom, and the photon counts are plotted with respect to depth. Laser power and sample location is fixed to prevent any deviations in data due to variables. SNR comparisons will ultimately determine the ideal imaging system.

The experiment is performed using four different NLOM setups. NOMS is to be used as a control for a point of reference. NOMSISv1 is then used to take the exact same stack. An intermediary setup, using the fiber-based optics of NOMSISv1 with the FPGA counting of NOMSISv2 helps differentiate between the root cause of any significant SNR differences between the optics and electronics. Finally, the experiment is repeated one last time using the NOMSISv2 setup. Two goals are desired in the experiment. The first is proper exponential decay of the signal with respect to depth, verifying the

different NLOM setups as properly collected data. The second is to determine the SNR of the systems using the data, effectively providing the true conclusion as to which optical system performs better in its current state.

Figure 6.1 summarizes the results in the graph of raw photon counts versus depth in  $\mu\text{m}$ . 2-channel data is displayed using the entire dataset from NOMS. The spectral systems are displayed using the summation of data in the five strongest channels, effectively representing the photons collected for spectral full-width at half-max (FWHM). Choosing only the channels representing FWHM minimizes the effects of noise on both spectral systems and allows for irrelevant noise to be excluded from the true SNR. As expected, an exponential decay is observed for all system setups.

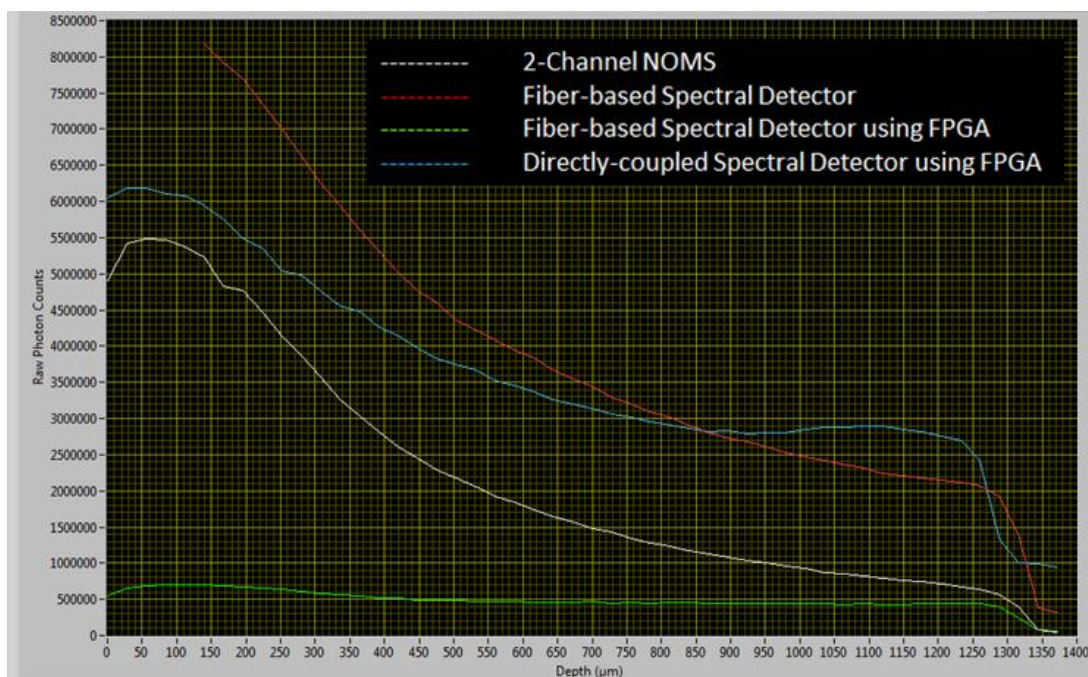


**Figure 6.1. System comparisons.**

The absolute maxima for all setups should exist at the same depth. For the fiber-based spectral detector, a lack of water under the immersion objective created a delay in signal generation. We can take note that the actual peak for the setup is roughly 5% higher than presented in the figure which should slightly increase the SNR. Because the fluorescent slide is not infinitely thick, the expected value for noise in SNR would be that of the raw photon counts after the laser has passed through the slide. Therefore, calculation of the SNR can be performed by taking the ratio between the strongest point in the signal curve with respect to the corresponding signal at the drop-off point when the laser has passed through the sample. The results are summarized in Table 6.1.

**Table 6.1. Experimental configurations with calculated SNR.**

<b>NLOM Setup</b>	<b>Optics</b>	<b>Electronics</b>	<b>SNR</b>
NOMS	Filters	Counter Cards	61.1
NOMSISv1	Fiber-based Spectrometer	Counter Cards	20.5
Intermediary	Fiber-based Spectrometer	FPGA	7.78
NOMSISv2	Directly-coupled Spectrometer	FPGA	6.20

NOMSISv1 is expected to have a fair reduction in SNR compared to NOMS due to the reduction in NA and attenuation of optical transmission from the spectrometer. As the experimental setup changed from NOMSISv1 to the Intermediary, a surprising reduction of nearly 3x SNR is observed. Based on the green line of Figure 6.1, the results show that the usage of the new discriminators with FPGA-based photon counting caused a

significant reduction in the maximum signal. The root cause may be from a loss in efficiency in counting by using an FPGA as well as an increase in noise from the new discriminator array. The data indicates that NOMSISv1 is the ideal system when taking spectral images of samples that are not time-limited.

## 6.2 NOISE REMOVAL

High quality images are a necessity for processing and presentation of experimental datasets in NLOM. Because the discriminators for NOMS and NOMSIS are highly sensitive to electromagnetic interference from the environment, a few datasets may easily be clouded by noise. This is evident by the random speckle pattern apparent within images. For our NLOM systems, noise can be removed by a simple algorithm of equating the noisy pixel to a non-problematic neighbor. The image resolution is high enough to perform the task without causing aberrations in the data.

LabVIEW code for noise removal is shown in Figure 6.2. The corresponding intensity data enters the loop from the left, with a user-specified noise threshold set into the *threshold* control. Because LabVIEW supports basic C programming code, the data can be passed into a formula node which contains the algorithm for noise removal. The code analyzes data row-by-row, and compares the intensity difference from one pixel to the next. If this difference exceeds the *threshold* value, the noisy pixel is set equal to the intensity of its neighbor. The current state of NOMS and NOMSIS do not implement

this feature automatically, however future work could implement the *threshold* control into the front panel of the software for automated noise removal.

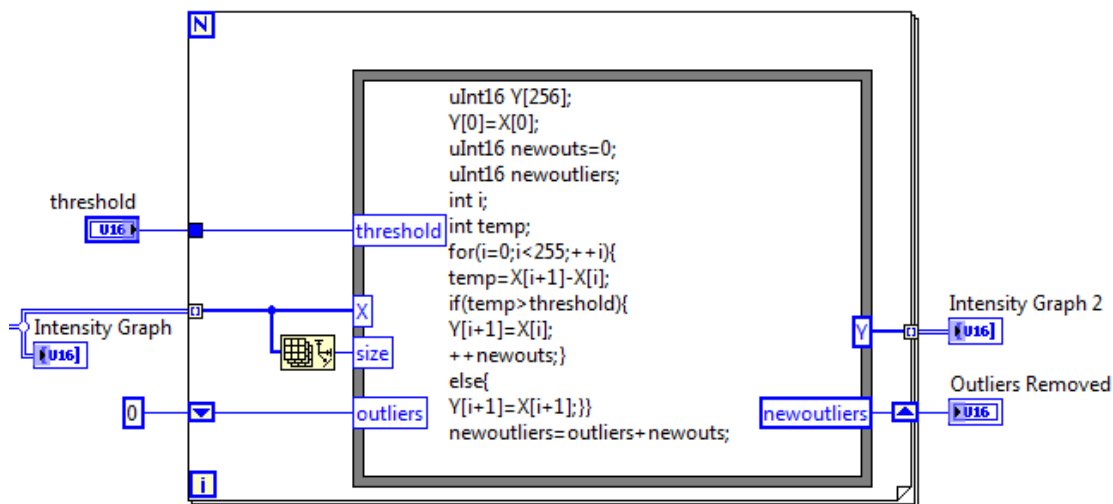


**Figure 6.2. Noise removal.**

Figure 6.3 validates this process as seen in the pre-processed and post-processed images for despeckling of a zebrafish eye. The unprocessed dataset on the left has a fair number of pixels plagued with noise. This is most easily identified by the bright spots in the dark portions of the image. With a threshold level of 70 for this particular sample, a total of 1,150 noise pixels covering roughly 1.8% of the image are removed via post-processing. This process saves valuable time and prevents the need for reacquisition of datasets when noise exists throughout an image.

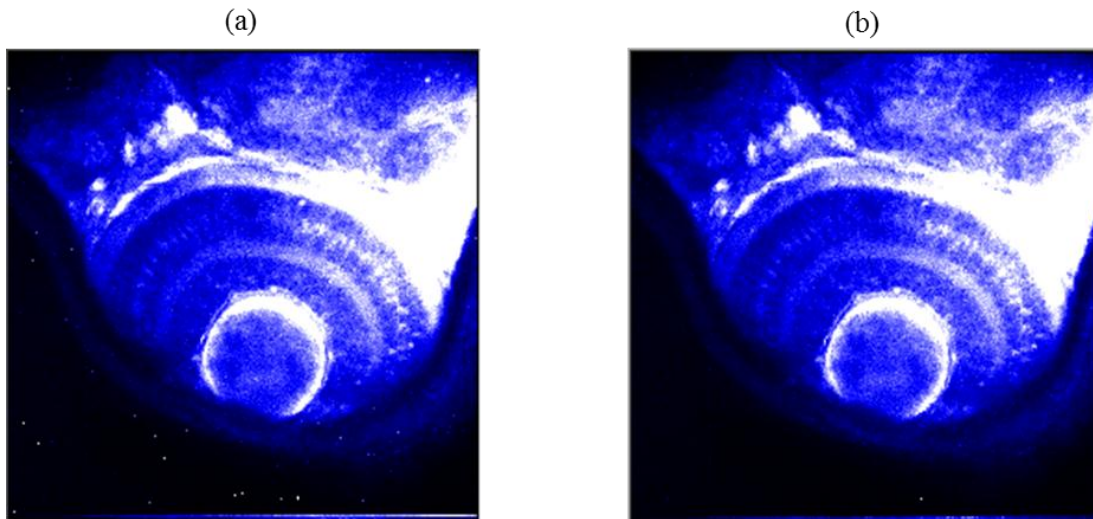


**Figure 6.3. Collected (a) pre-processed and (b) post-processed data.**

### **6.3 IN VITRO IMAGING OF AN ANGIOGENIC SYSTEM**

Experimental validation of NOMSISv1 is performed using an in vitro model that mimics angiogenesis [13]. Human endothelial cells (EC) expressing green (GFP), yellow (YFP), and cyan fluorescent proteins (CFP) are mixed and stimulated to penetrate a 3D well consisting of collagen matrix. Given time to incubate, the cells assemble into multicellular structures surrounding an open lumen. The goal of the experiment is to delineate multiple colored ECs from a body consisting of multiple fluorescent fluorophores.

For initial reference spectra, confluent populations of each fluorescent EC cell line are imaged within a 12-well plate. Data for corresponding spectra are normalized and shown in Figure 6.4.

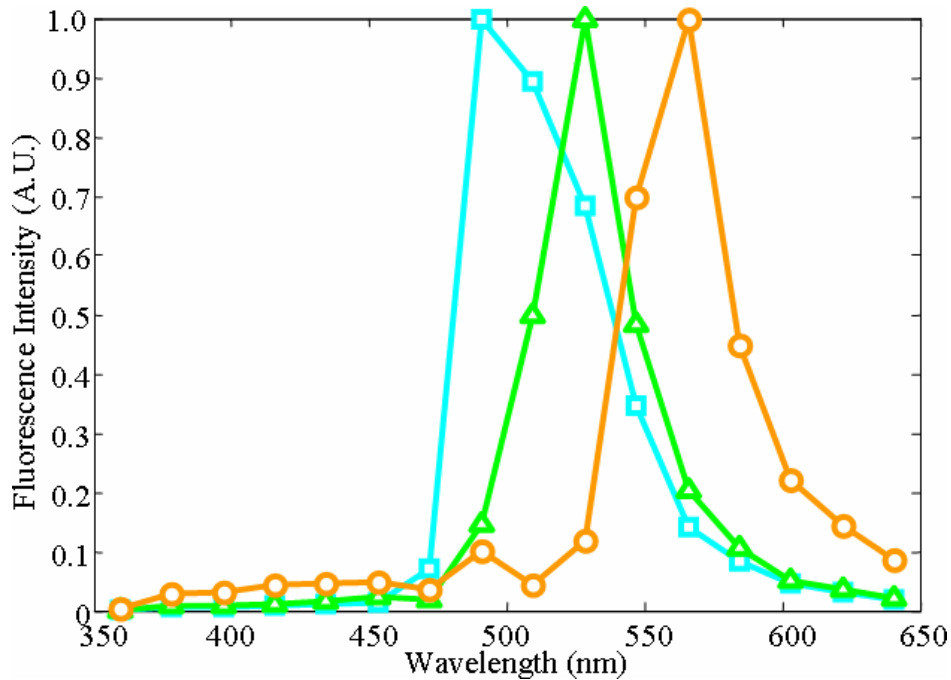


**Figure 6.4. TPF spectra for CFP, GFP, and YFP.**

The mixed sample of ECs within the collagen is allowed to incubate and invade the collagen for 60 hours before imaging. Figure 6.5 illustrates a resulting representative image of the system taken near the monolayer of the sample. The numbered spectra correspond to the regions marked in the NOMSIS image, with false color applied to illustrate the locality of fluorescence. SHG from the collagen is left in grayscale.

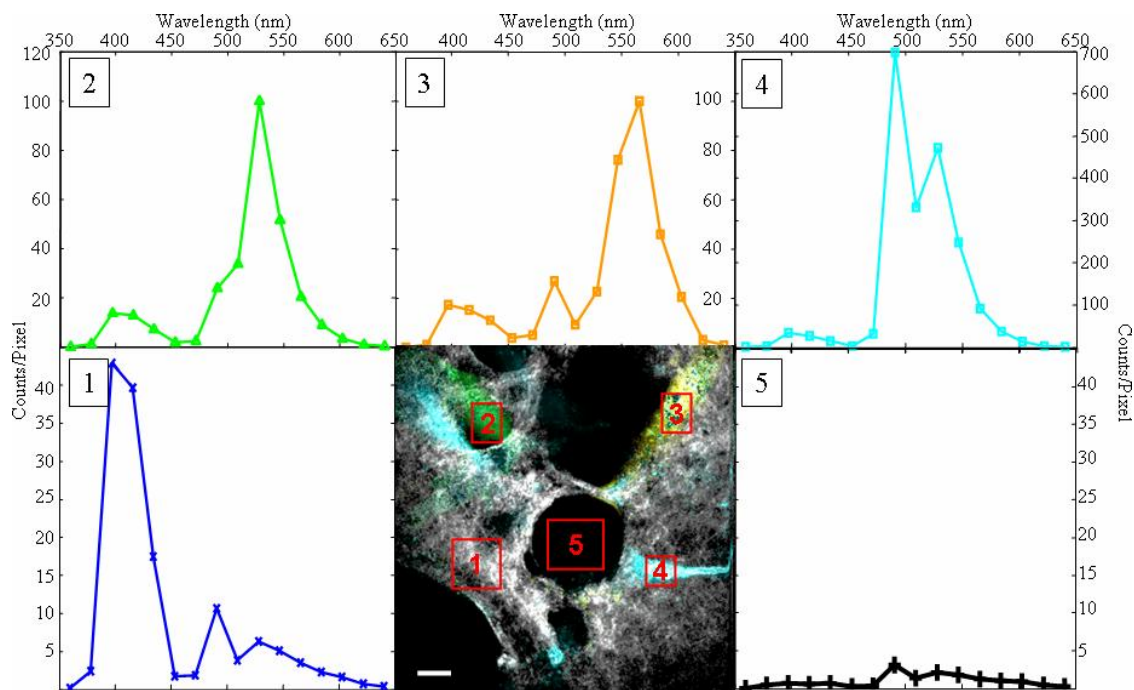


**Figure 6.5. Spectral analysis of endothelial cells. Scale bar 15  $\mu\text{m}$ .**

Region 1 corresponds to expression of second harmonic signal from collagen. Regions 2 through 4 correspond to endothelial cells expressing GFP, YFP, and CFP, respectively. Region 5 corresponds to the lumen of the cell, which lacks signal as expected and corresponds to dark count of background signal. The data shows that the system can clearly identify individual spectra expressed from multiple fluorophores with just a single scan of data.



## 6.4 SPECTRAL ANALYSIS OF MULTICOLOR ZEBRAFISH

The zebrafish eye has become an important model for study due to the similarities in morphology to the human eye [19-21]. The fast life cycle of the fish, transparency of the embryo, and the large number of eggs allows for detailed studies to be performed for analysis of eye development. NOMSISv2 will be validated by a study of zebrafish expressing multiple fluorescent fluorophores within the eye. Multicolor zebrafish were provided by researchers from Georgia Health Sciences University and prepared as described [22]. Mating between the fish have produced an embryo with positive expression of enhanced CFP (ECFP) from transgene *pax6-DF4:gap43-CFP* and enhanced YFP (EYFP) from transgene *UAS:gap43-YFP*.

EYFP expression is targeted to the retinal bipolar interneurons of the eye, and ECFP expression is a membrane-tagged reporter and expressed in membranous regions of the fish. The inner plexiform layer (IPL) is where several retinal neuron subtypes – including bipolars – make synaptic connections. It can be clearly identified by its unique semicircular structure within the retina and surrounding the lens. Because the ECFP is membrane-tagged, the IPL and other synaptic neuropils are labeled strongly since they are membrane-rich regions. Using the same zebrafish data illustrated in Figure 6.3, the spectrum is shown in Figure 6.6. The graph clearly indicates two unique fluorophores represented by the two maxima in the graph at 405 nm and 500 nm. Unlike the dataset from the ECs, spectral analysis of the zebrafish eye will be performed using subtraction

instead of localized analysis. Because the spectral graph represents the image as a whole, individual pixels can be uniquely classified by applying a mask. When analyzing pixels corresponding to EYFP, the spectrum will exhibit a strong unique peak corresponding to the 500 nm channel. Similarly, the pixels corresponding to the membranous expression of ECFP will have a unique peak at 405 nm. This characteristic allows us to apply a discrete mask to the data, segmenting the image into ECFP, EYFP, and background.

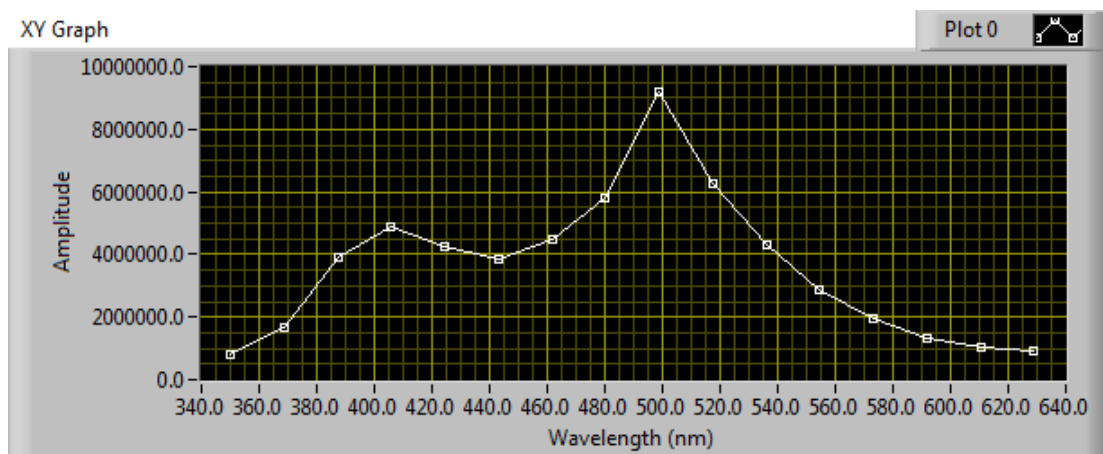


**Figure 6.6. Spectral graph of zebrafish eye.**

The mask in Figure 6.7 represents the discretized image of the zebrafish eye. Each pixel is processed and assigned a color. Black if there is no signal, blue if the signal is most likely ECFP, and green if the signal is most likely EYFP. This information can be used to identify the corresponding fluorescent signal of the fluorophore as well as determine color assignment when processing an image.

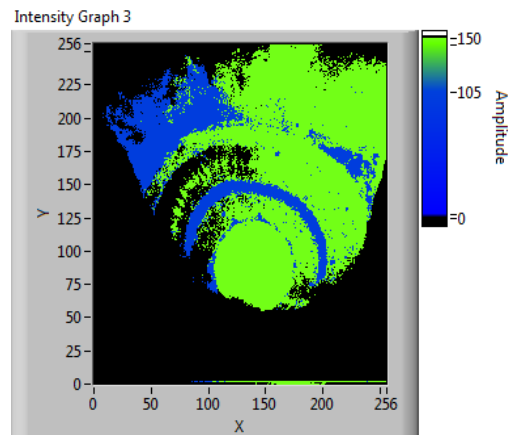


**Figure 6.7. Discrete masking of the zebrafish eye.**

Isolating the individual reporters within the image can be done using simple subtraction between channels. By taking the individual image corresponding to the yellow and cyan channels, subtraction from one another yields the regions of the desired fluorophore. As seen in Figure 6.8(a), subtraction from the yellow channel removes the IPL from the retina in the eye. The remaining signal from the bipolar neurons remains strong and visible. Figure 6.8(b) performs the same subtraction, only this time removing yellow from cyan. The resultant image isolates the IPL as the membranous-tagged reporter.

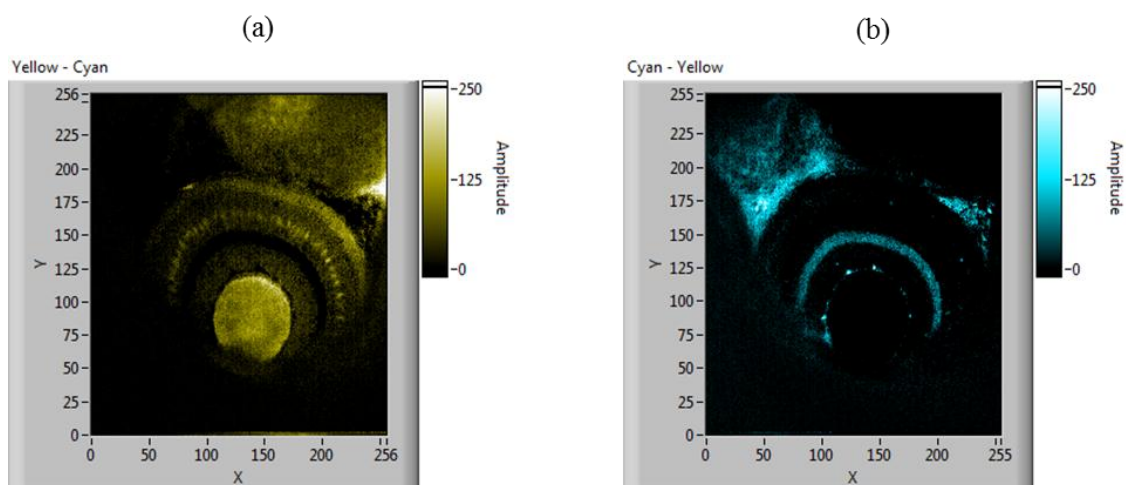


**Figure 6.8. Spectral subtraction to isolate (a) EYFP and (b) ECFP.**

Endogenous autofluorescence must be accounted for as well. To identify and exclude the signal caused by autofluorescence, we use a wild type zebrafish with no exogenous reporters as seen in Figure 6.9. We can clearly identify the areas where untagged bipolar neurons would exist. The IPL, although visible, is much weaker in signal intensity.

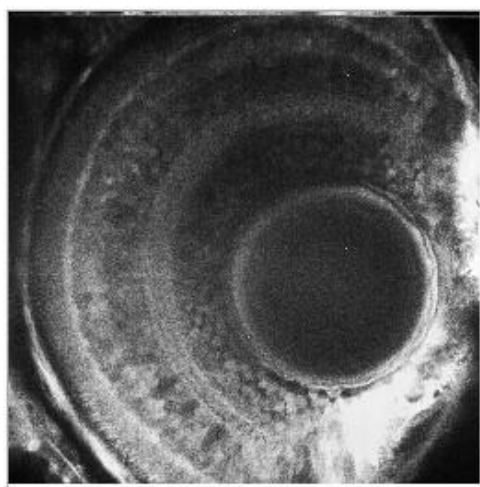


**Figure 6.9. Autofluorescence of wild-type zebrafish.**

After identifying the desired fluorescent markers, we can recombine the initial dataset and color the morphologically relevant portions of the image as shown in Figure 6.10(a). The image shows expression of ECFP and EYFP reporters within the eye, with false-colors blue representing ECFP and yellow representing EYFP. Using the wild-type zebrafish to identify autofluorescence, the corresponding signal is left in grayscale. The white box marks a region of distinguishable bipolar interneurons, with the overexposure in the right part of the eye caused by the angle of the fish during imaging. The dominant cyan band marked by the arrow within the retina represents the IPL. Figure 6.10(b) decreases the field of view and displays a close-up of the retina, allowing for a better look at the neurons. These results show that NOMSISv2 is a valid spectral system for NLOM, obtaining useful results in biological systems regardless of the reduction observed in the SNR.

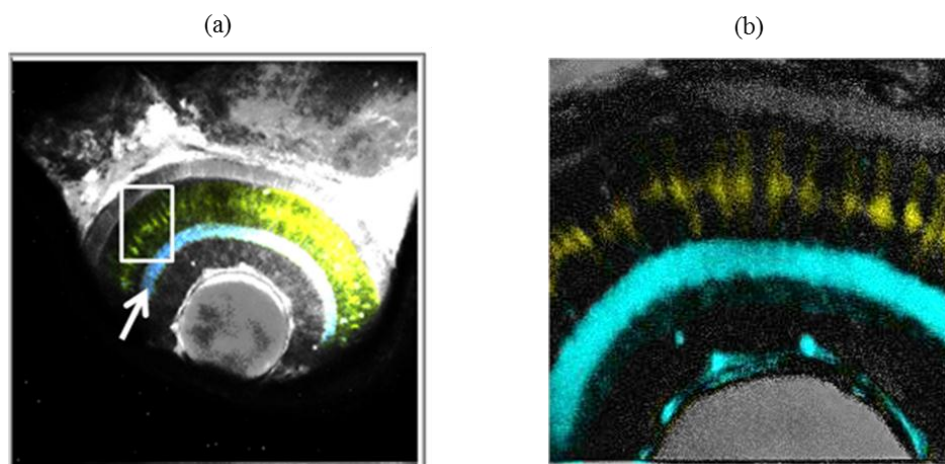


**Figure 6.10. Multicolor zebrafish eye expressing ECFP and EYFP with a view (a) of the whole eye and (b) zoomed into the retina.**

## CHAPTER VII

### CONCLUSION AND RECOMMENDATIONS

This study encompassed the development and benefits of using NLOM as a valid form of spectral imaging. Using the LabVIEW Professional Development System, we developed an in-house NLOM system for two-channel imaging in multiple dimensions known as NOMS. Using optical filters, the system is capable of targeting reporters of known emission wavelengths and generates respective intensity images. NOMS was validated by a three-dimensional acquisition of a mouse tail tendon. The system is still used regularly by the Tissue Microscopy Lab for two-channel data acquisition.

Because an ultrashort pulse laser allows for simultaneous excitation of multiple fluorophores across a large spectrum, acquisition of more than two nonlinear signals required a new method of collection which motivated development of NOMSISv1. Using a multimode fiber-optic cable, delivery of fluorescent signal occurred in a spectrometer isolated from the microscope. A multi-channel PMT detected optical signals which were diffracted through a grating and allowed for spectral imaging of a biological system on-the-fly. An angiogenesis model demonstrated the system's capabilities of spectral delineation.

Limited DMA channels prevented the system from collecting images at speeds faster than 16 seconds. The desire for high-speed imaging motivated the development of

NOMSISv2. Overcoming this limitation required the use of an FPGA, which also came with an updated discriminator array. Updating the system motivated a change in the optics as well. A spectrometer directly coupled to the microscope was chosen in hopes to increase optical collection efficiency and optimize SNR. Experimental comparison between the two systems contradicted the calculations, as SNR in NOMSISv2 declined due to the counting mechanism from either the FPGA or discriminator arrays. Despite the decline in efficiency, NOMSISv2 performed well in the experimental validation of a multicolor zebrafish sample. Excitation of EYFP and ECFP yielded spectral data for bipolar interneurons and the membrane-rich IPL, respectively.

As technology develops, new methods for improving optical efficiency of the system can be utilized. Future work should involve increasing the collection efficiency of the spectral systems by identifying new optics with higher NA. Additionally, locating the source of the significant reduction in SNR is vital to further enhancement of the system. Whether the reduction was induced by the decrease in photon counting speed required by the FPGA or poor performance of the new discriminators, identifying the problem should significantly improve system performance. Since FPGA-based photon counting was limited to 20 MHz, newer technological advances should increase this limit and ultimately gain the capability to perform photon counting at ultra-high speeds. By using newer PMTs capable of 32 channels, spectral resolution may be further enhanced.

## REFERENCES

1. A. T. Yeh, H. Gibbs, J. J. Hu, and A. M. Larson, "Advances in nonlinear optical microscopy for visualizing dynamic tissue properties in culture," *Tissue Engineering Part B Rev.* **14**(1), 119-31 (2008).
2. R. K. Benninger, M. Hao, and D. W. Piston, "Multi-photon excitation imaging of dynamic processes in living cells and tissues," *Reviews of Physiology, Biochemistry, and Pharmacology* **160**, 71-92 (2008).
3. P. P. Provenzano, C. T. Rueden, S. M. Trier, L. Yan, S. M. Ponik, D. R. Inman, P. J. Keely, and K. W. Eliceiri, "Nonlinear optical imaging and spectral-lifetime computational analysis of endogenous and exogenous fluorophores in breast cancer," *Journal of Biomedical Optics* **13**, 031220 (2008).
4. A. Leray and J. Mertz, "Rejection of two-photon fluorescence background in thick tissue by differential aberration imaging," *Optics Express* **14**, 10565-10573 (2006).
5. P. Theer and W. Denk, "On the fundamental imaging-depth limit in two-photon microscopy," *Journal of the Optical Society of America A* **23**, 3139-3149 (2006).
6. S. Pang, A. T. Yeh, C. Wang, and K. E. Meissner, "Beyond the  $1/T_p$  limit: two-photon-excited fluorescence using pulses as short as sub-10-fs," *Journal of Biomedical Optics* **14**, 054041 (2009).



7. A. J. Radosevich, M. B. Bouchard, S. A. Burgess, B. R. Chen, and E. M. C. Hillman, "Hyperspectral in vivo two-photon microscopy of intrinsic contrast," *Optics Letters* **33**, 2164-2166 (2008).
8. G. Faraco and L. Gabriele, "Using LabVIEW for applying mathematical models in representing phenomena," *Computers & Education* **49**(3), 856-872 (2007).
9. M. A. Alia, T. M. Younes, and S. A. Alsabbah, "A design of a PID self-tuning controller using LabVIEW," *Journal of Software Engineering and Applications* **4**(3), 161-171 (2011).
10. M. A. Alia, T. M. Younes, and M. A. Zalata, "Development of equivalent virtual instruments to PLC functions and networks," *Journal of Software Engineering and Applications* **4**(3), 172-180 (2011).
11. J. Herrmann, "Theory of Kerr-lens mode locking: role of self-focusing and radially varying gain," *Journal of the Optical Society of America B* **11**, 498-512 (1994).
12. T. Brabec, C. Spielmann, P. F. Curley, and F. Krausz, "Kerr lens mode locking," *Optics Letters* **17**(18), 1292-1294 (1992).
13. A. M. Larson, A. Lee, P.-F. Lee, K. J. Bayless and A. T. Yeh, "Ultrashort pulse, multispectral nonlinear optical microscopy," *Journal of Innovative Optical Health Sciences* **2**(1), 27-35 (2009).
14. J. Huth, M. Buchholz, J. M. Kraus, M. Schmucker, G. Wichert, et al., "Significantly improved precision of cell migration analysis in time-lapse video

- microscopy through use of a fully automated tracking system," *BMC Cell Biology* **11**(24), 1-12 (2010).
15. C. Buehler, K. H. Kim, U. Greuter, N. Schlumpf, and P. T. C. So, "Single-photon counting multicolor multiphoton fluorescence microscope," *Journal of Fluorescence* **15**, 41-51 (2005).
  16. L. Yan, C. T. Rueden, J. G. White, and K. W. Eliceiri, "Applications of combined spectral lifetime microscopy for biology," *Biotechniques* **41**(3), 249-253 (2006).
  17. F. Helmchen and W. Denk, "Deep tissue two-photon microscopy," *Nature Methods* **2**, 932-940 (2005).
  18. A. K. Dunn, V. P. Wallace, M. Coleno, M. W. Berns, and B. J. Tromberg, "Influence of optical properties on two-photon fluorescence imaging in turbid samples," *Applied Optics* **39**, 1194-1201 (2000).
  19. C. B. Kimmel, W. W. Ballard, S. R. Kimmel, B. Ullmann, and T. F. Schilling, "Stages of embryonic development of the zebrafish," *Developmental Dynamics* **203**, 253-310 (1995).
  20. T. Greiling and J. I. Clark, "Early lens development in the zebrafish: a three-dimensional time-lapse analysis," *Developmental Dynamics* **238**, 2254-2265 (2009).
  21. Z. Li, N. M. Joseph, and S. S. Easter, "The morphogenesis of the zebrafish eye, including a fate map of the optic vesicle," *Developmental Dynamics* **218**, 175-188 (2000).

22. J. Ariga, S. L. Walker, and J. S. Mumm, “Multicolor time-lapse imaging of transgenic zebrafish: visualizing retinal stem cells activated by targeted neuronal cell ablation,” *Journal of Visualized Experiments* **43**, (2010): <http://www.jove.com/details.php?id=2093>.

## APPENDIX A

### NOMS SOURCE CODE

#### **nomsis.vi**

Primary vi file for NOMS. Although front panel names it as NOMSIS and there are controls for spectral control, the features are disabled and the software functions as a 2-channel NLOM system.

---

#### **Connector Pane**



## Front Panel

**NONLINEAR OPTICAL MICROSCOPY SPECTRAL IMAGING SYSTEM**  
v1.91

**Data Acquisition** | **Data Processing** | **Revision History** | **About**

**START**

**STOP**

**Enable Laser Divergence**

**Export Data**

Data Format  
Binary and TIFF

**Program Status**

**Scanning Specifications**

Field of View (voltage)  Integration Time (seconds)

Continuous Scan      Scans per Image   
 Multiple Scans

**Image Stack Parameters**

Enable Stack

Step Size  Number of Images

File Start Number  Data Format

Path

**Wavelength Selection (nm)**

380-395	500-515
395-410	515-530
410-425	530-545
425-440	545-560
440-455	560-575
455-470	575-590
470-485	590-605
485-500	605-620

**Full Spectrum**

Y-axis: 0 to 256  
X-axis: 0 to 256  
Color scale: 0 to -500

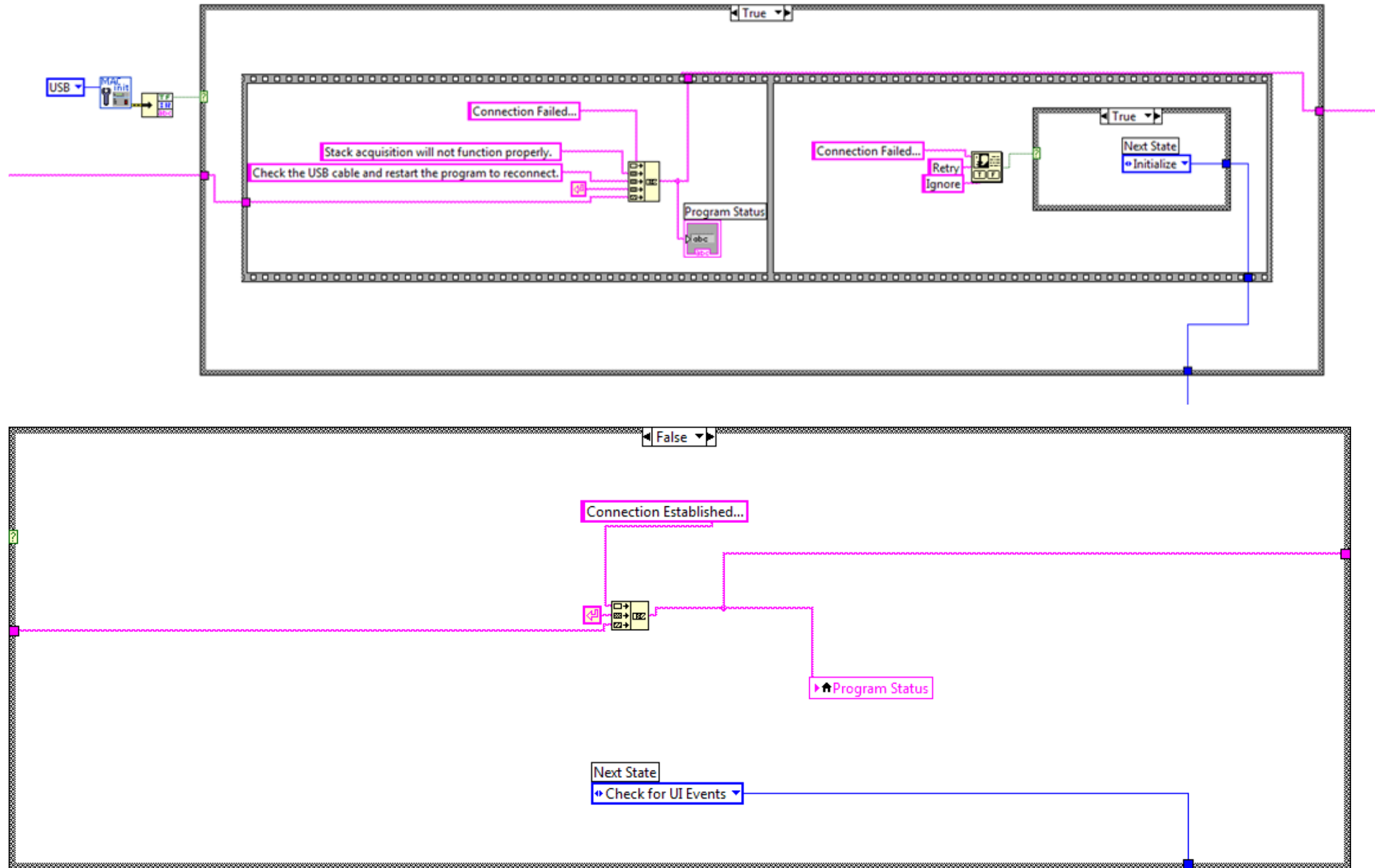
**Selected Spectra**

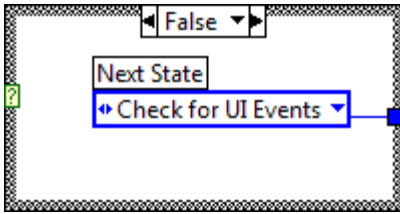
Y-axis: 0 to 256  
X-axis: 0 to 256  
Color scale: 0 to -120

Connect remotely: <http://yehgx280-3.tamu.edu/nomsis.html>

## **Block Diagram**

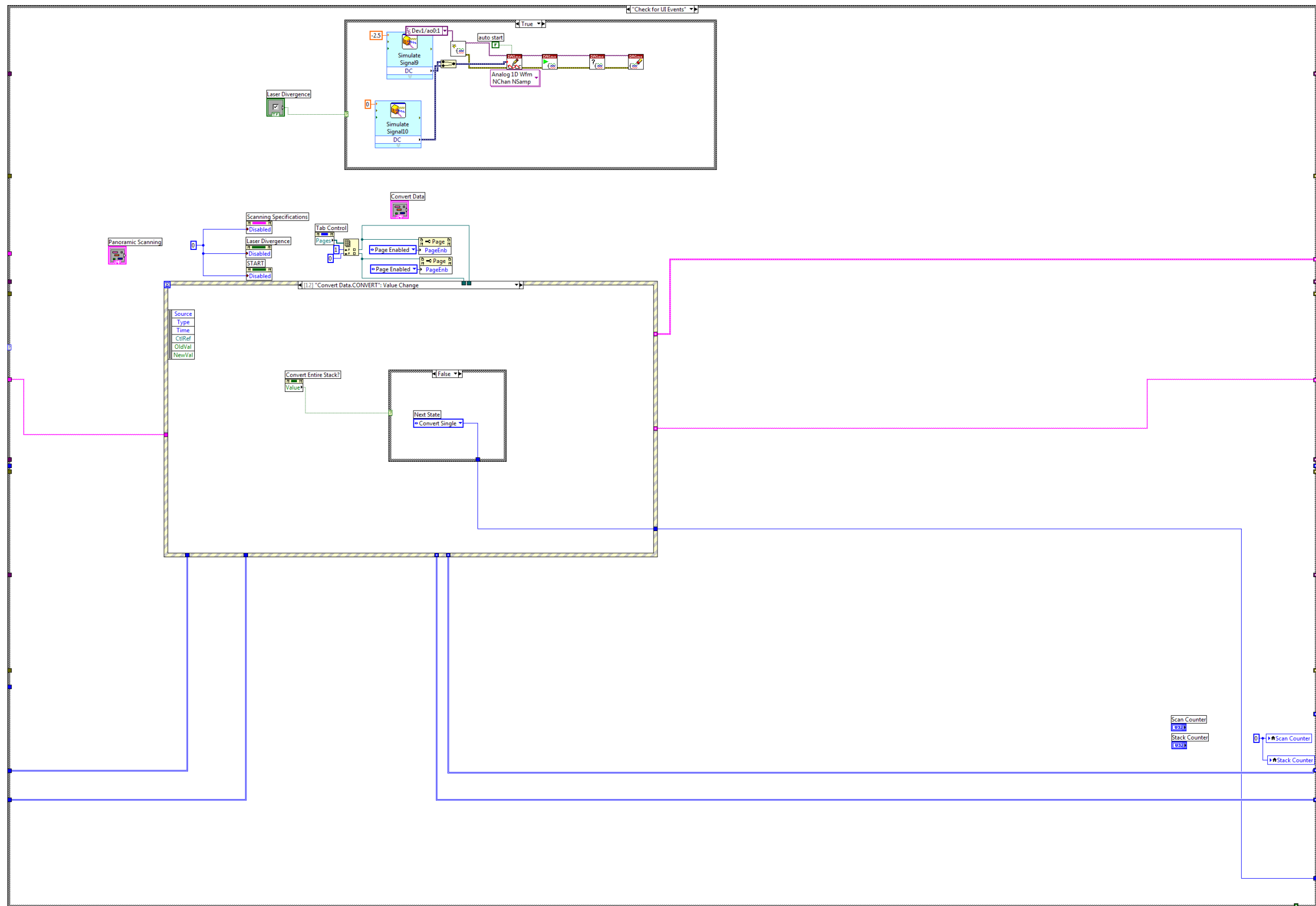
State S0 – Initialization. Sub-vi checks for proper initialization from the microscope stage. If failure, user is prompted to retry or ignore. Corresponding results will be shown in the on-screen indicator.

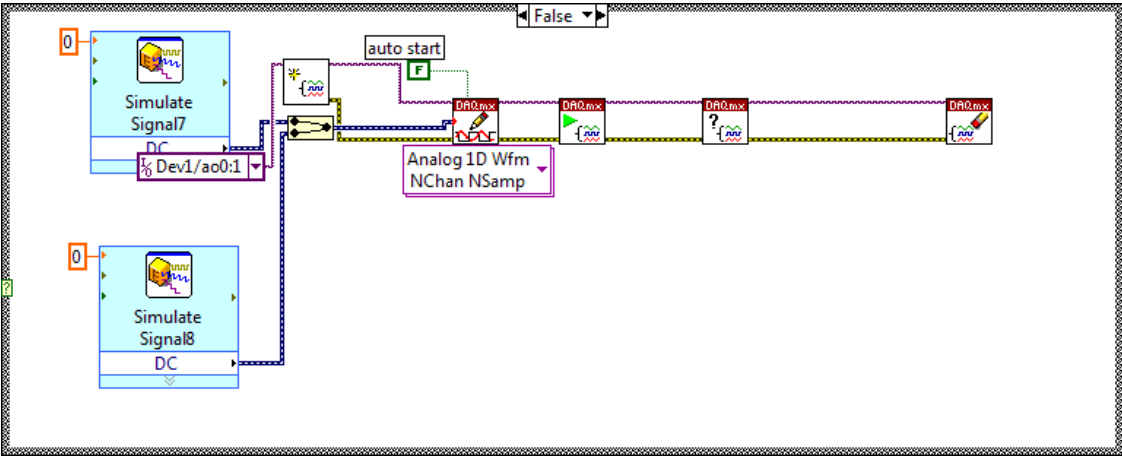




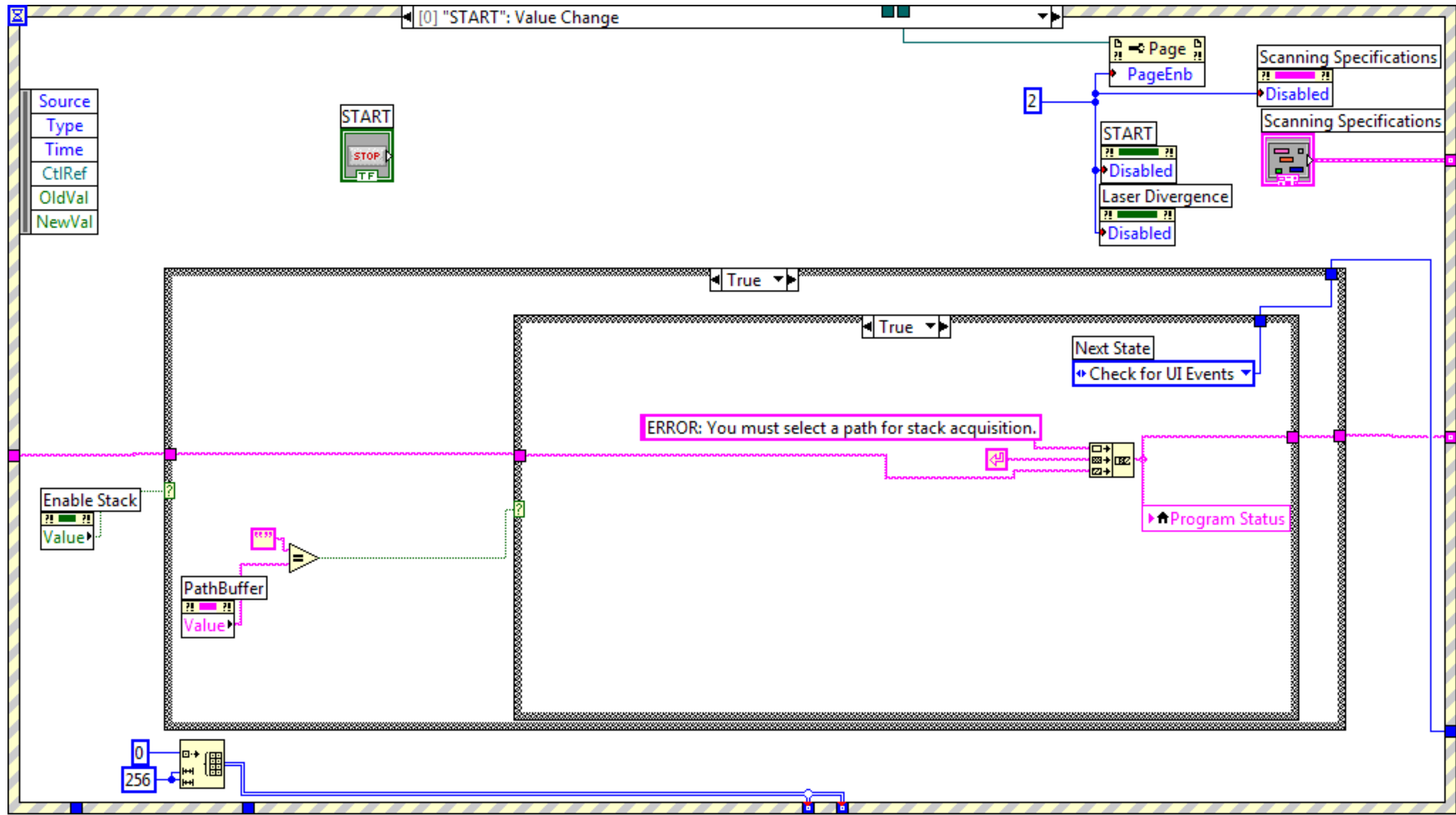
State S1 – Wait for User Input. Event structure waits for action from the user. If Laser Divergence is checked, DC voltage signals are sent to the mirrors to minimize laser-sample interaction. Controls and indicators are set to default value.

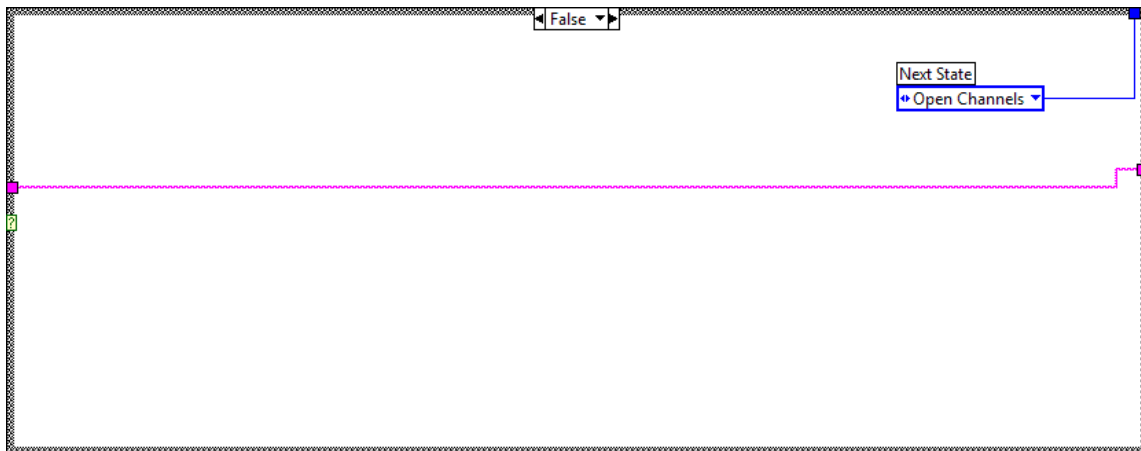




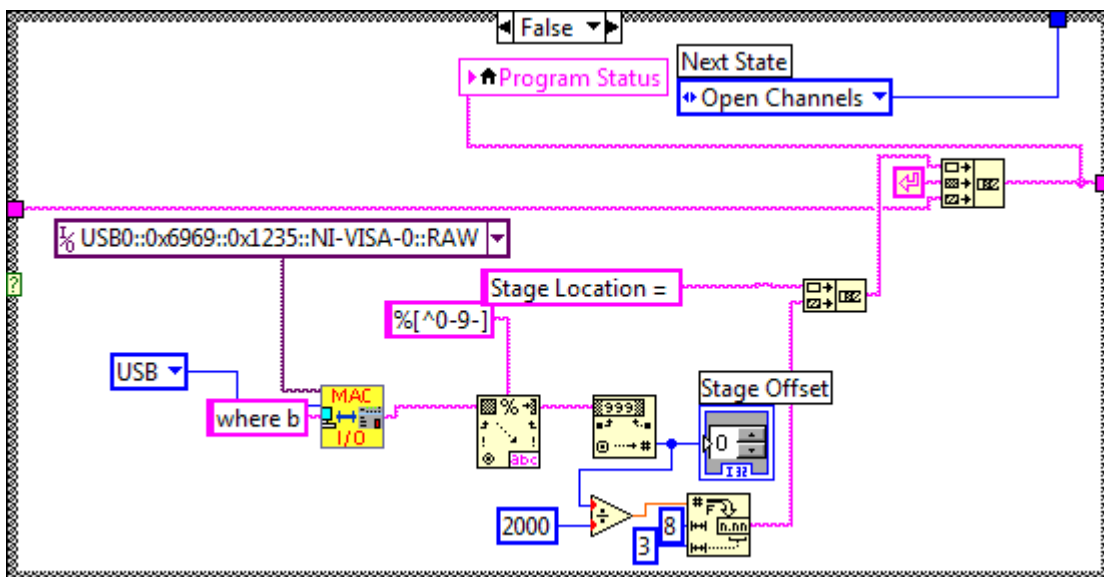


If the Start button is pressed, NOMS sets initial front panel display settings and sets the next state to S2. If other buttons are pressed, NOMS simply adjusts the visual front panel accordingly and returns to state S1.

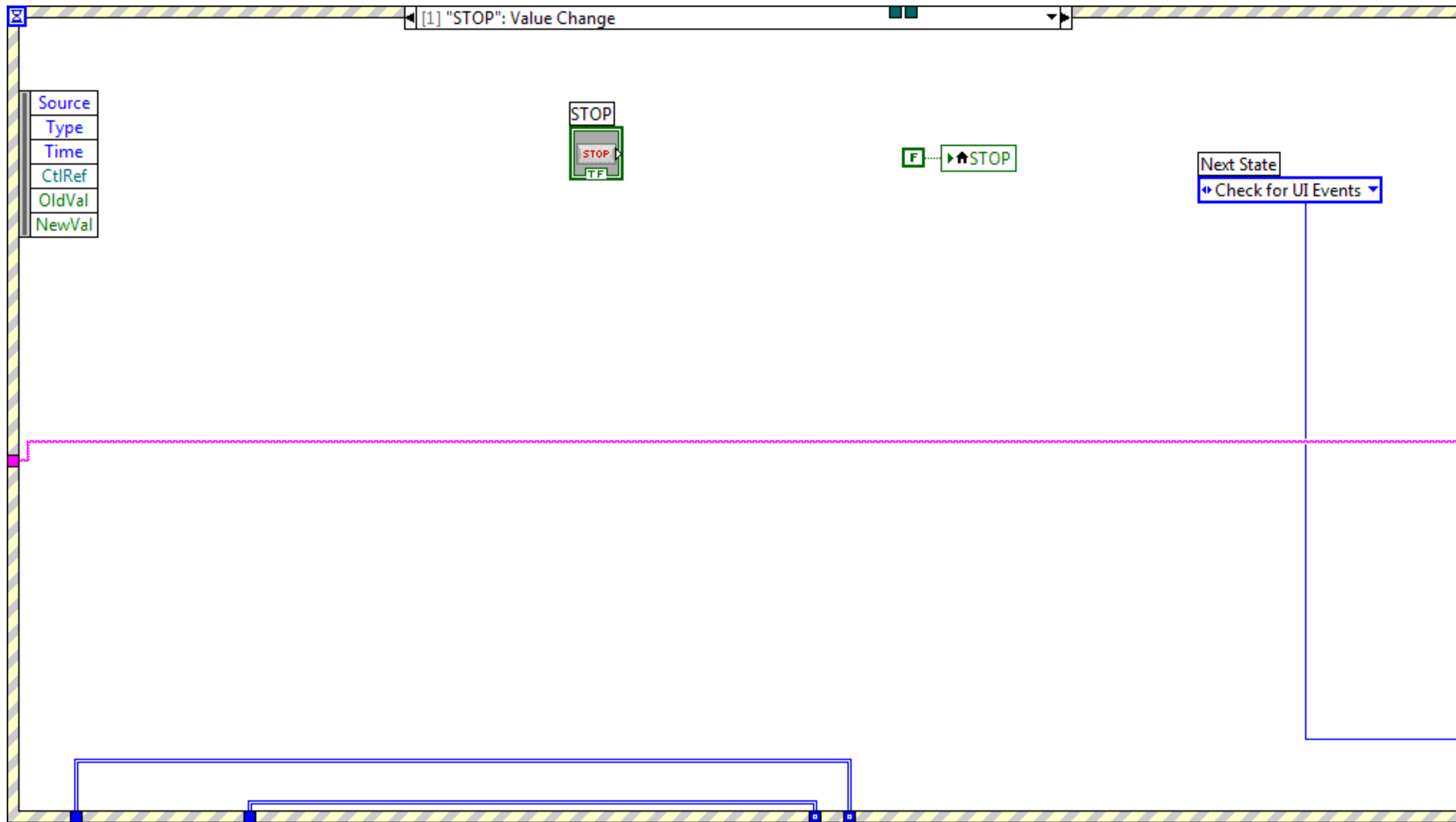




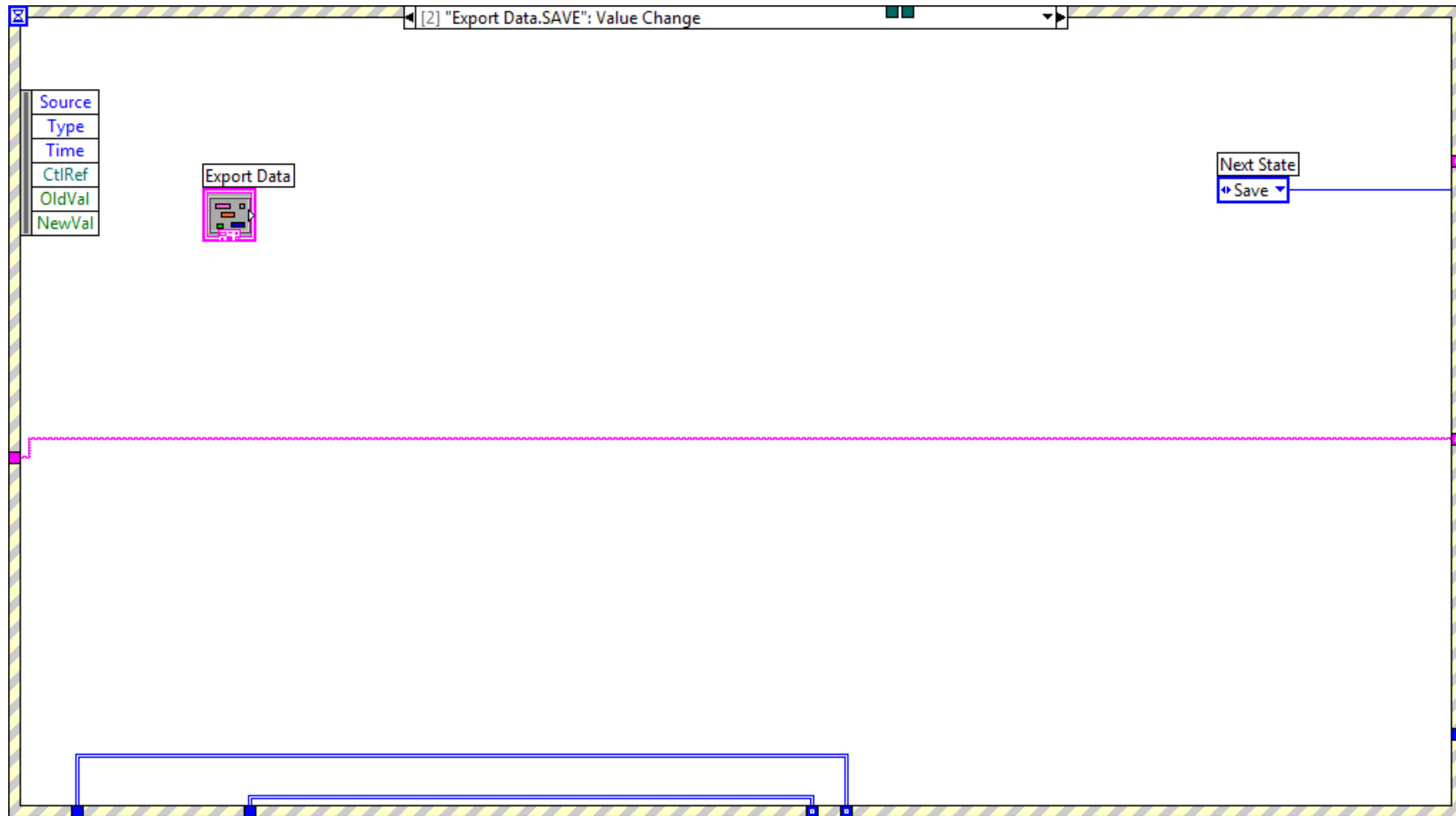
The current location of the stage is stored into the on-screen indicator. This value is also used to determine the appropriate offsets when performing 3-dimensional imaging.



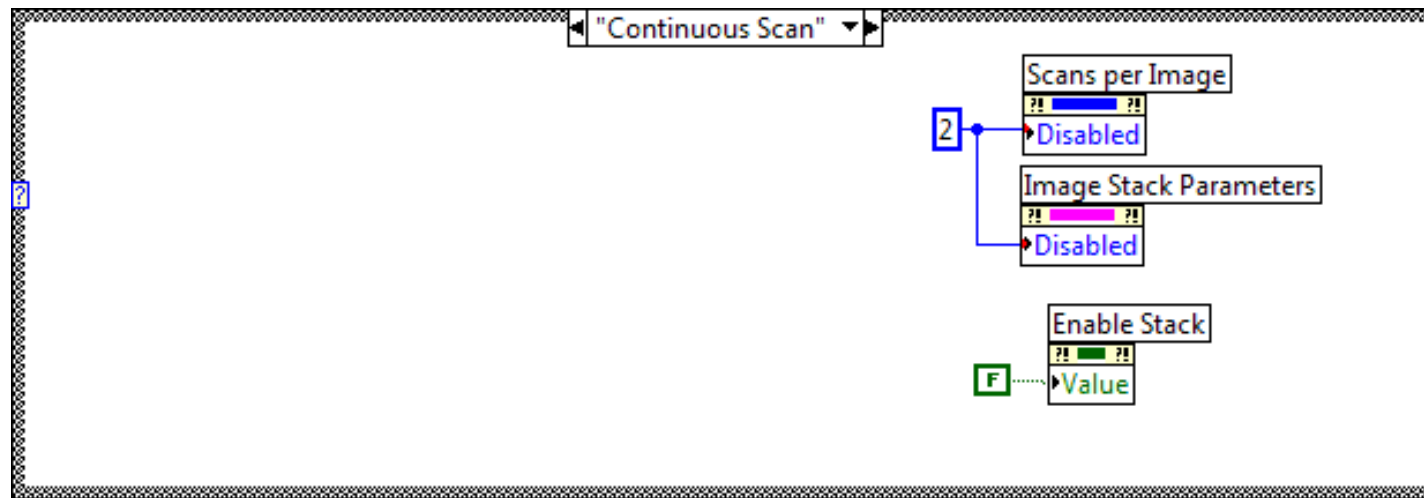
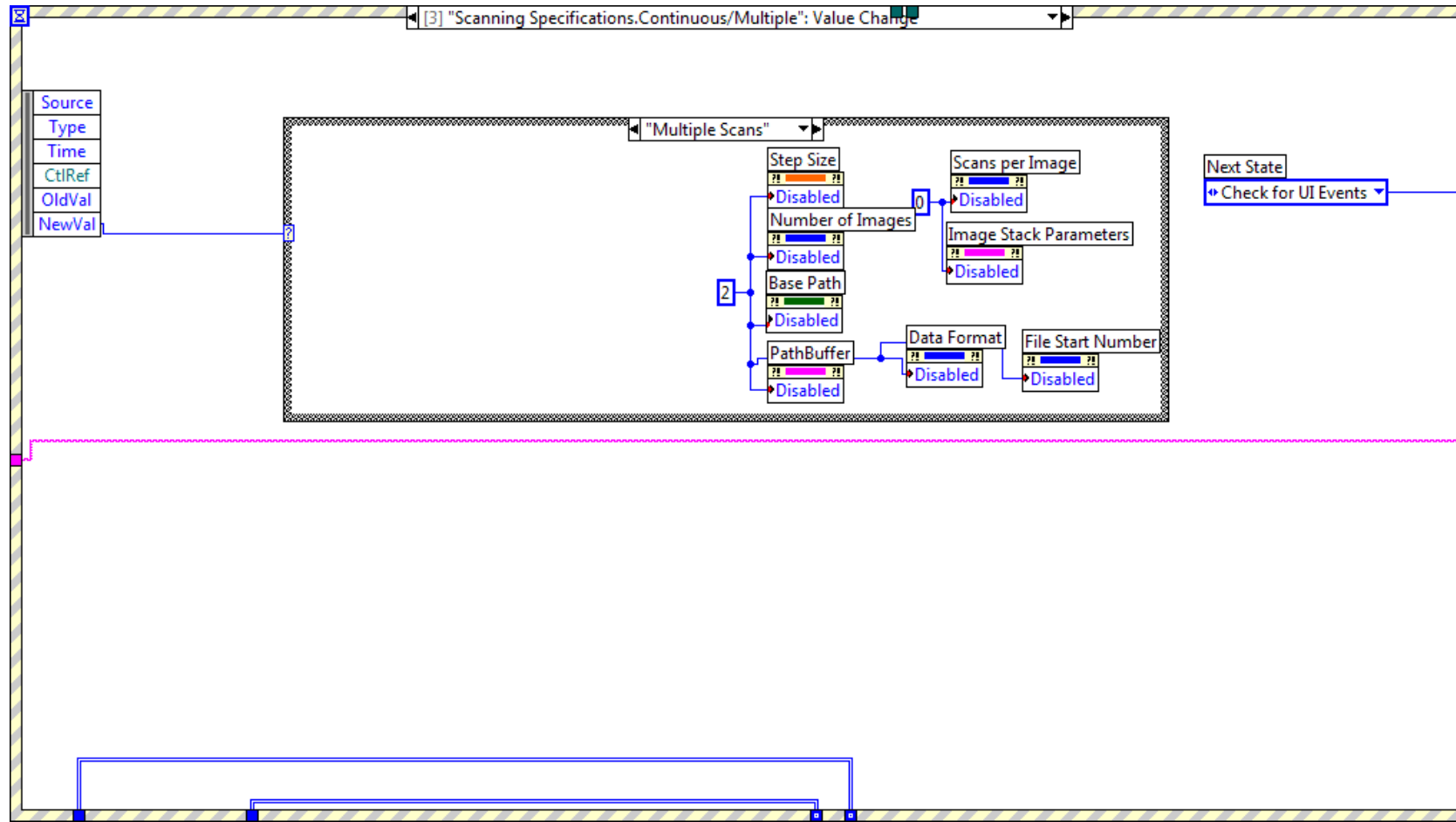
No action is taken if the Stop button is pressed during S1.



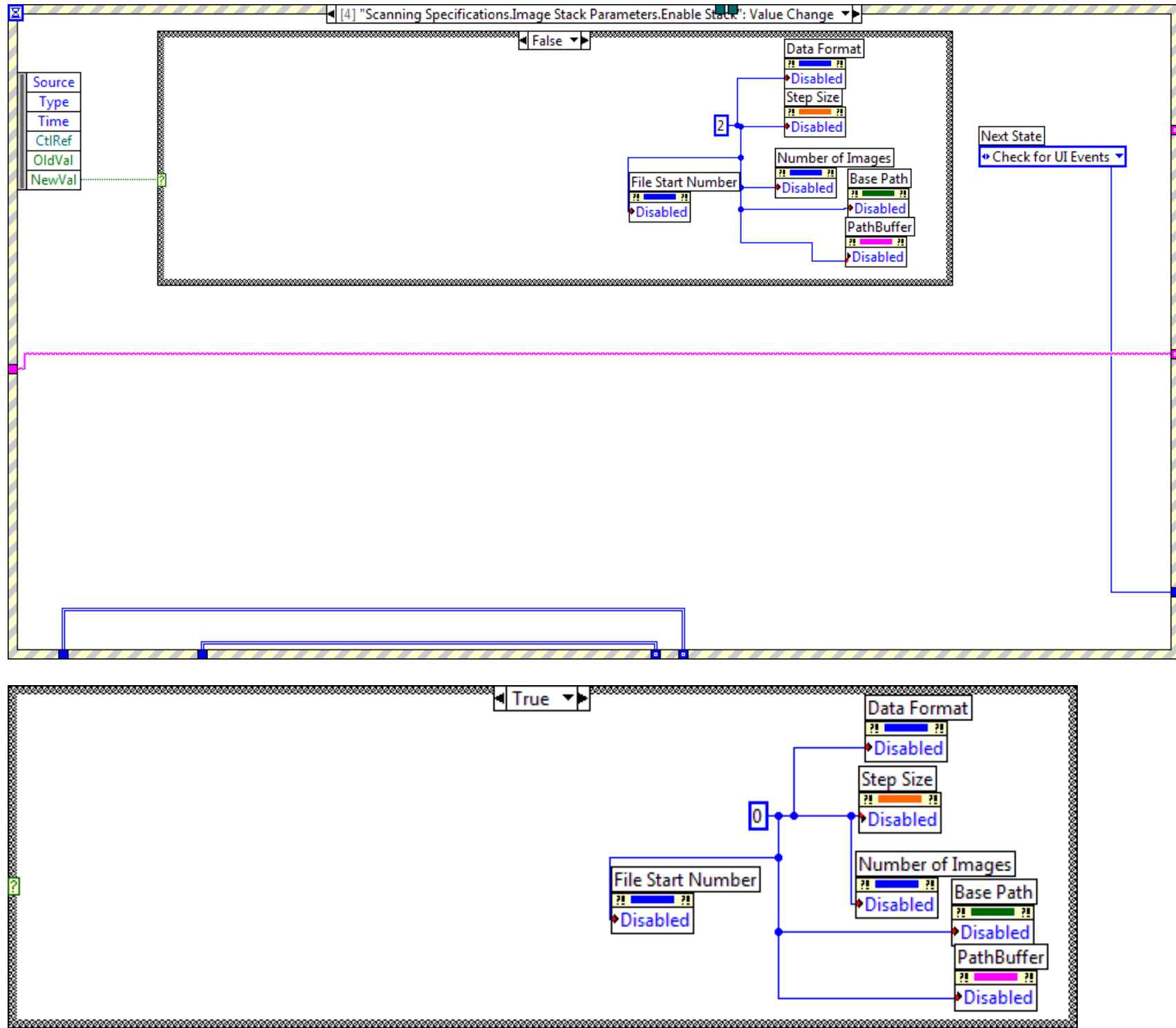
If the save button is pressed, next state is set to S5.



Aesthetic modifications.

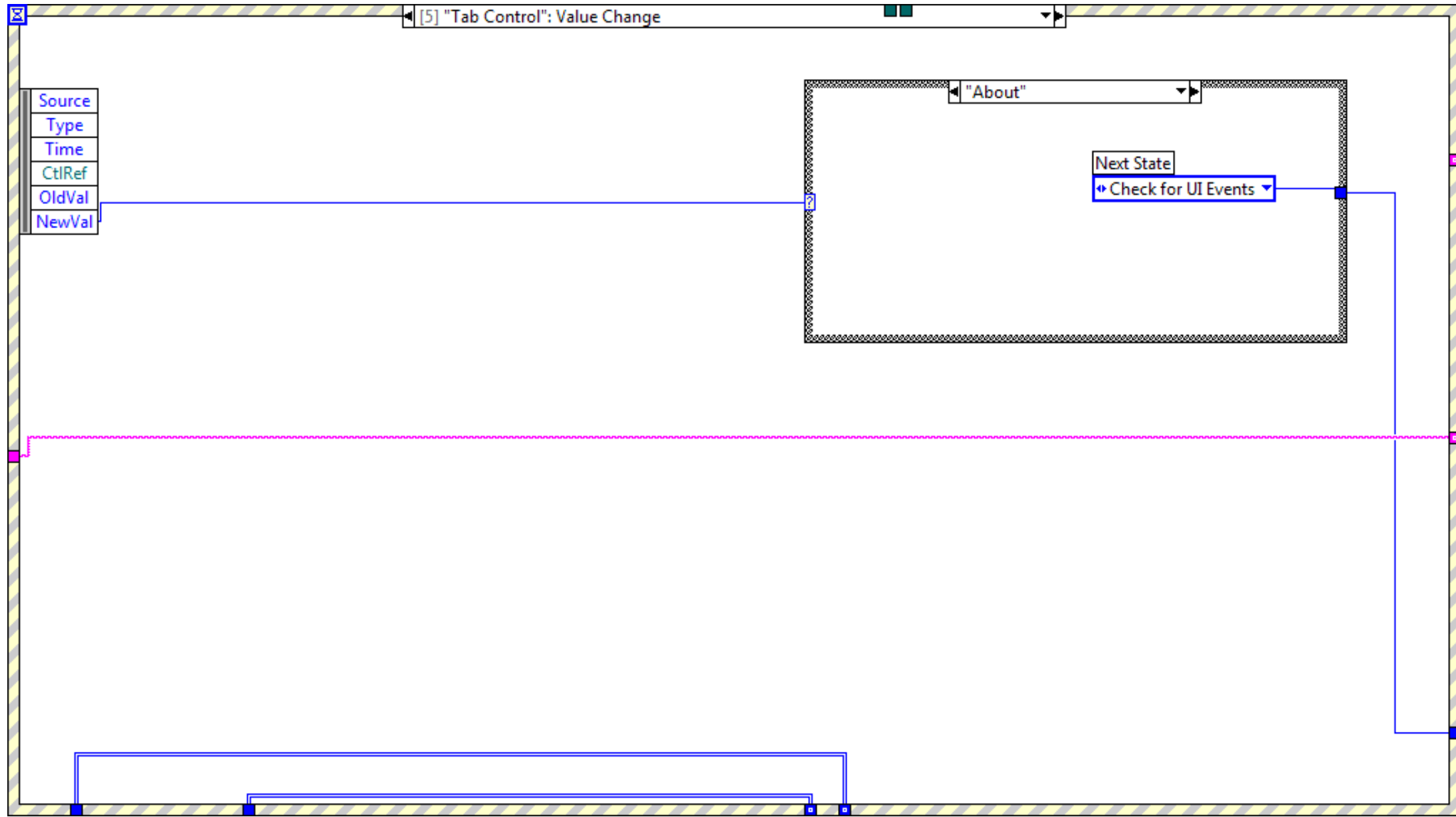


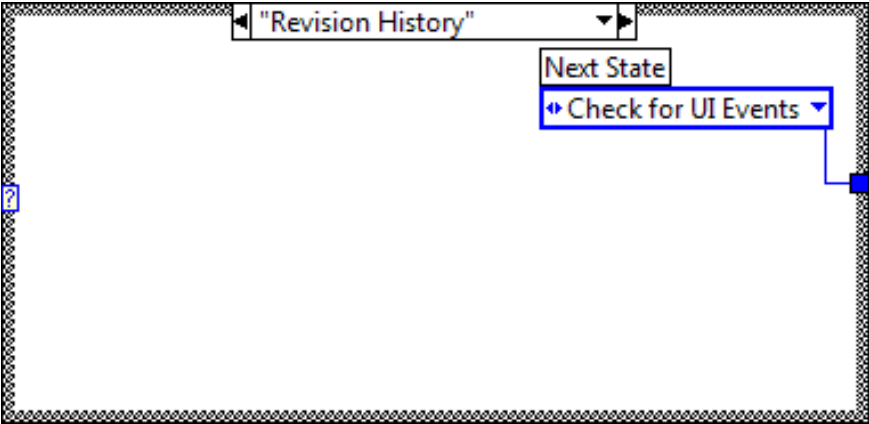
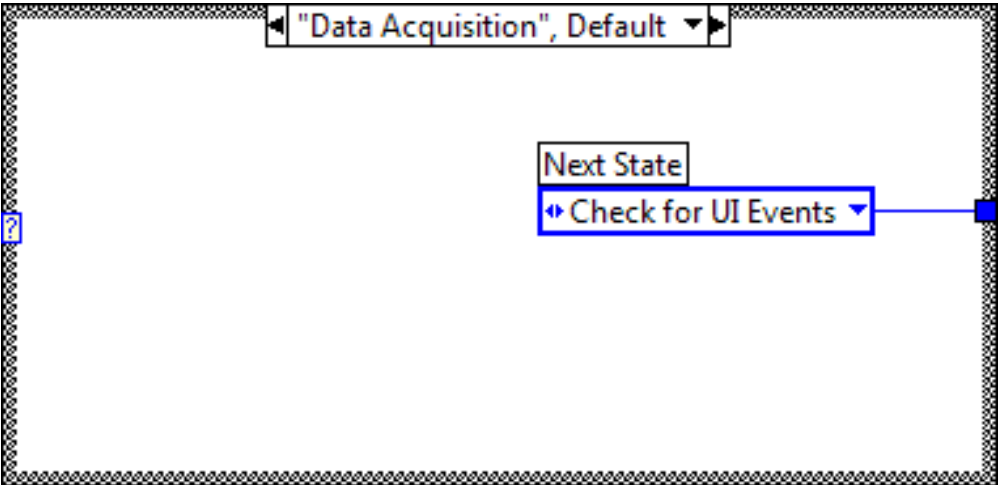
Aesthetic modifications.



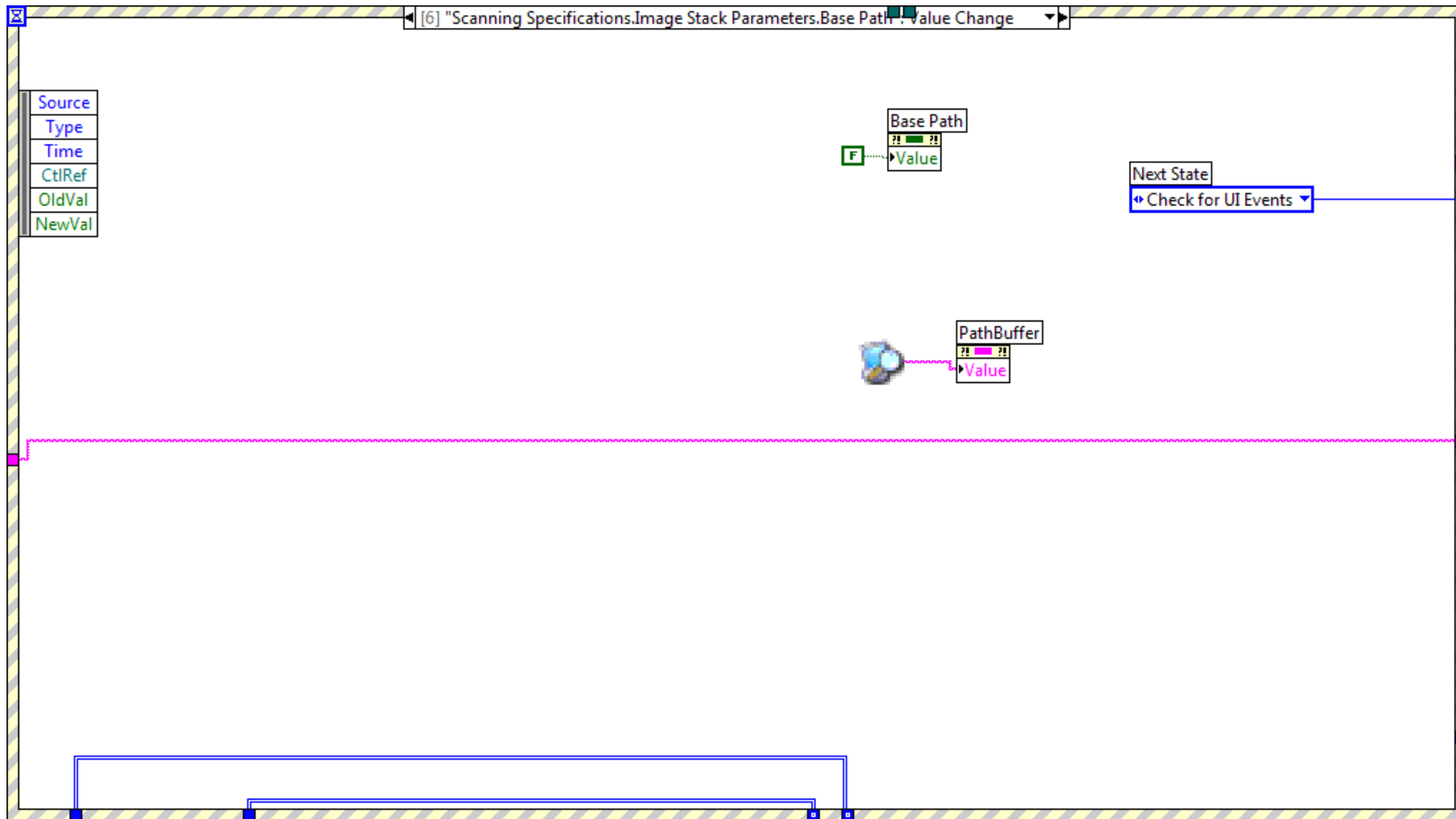


Aesthetic modifications.

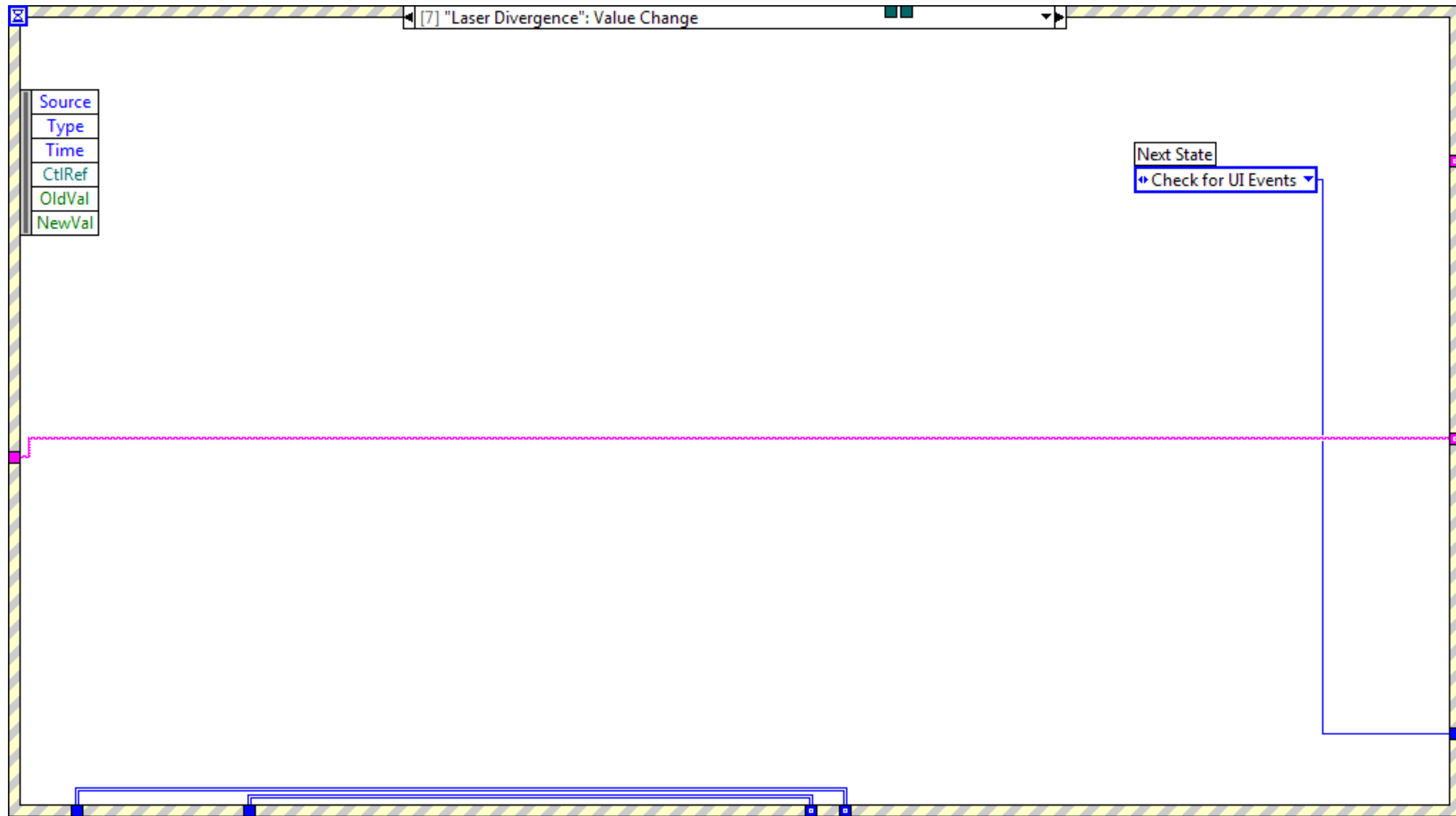




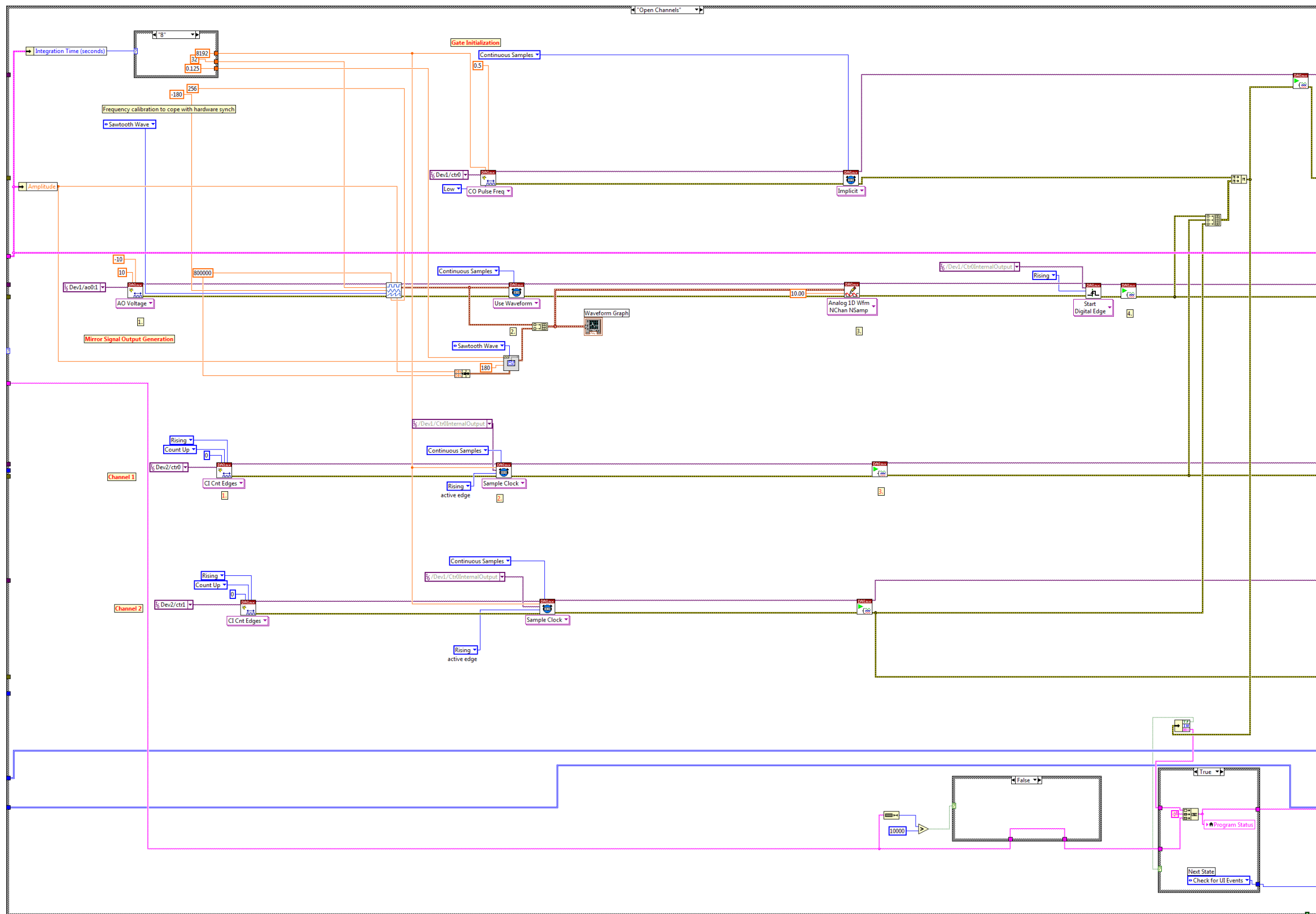
Sub-vi called when Path button is pressed. User is prompted to select a folder, and the path is stored in PathBuffer.

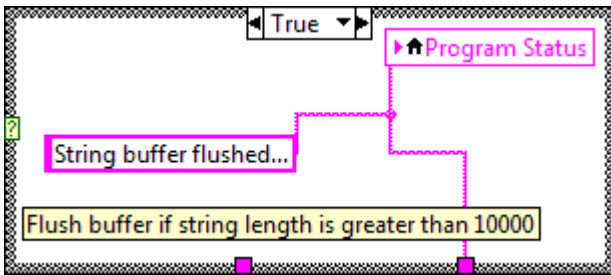
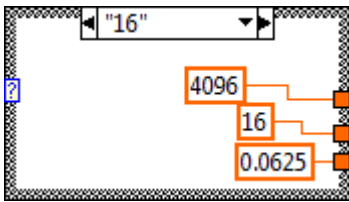
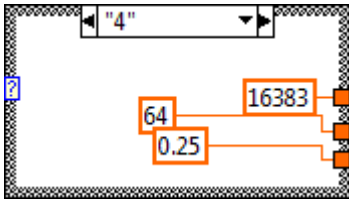
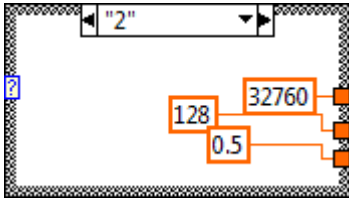
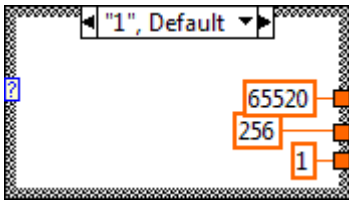


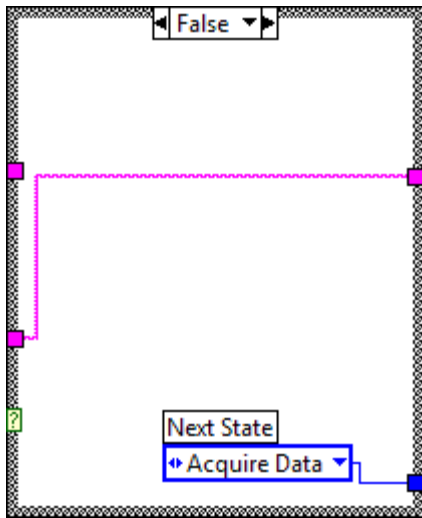
Aesthetic modifications.



State S2 – Open Channels. Pixel clock frequency is calculated based on user-inputted speed settings. A counter channel from the DAQ card initializes the waveform. Two analog output channels are initialized as well, set for amplitude and frequency based on user-specified settings. Two counter channels are activated on the counter cards for TTL pulse counting.

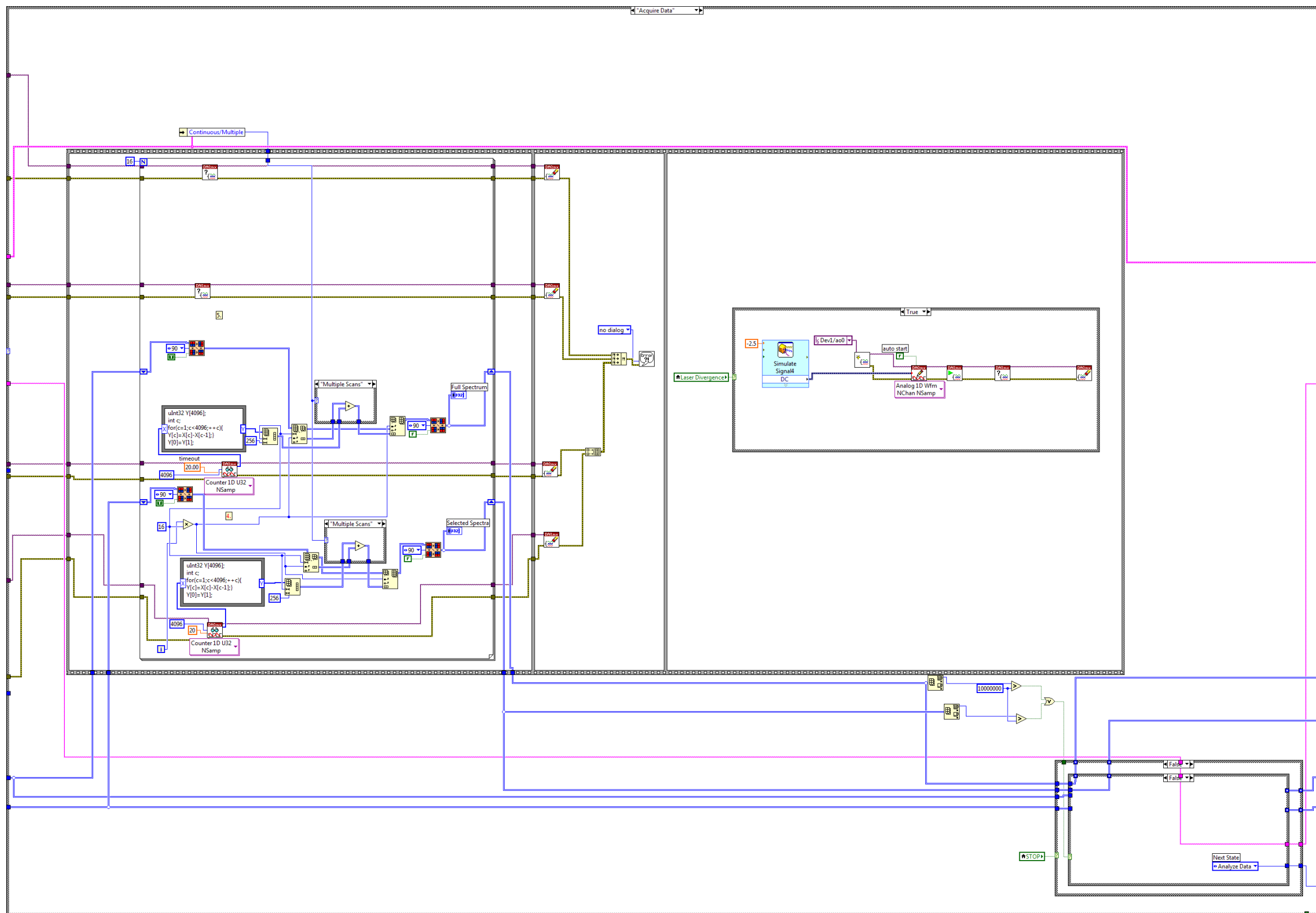


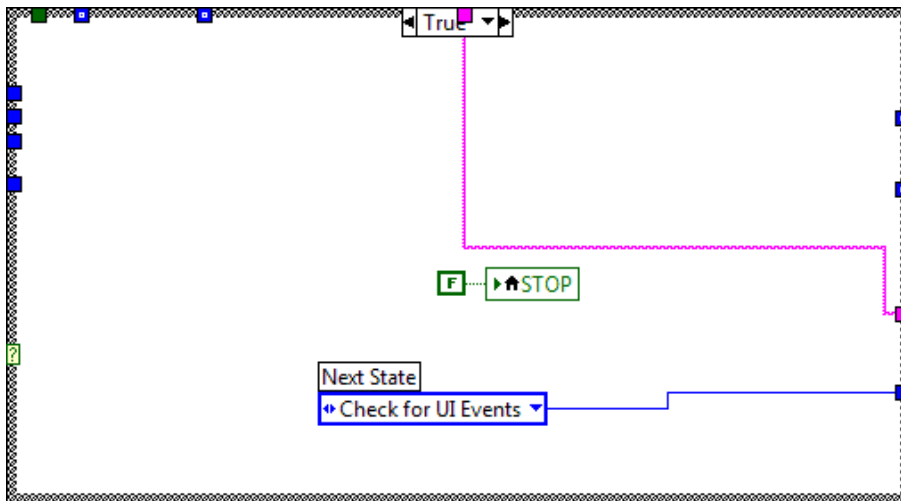
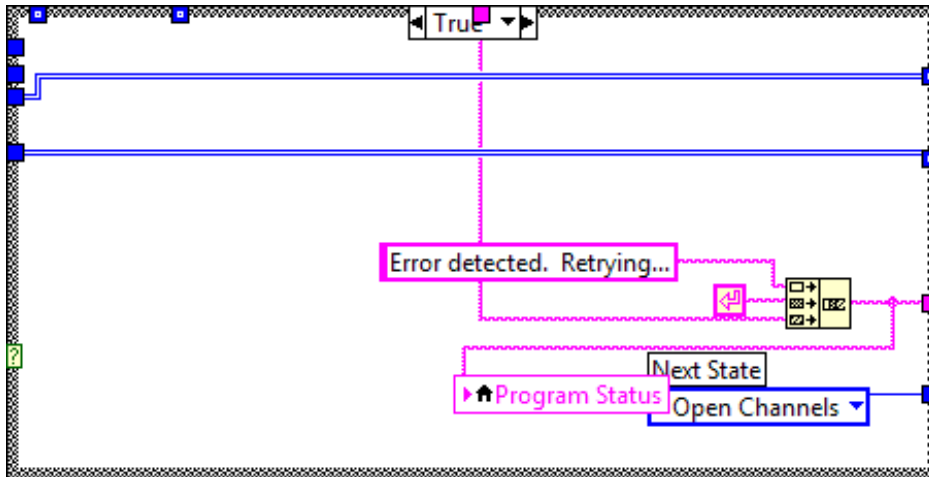
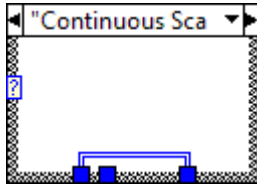
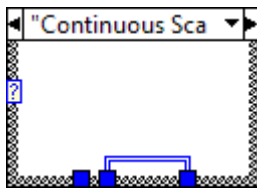


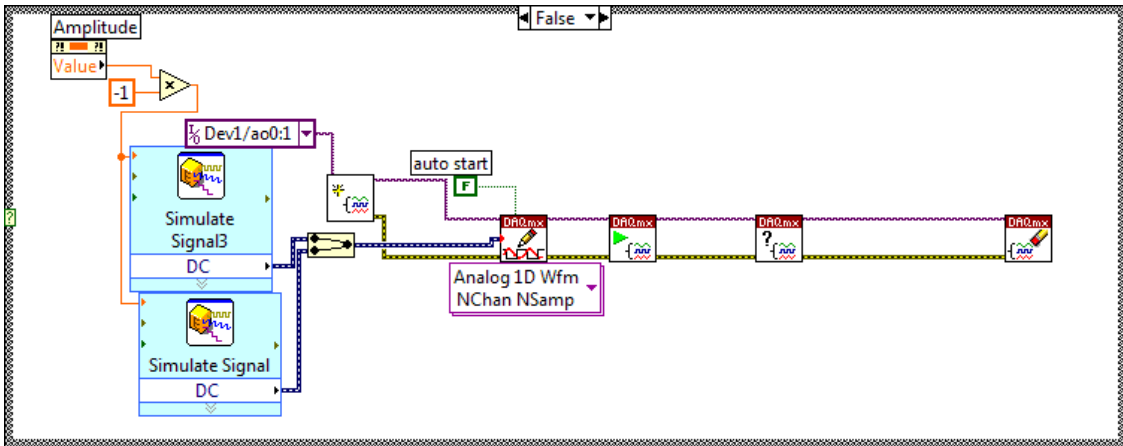




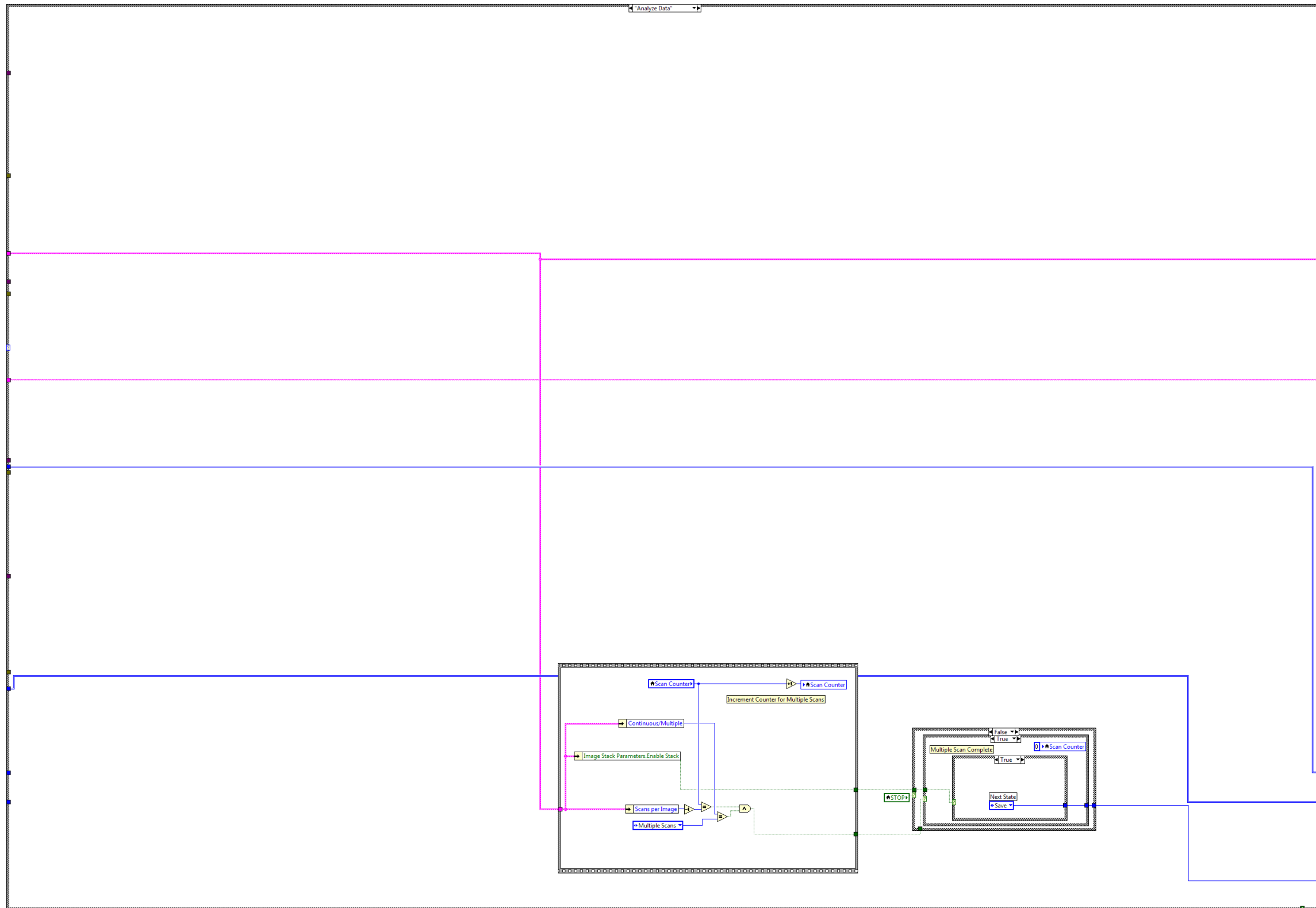
State S3 – Acquire Data. Pulses are collected by the counter cards within the for loop while the pixel clock and mirror waveforms continuously generates signal. Subtraction using a Formula Node creates actual photon count from continuously incrementing counter card data. Counts are organized into a 2-dimensional array and displayed on-screen. Upon completion, the laser is instructed to diverge from the sample.

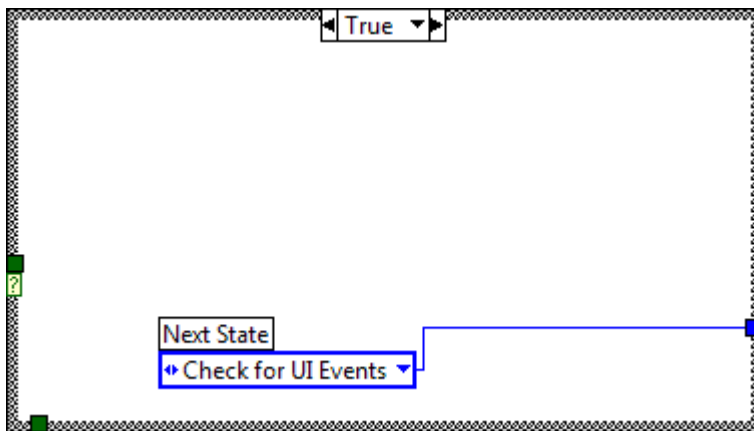
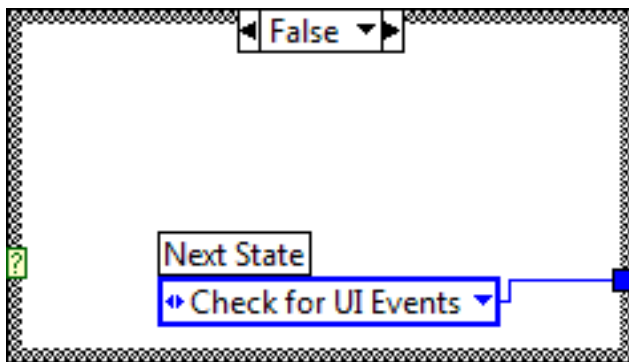
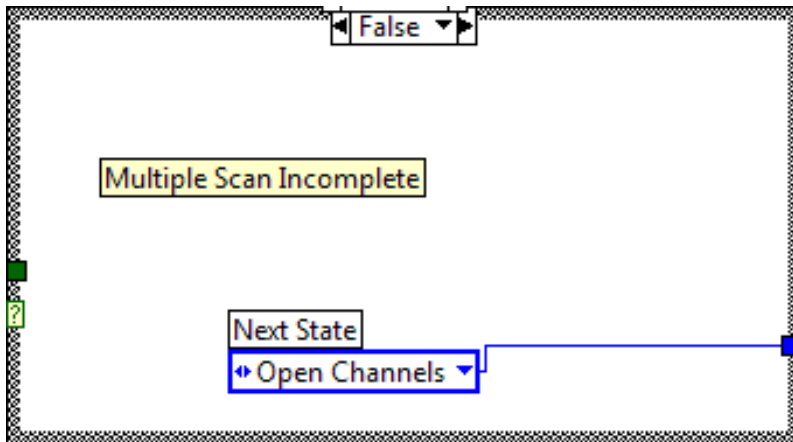


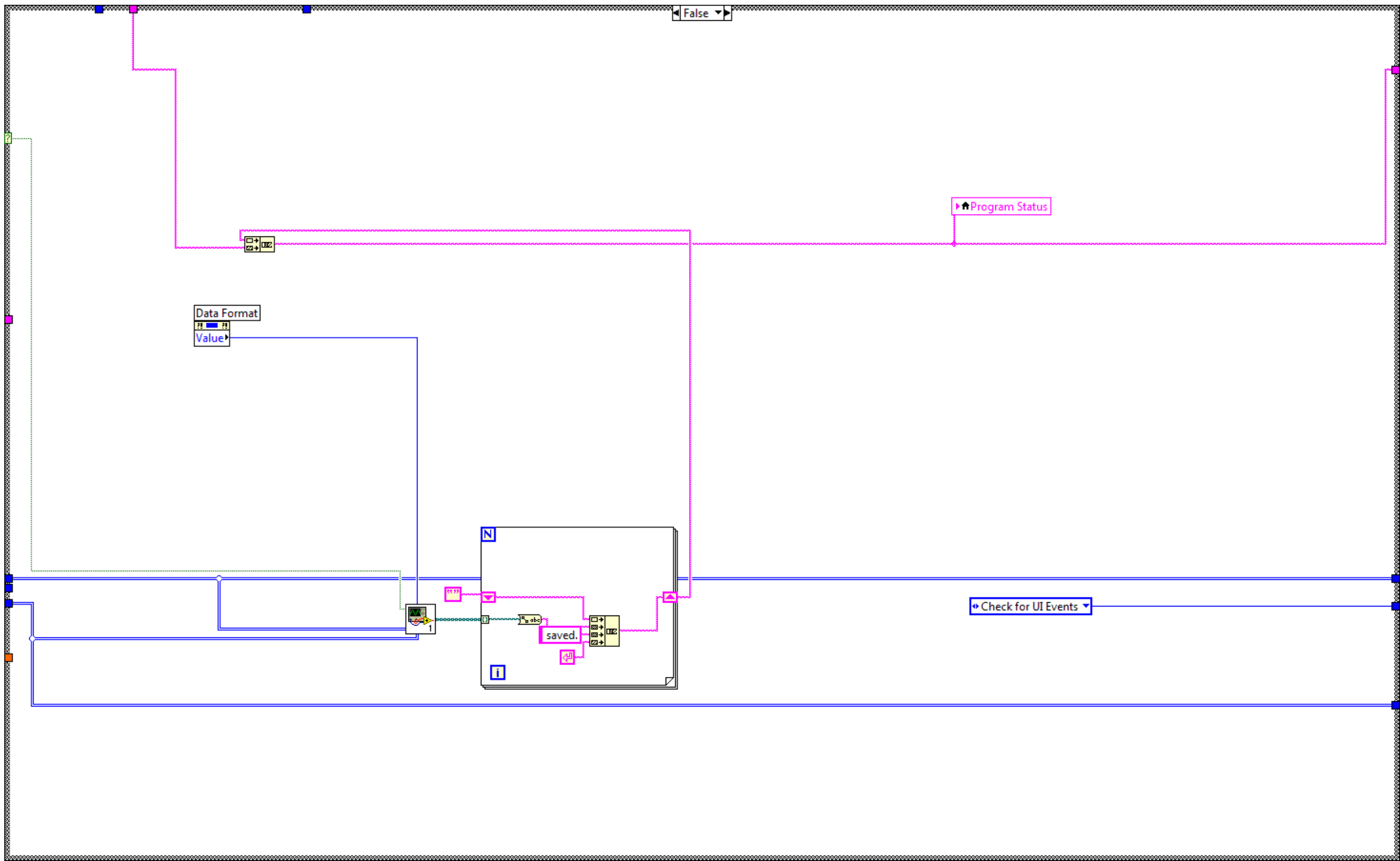




State S4 – Analyze Data. System checks progress on stack acquisition by an internal counter. If an additional scan is necessary, next state is set to S2, otherwise it is set to S5.

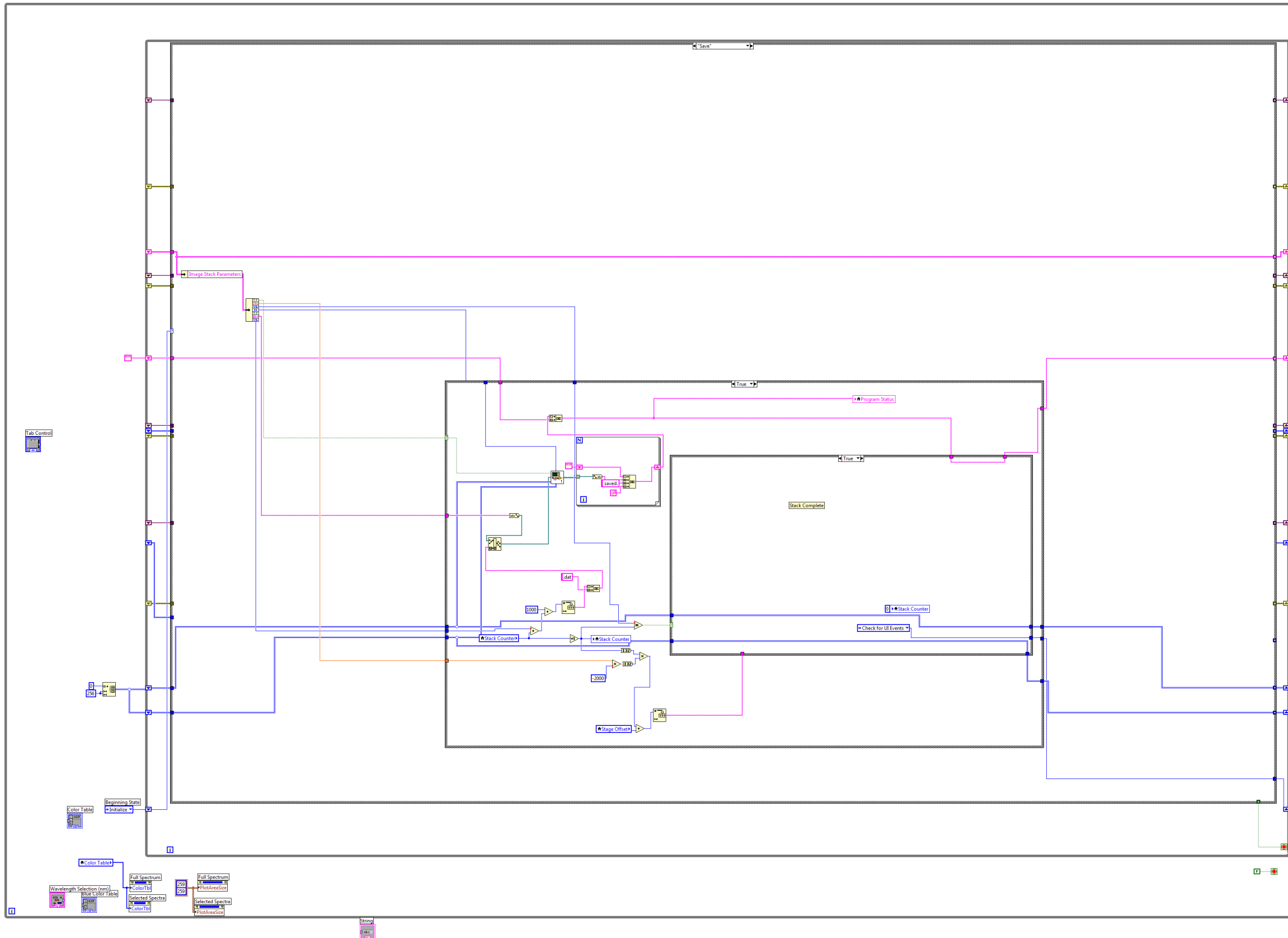


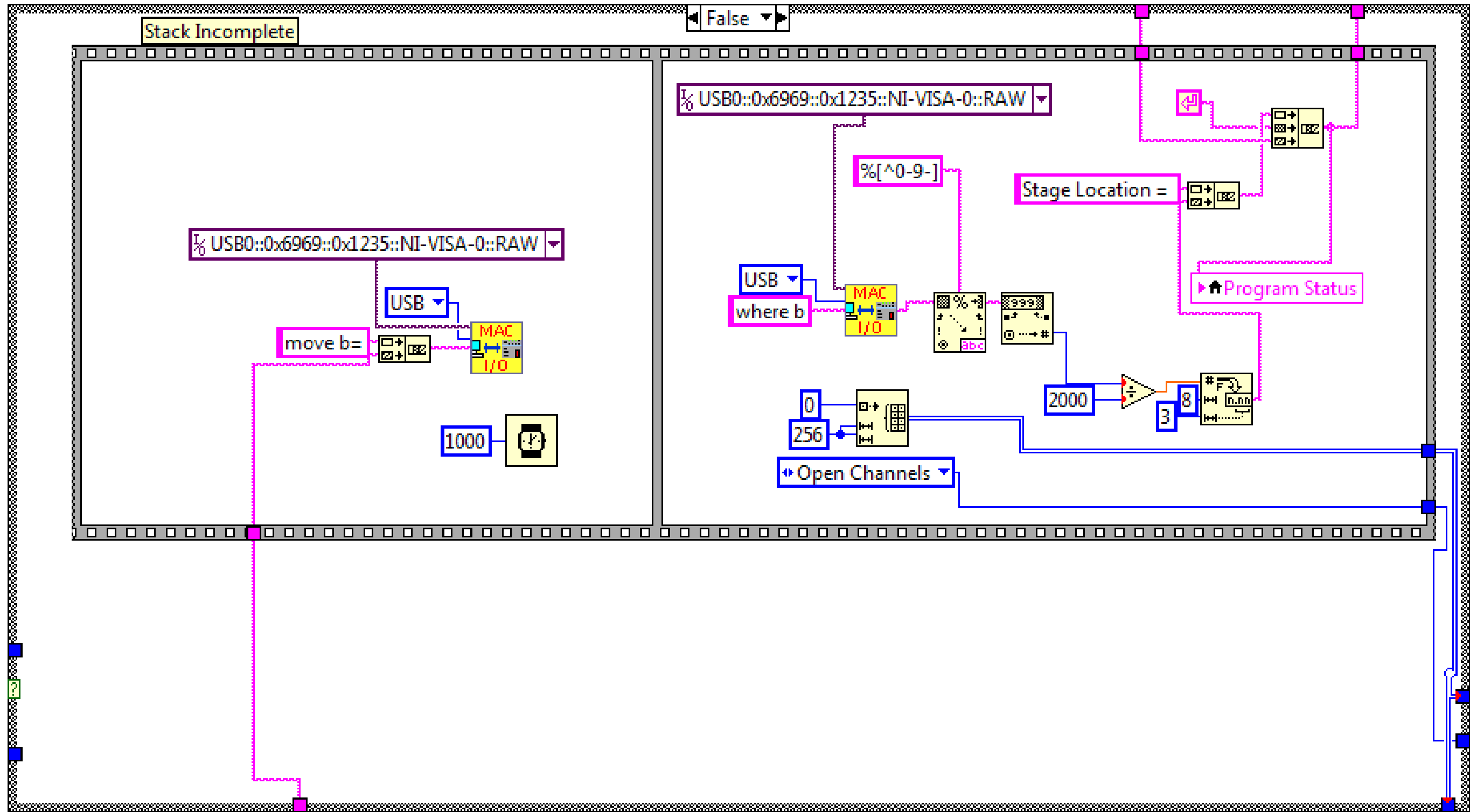




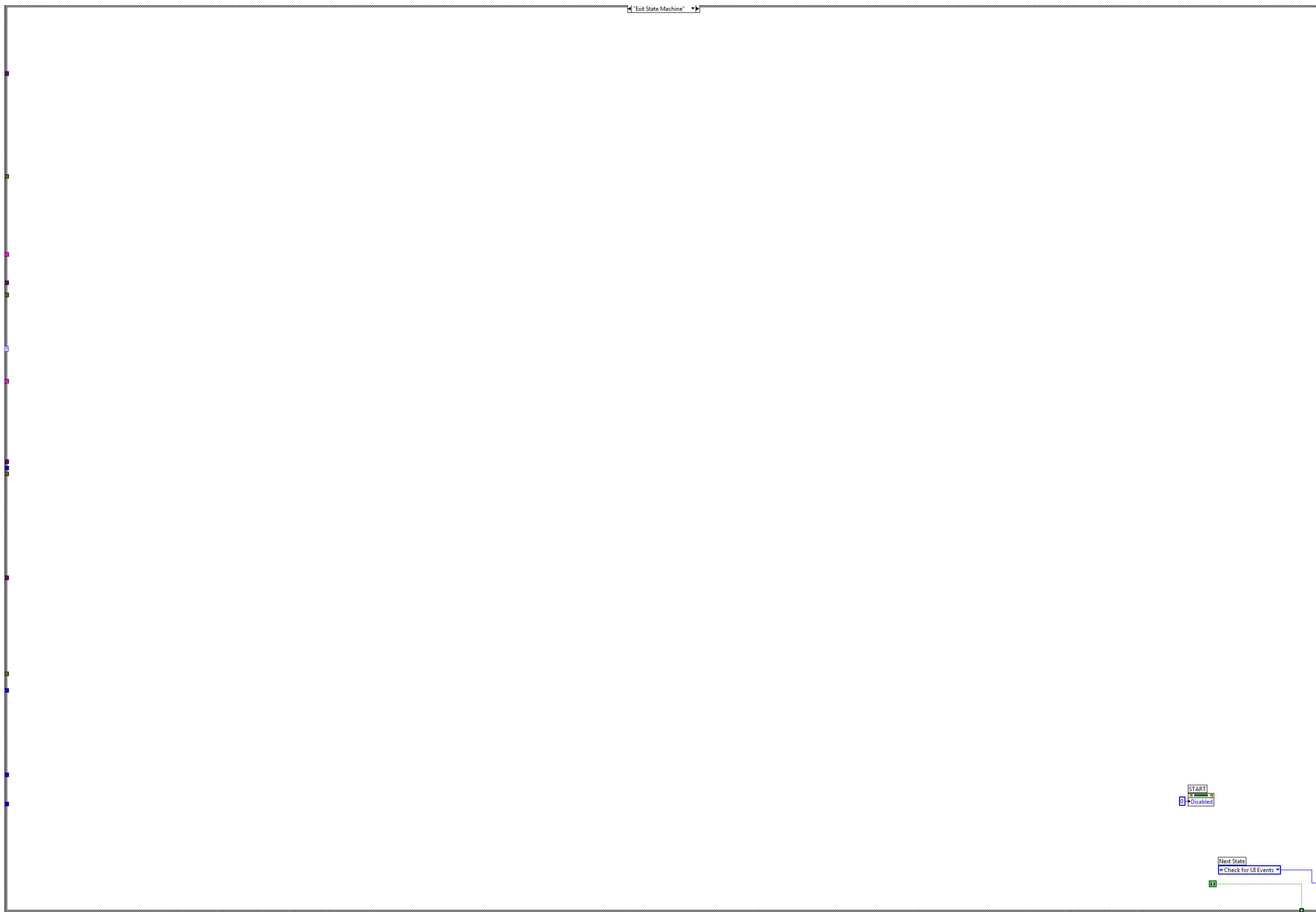


State S5 – Save Data. The software reads input parameters corresponding to desired file type to be saved. The data from both channels is transferred to a sub-vi for saving, and the on-screen indicator updates upon successful saving. If z-axis stack collection is enabled, the stage is sent commands over USB to update stage location.





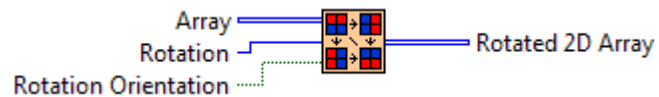
State S6 – Emergency Exit. Emergency stop for instantly quitting the software.  
Implemented for the sake of completeness, but not used within the State Machine.



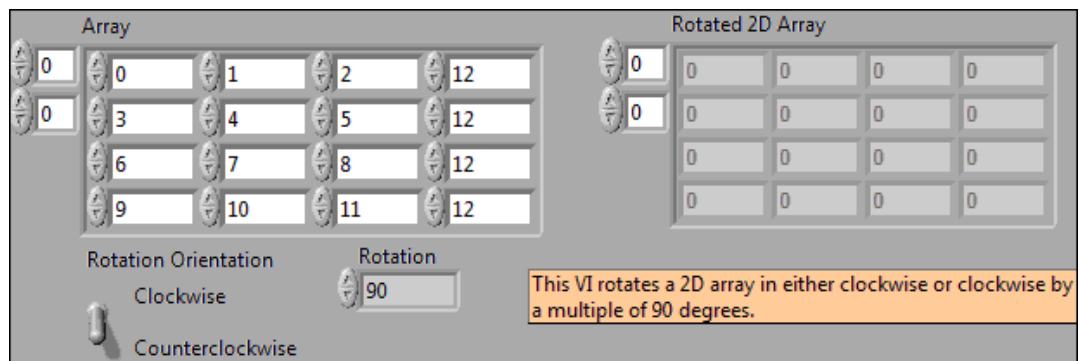
## Rotate2DArray90DegreeMultiple.vi

Pre-existing VI. This VI rotates a 2D array in either clockwise or counter-clockwise by a multiple of 90 degrees.

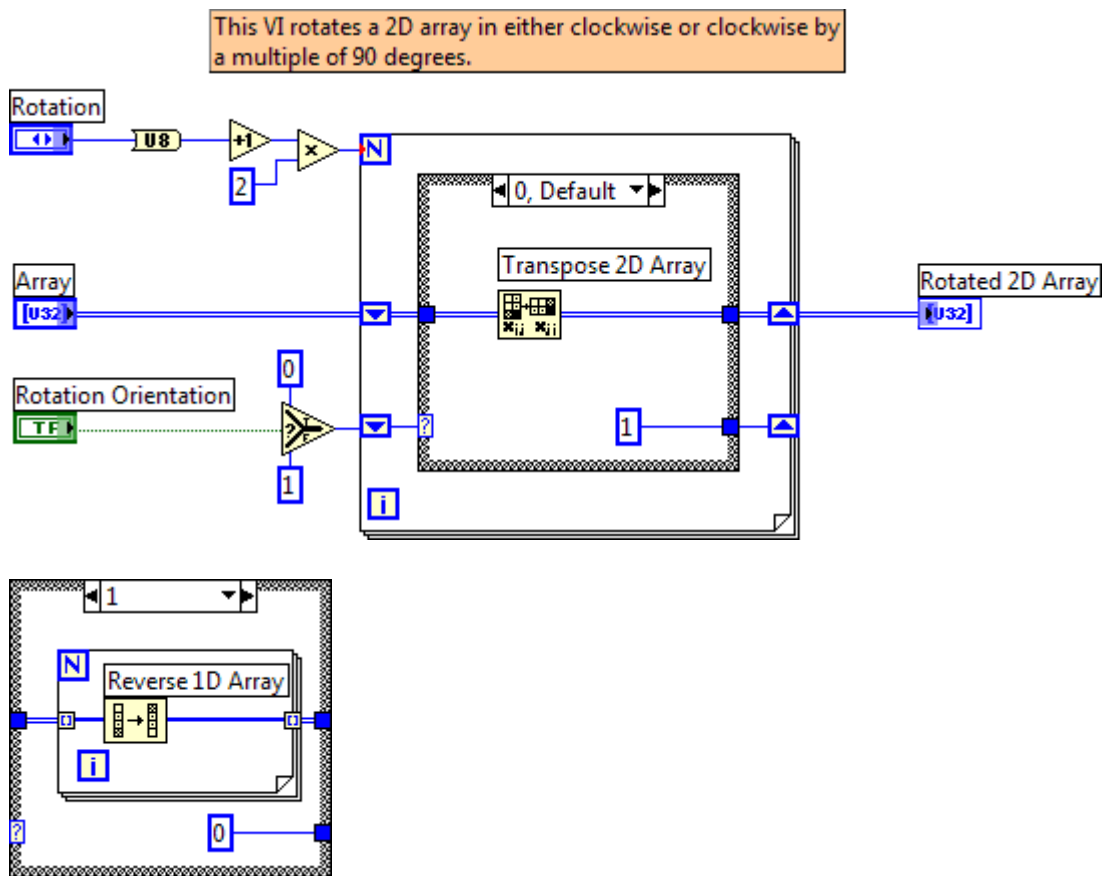
### Connector Pane



### Front Panel



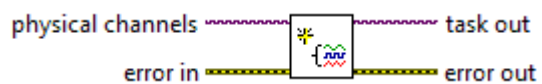
## Block Diagram



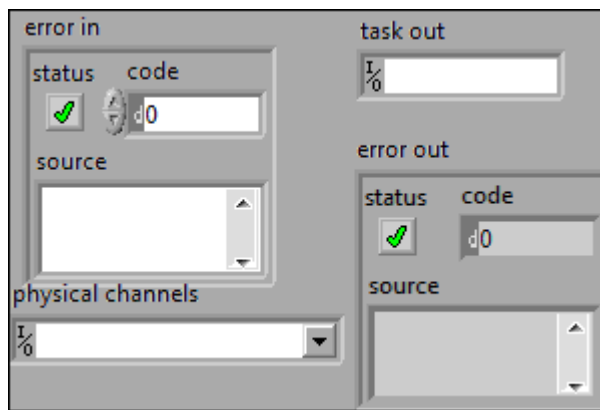
## lasershift.vi

Sub-vi used for laser divergence. Appropriate channels are initialized and activated when divergence is desired.

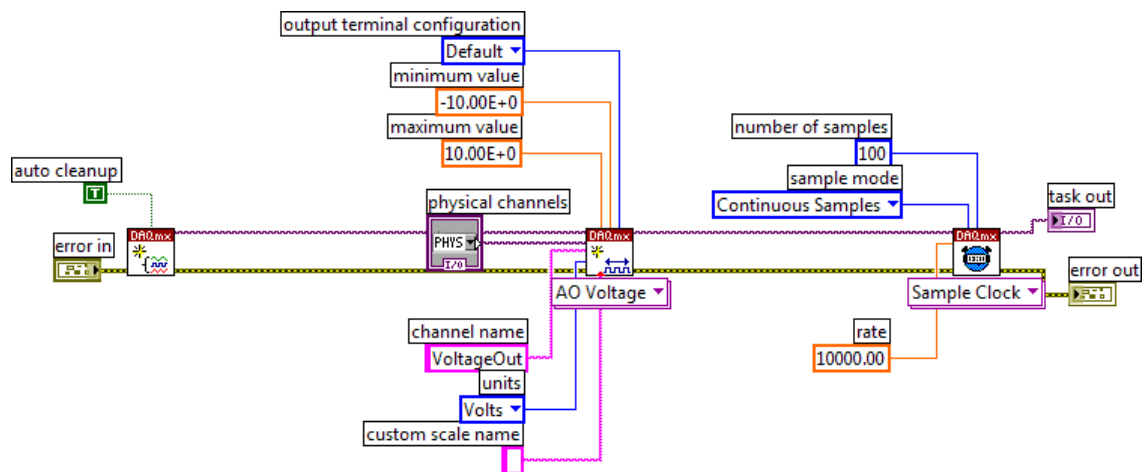
## Connector Pane



## Front Panel



## Block Diagram

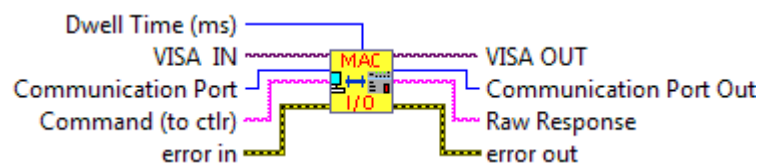


## IOMAC5000.vi

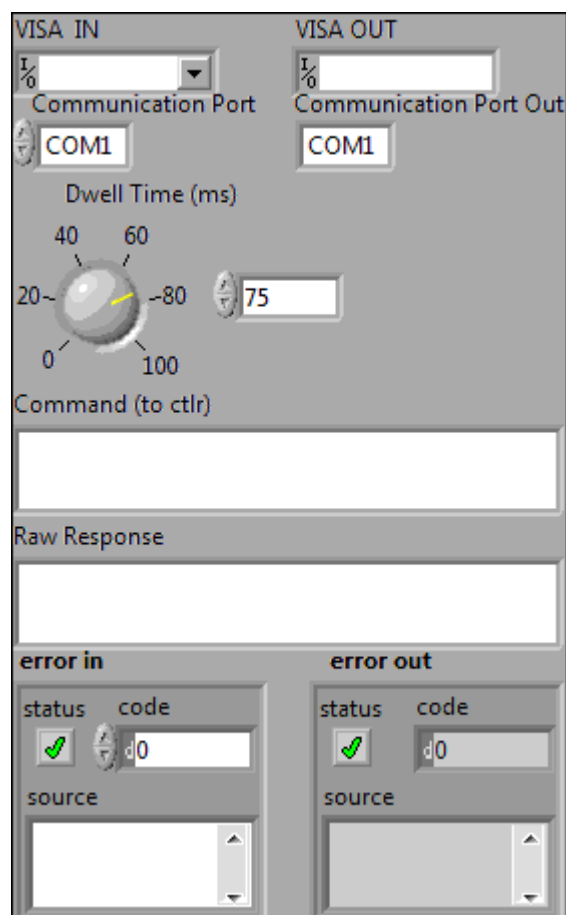
Pre-existing VI. SubVI for sending commands to the MAC5000 and receiving responses from the MAC5000.



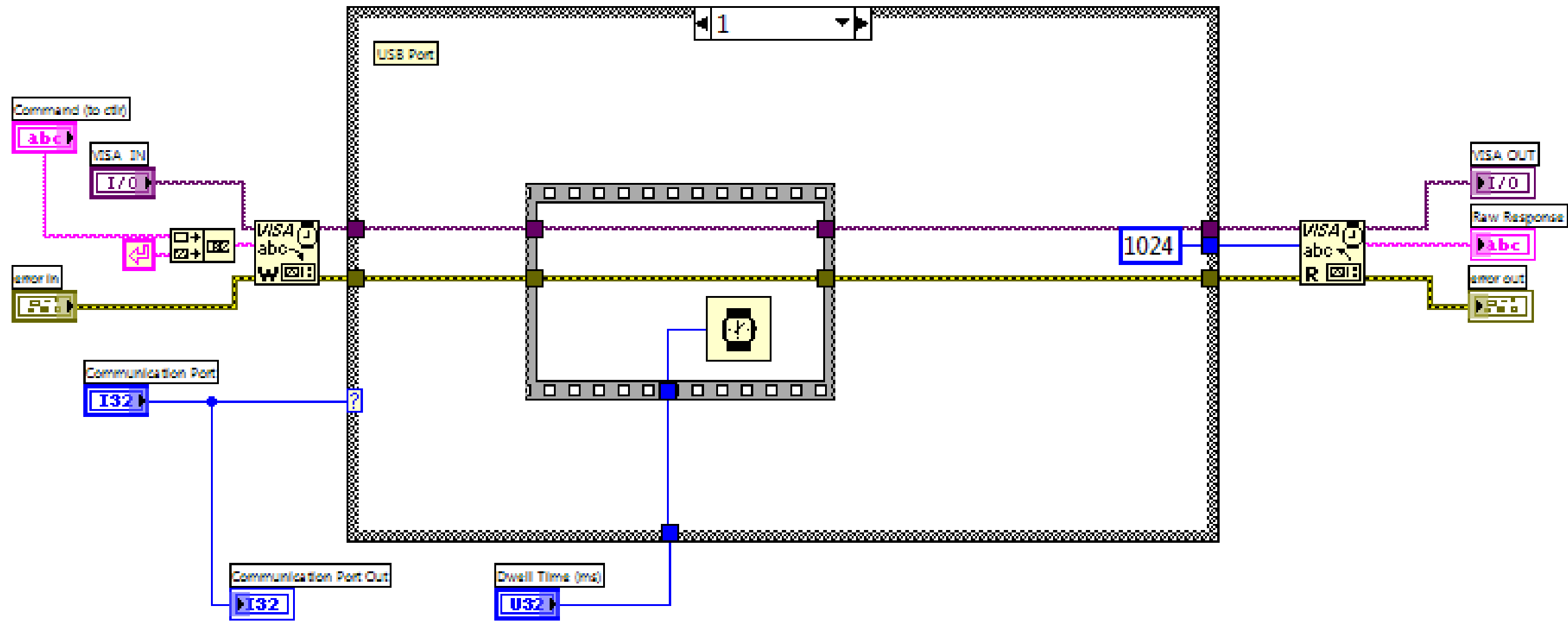
## Connector Pane

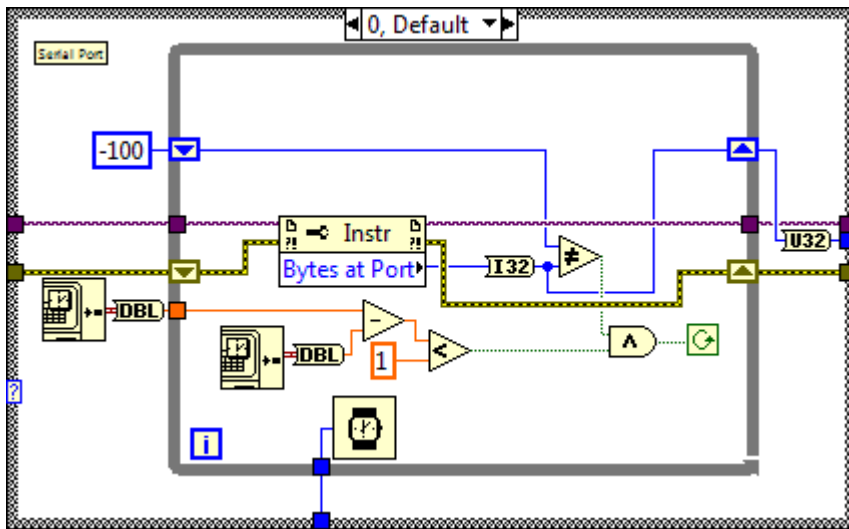


## Front Panel



Block Diagram





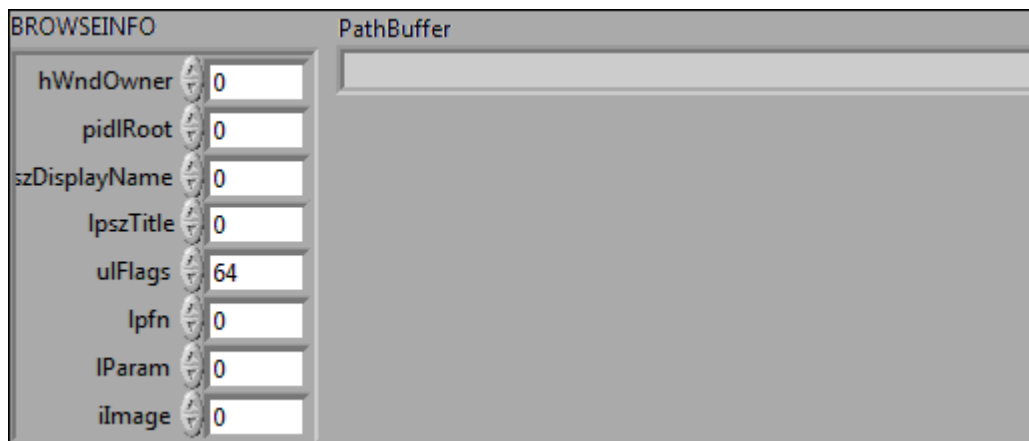
## Browse\_Folders.vi

Pre-existing VI. Sub-vi allows for an on-screen interface for prompting the user to select a folder in the computer.

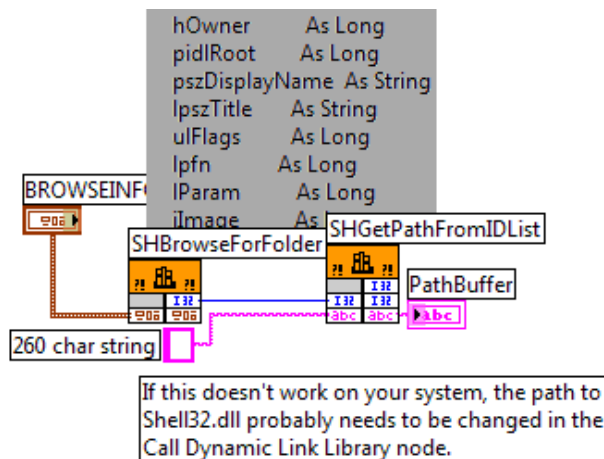
## Connector Pane



## Front Panel



## Block Diagram



### Structure

<http://msdn.microsoft.com/library/default.asp?url=/library/en-us/shellcc/platform/shell/reference/structures/browseinfo.asp>

### Header File

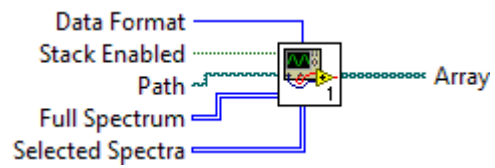
<http://cvs.sourceforge.net/viewcvs.py/mingw/w32api/include/shlobj.h?rev=1.7>

## save data.vi

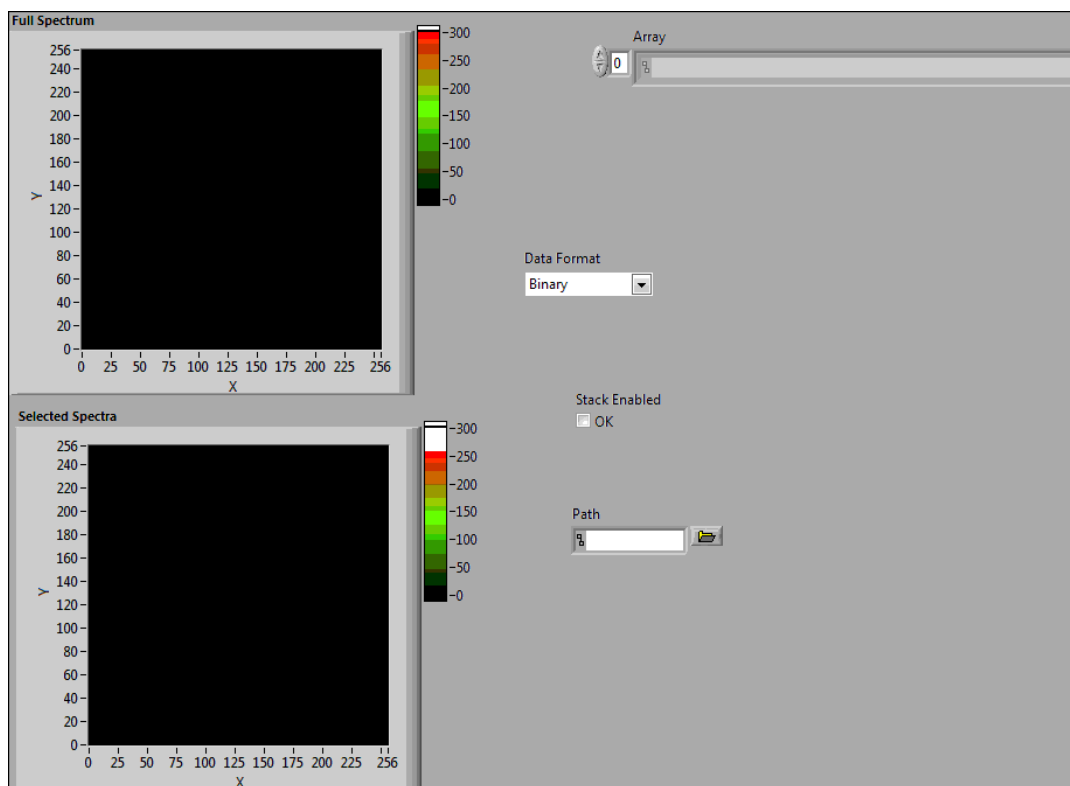
Sub-vi used to save collected data to the hard drive.

---

## Connector Pane

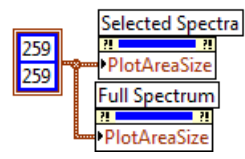
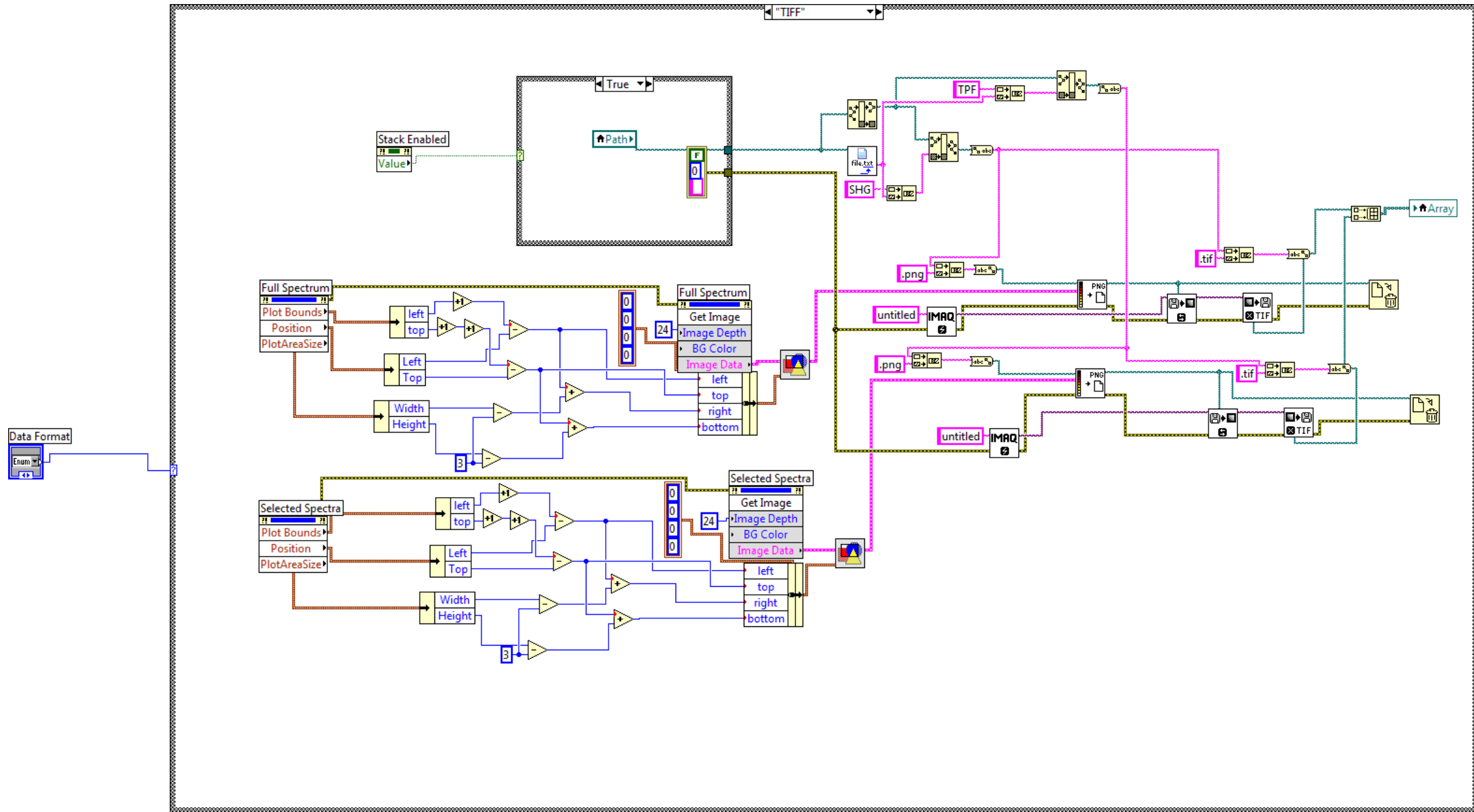


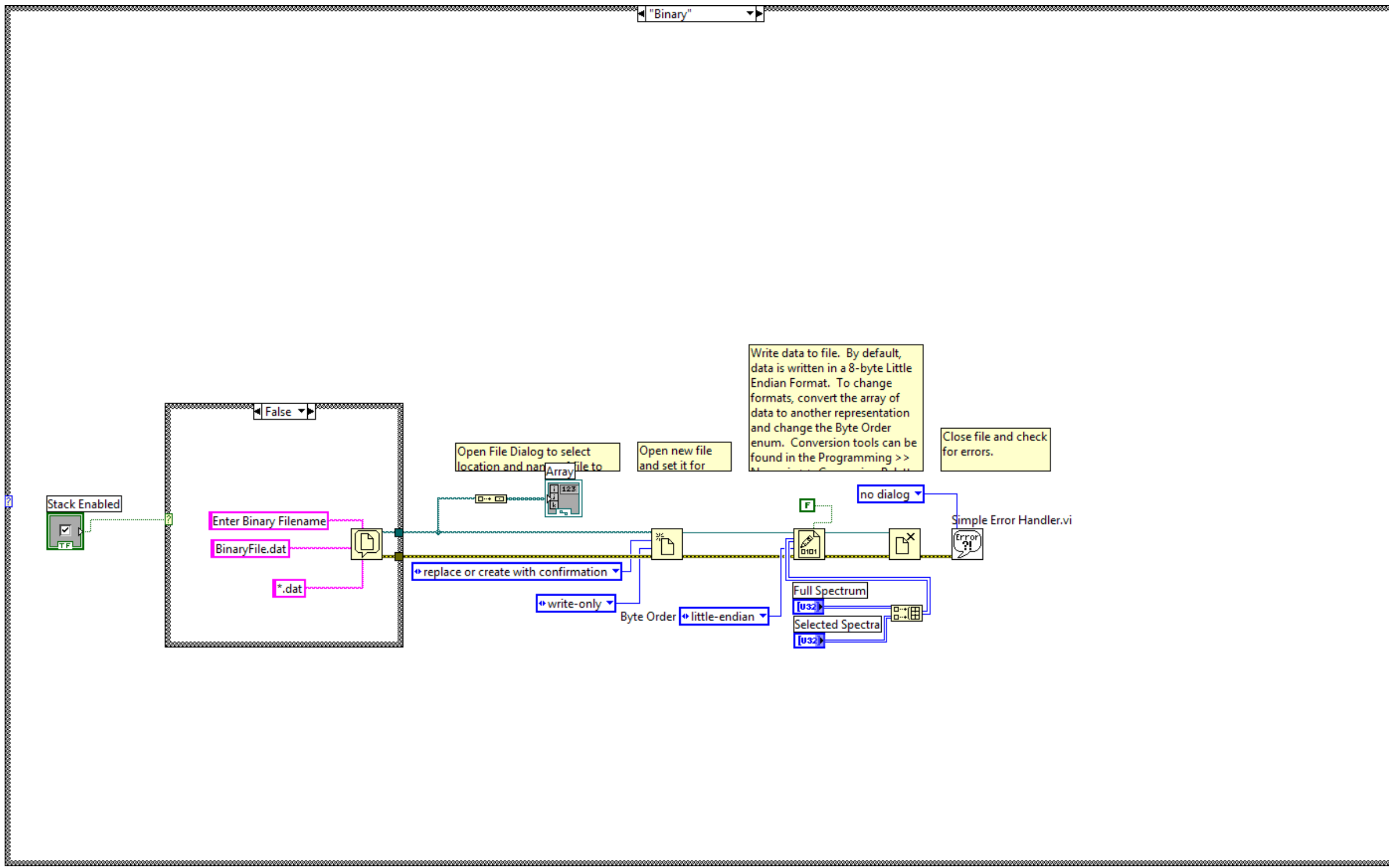
## Front Panel



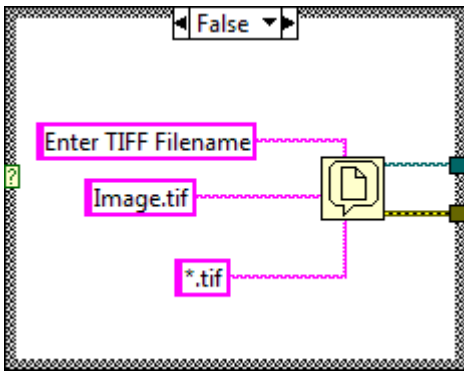
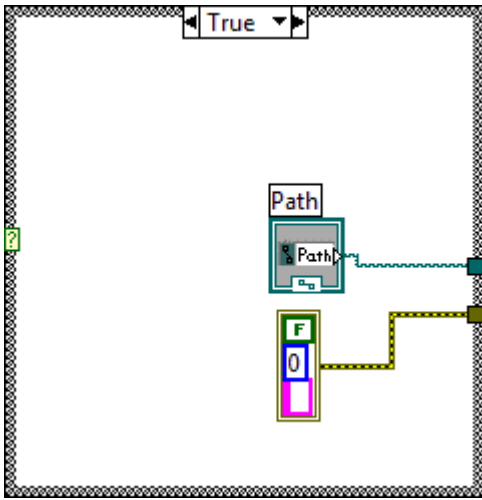
## **Block Diagram**

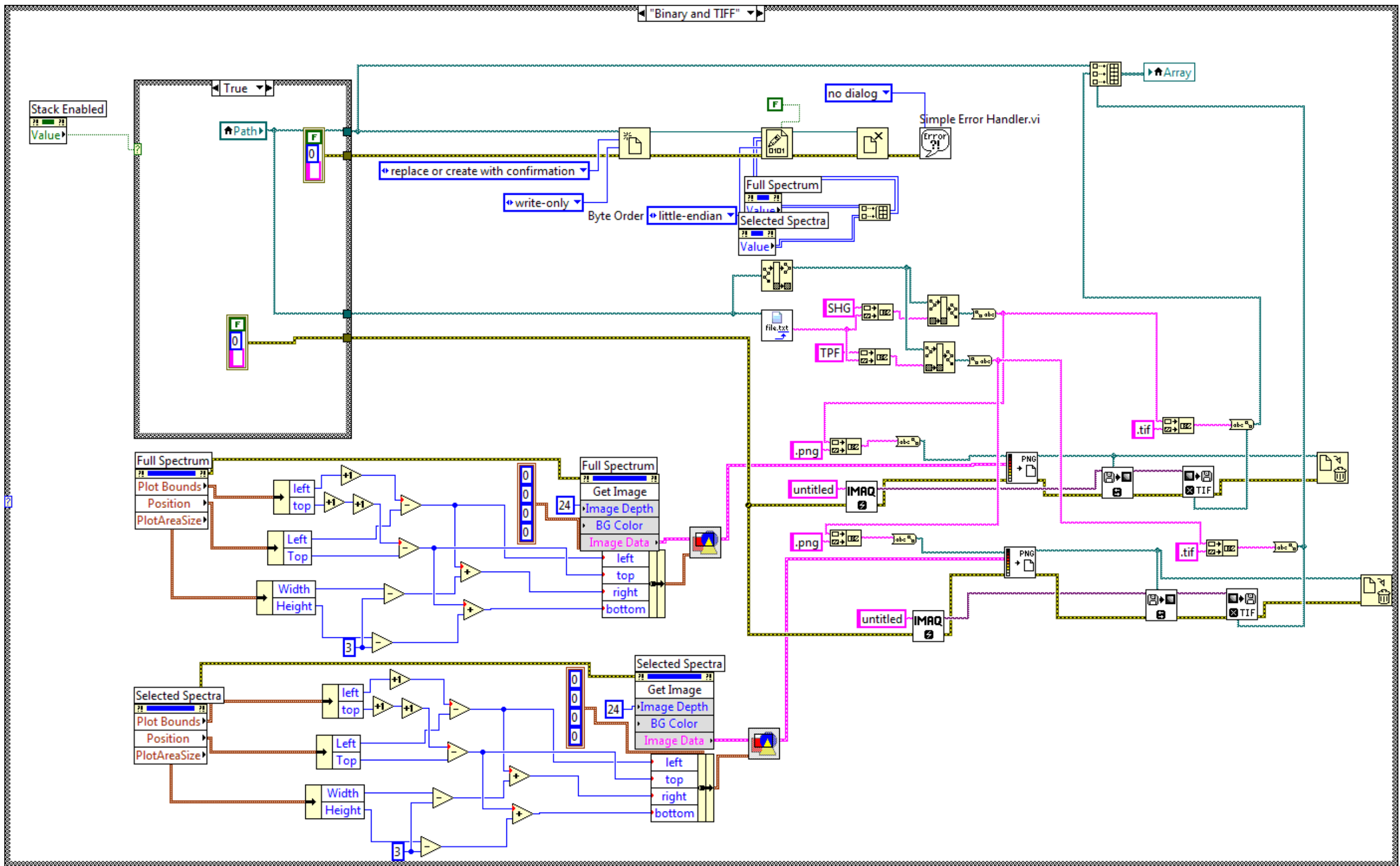
Property nodes are used to identify true boundaries for images. The images are exported into the appropriate format selected by the user.

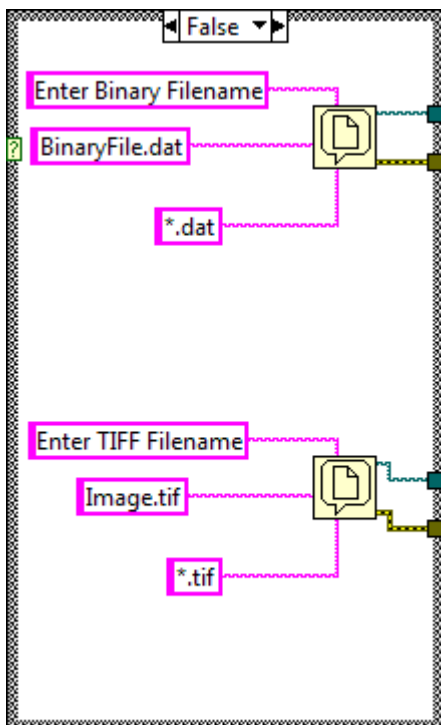













---

## Waveform Buffer Generation.vi

Pre-existing VI. This subVI is used to create a Sine, Square, Triangle or Sawtooth Waveform. The inputs to this VI are the Waveform Type, which determines if the output waveform is a Sine, Square, Triangle, or Sawtooth Waveform, the amplitude, Desired Frequency, Samples per Buffer, and Cycles per Buffer.

The Desired Frequency, Samples per Buffer, and Cycles per Buffer are used to calculate the sample clock rate. The DAQmx Timing property node sets the sample clock rate for the device specified in the task/channels in control.

The actual, coerced, sample clock rate is returned and used as an input to the Basic Function Generator.vi. The Basic Function Generator returns a waveform of data with timing information.

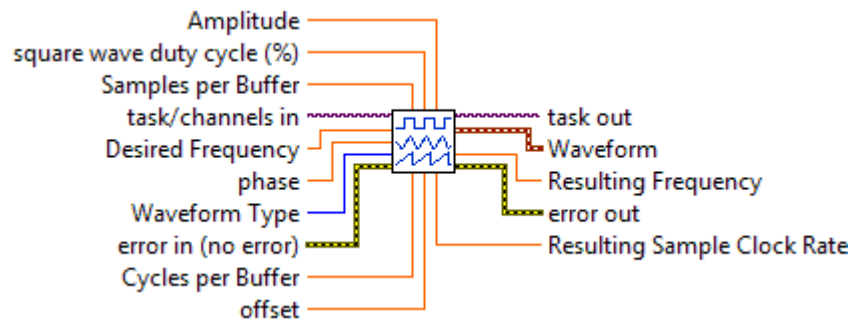
The formula below was used to determine the sample clock rate:

$$\text{Desired Frequency} = [(\text{Cycles/Buffer}) \times (\text{Sample Clock Rate})] / \text{Samples per Buffer}$$

Note: The Block Diagram rearranges the variables to solve for Sample Clock Rate

---

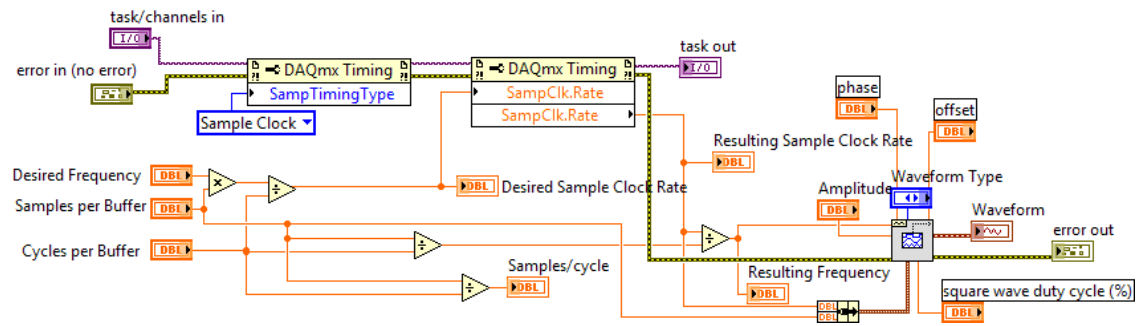
### Connector Pane



## Front Panel

task/channels in	task out												
<input type="text" value="1/0"/>	<input type="text" value="1/0"/>												
Desired Frequency	Resulting Frequency												
<input type="text" value="1000.00"/>	<input type="text" value="0.00"/>												
Samples per Buffer	Desired Sample Clock Rate												
<input type="text" value="1000"/>	<input type="text" value="0.00"/>												
Cycles per Buffer	Resulting Sample Clock Rate												
<input type="text" value="1.00"/>	<input type="text" value="0.00"/>												
Waveform Type	Samples/cycle												
<input type="text" value="Sine Wave"/>	<input type="text" value="0.00"/>												
Amplitude	Waveform												
<input type="text" value="2.00"/>	<table border="1"> <tr> <td><b>t0</b></td> <td><b>Y</b></td> </tr> <tr> <td>00:00:00 PM</td> <td><input type="text" value="0"/></td> </tr> <tr> <td>MM/DD/YYYY</td> <td><input type="text" value="0"/></td> </tr> <tr> <td><b>dt</b></td> <td><input type="text" value="0"/></td> </tr> <tr> <td>0.000000</td> <td><input type="text" value="0"/></td> </tr> <tr> <td></td> <td><input type="text" value="0"/></td> </tr> </table>	<b>t0</b>	<b>Y</b>	00:00:00 PM	<input type="text" value="0"/>	MM/DD/YYYY	<input type="text" value="0"/>	<b>dt</b>	<input type="text" value="0"/>	0.000000	<input type="text" value="0"/>		<input type="text" value="0"/>
<b>t0</b>	<b>Y</b>												
00:00:00 PM	<input type="text" value="0"/>												
MM/DD/YYYY	<input type="text" value="0"/>												
<b>dt</b>	<input type="text" value="0"/>												
0.000000	<input type="text" value="0"/>												
	<input type="text" value="0"/>												
error in (no error)	error out												
status <input checked="" type="checkbox"/> code <input type="text" value="0"/>	status <input checked="" type="checkbox"/> code <input type="text" value="0"/>												
source <input type="text"/>	source <input type="text"/>												
phase													
<input type="text" value="0.00"/>													
square wave duty cycle (%)													
<input type="text" value="50.00"/>													
offset													
<input type="text" value="0.00"/>													

## Block Diagram



## StateMachineStates.ctl

## Connector Pane



## Front Panel



## Initialization.vi

Pre-existing VI. VI initializes and configures the MAC5000; the user chooses whether communication with the MAC5000 occurs over the Serial Port(RS232) or the USB port. This VI should be run once at the beginning of a larger program.

Note:

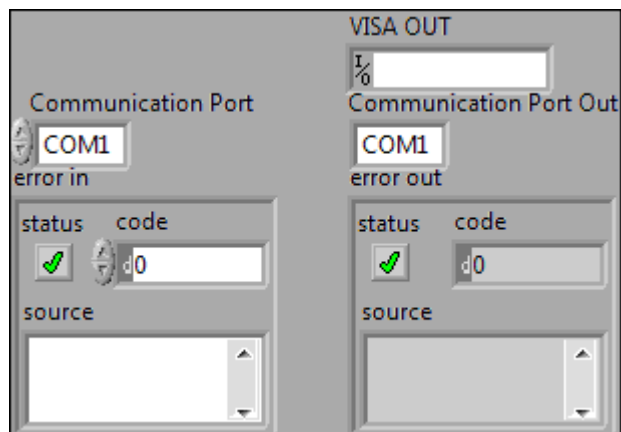
Serial Port communication occurs over Serial Port 1; if the user wants to use a different Serial Port the VISA Resource name needs to be changed in the block diagram from ASRL1::INSTR to ASRL#::INSTR where # is the number of the Serial Port.

To use USB communication, the user needs to set up the VISA protocol using the VISA driver development wizard. After setting up the VISA driver, the user needs to enter the correct VISA resource name in the block diagram. Note the VISA resource name is specific to a particular USB Bus; if the MAC5000 is plugged into another USB bus the user needs to set up the VISA resource name again.

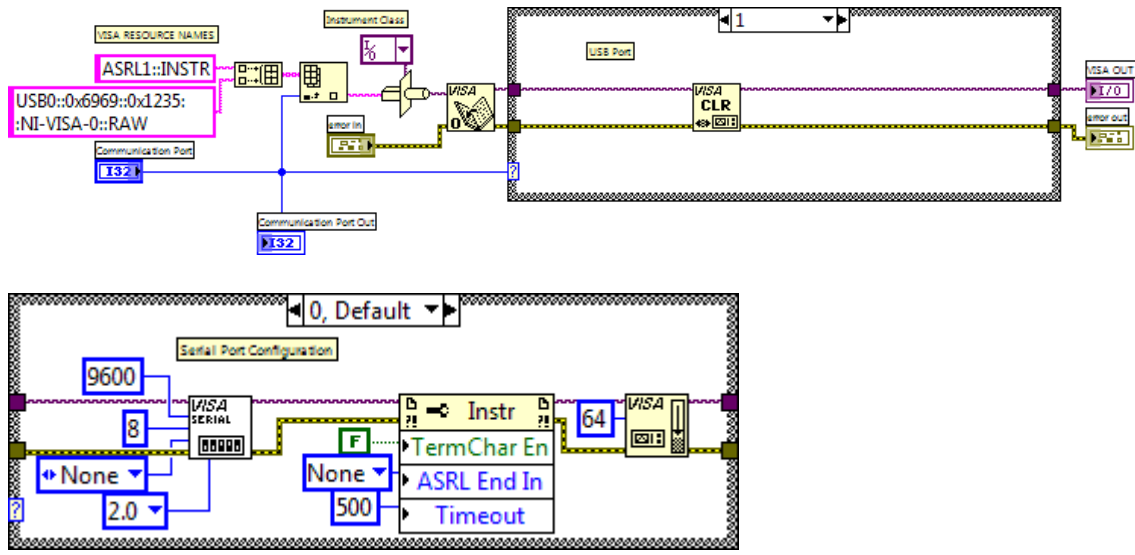
### Connector Pane



### Front Panel



### Block Diagram





## APPENDIX B

### NOM SISV1 SOURCE CODE

Only modifications from NOMS are shown. Code not shown can be assumed to match that of NOMS.

#### **nomsis.vi**

NOM SIS uses an updated front panel with 3 viewing panels, selectable channels, and an on-screen spectrum.

---

#### **Connector Pane**



Front Panel

## NONLINEAR OPTICAL MICROSCOPY SPECTRAL IMAGING SYSTEM

v2.0

Data Acquisition
Data Processing
Revision History
About

Program Status

Connection to Stage Failed...Stack acquisition will not function properly. Check the USB cable and restart the program to reconnect.

START

STOP

Enable Laser Divergence

Export Data

Data Format

Binary and TIFF ▼ SAVE

Scanning Specifications

Field of View (voltage)

Integration Time (seconds)

Continuous Scan  
 Multiple Scans

Scans per Image

Image Stack Parameters

Enable Stack

Step Size

Number of Images

File Start Number

Data Format

Path

Wavelength Selection 1 (nm)

350-368	421-438	491-508	561-578
369-385	439-455	509-525	579-595
386-403	456-473	526-543	596-613
404-420	474-490	544-560	614-630

Wavelength Selection 2 (nm)

350-368	421-438	491-508	561-578
369-385	439-455	509-525	579-595
386-403	456-473	526-543	596-613
404-420	474-490	544-560	614-630

Wavelength Selection 3 (nm)

350-368	421-438	491-508	561-578
369-385	439-455	509-525	579-595
386-403	456-473	526-543	596-613
404-420	474-490	544-560	614-630

Selection 1

Selection 2

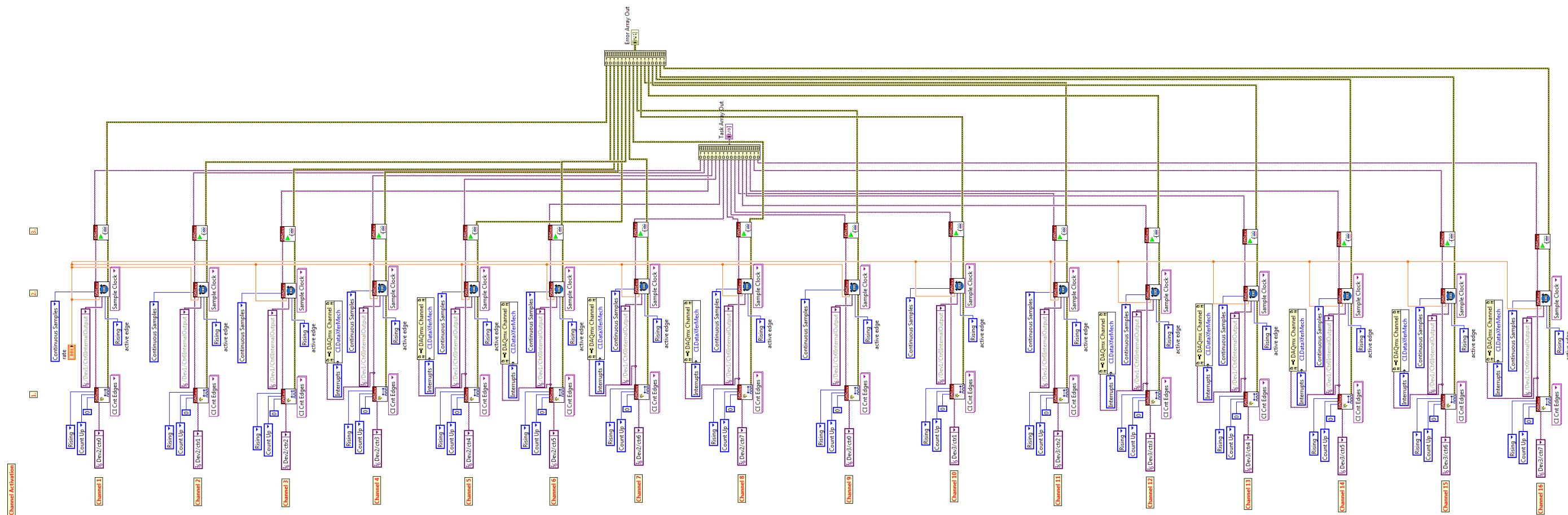
Selection 3

Connect remotely: <http://yehgx280-3.tamu.edu/nomsis.html>

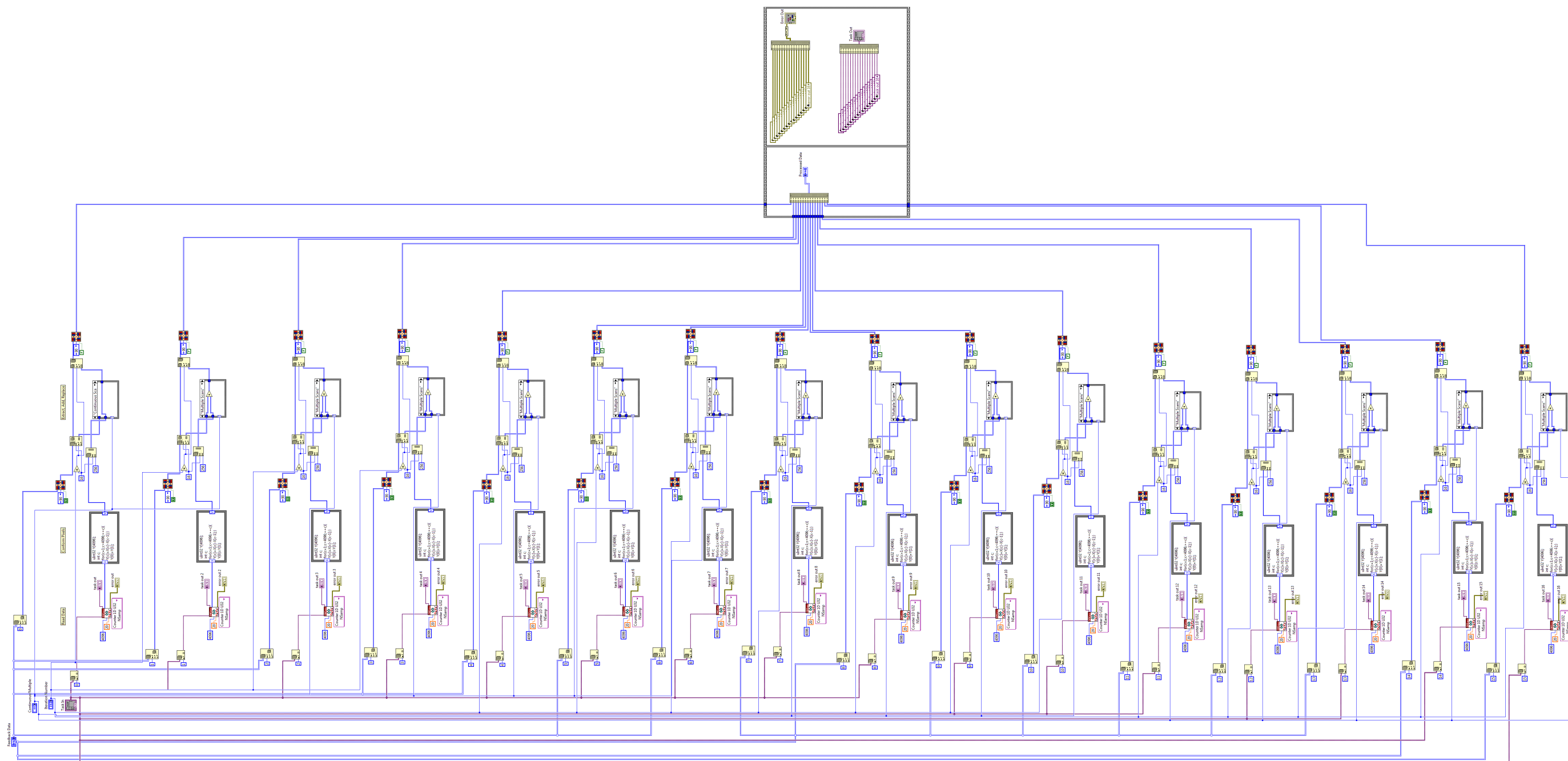
Optimized for 1280x1024 screen resolution

## **Block Diagram**

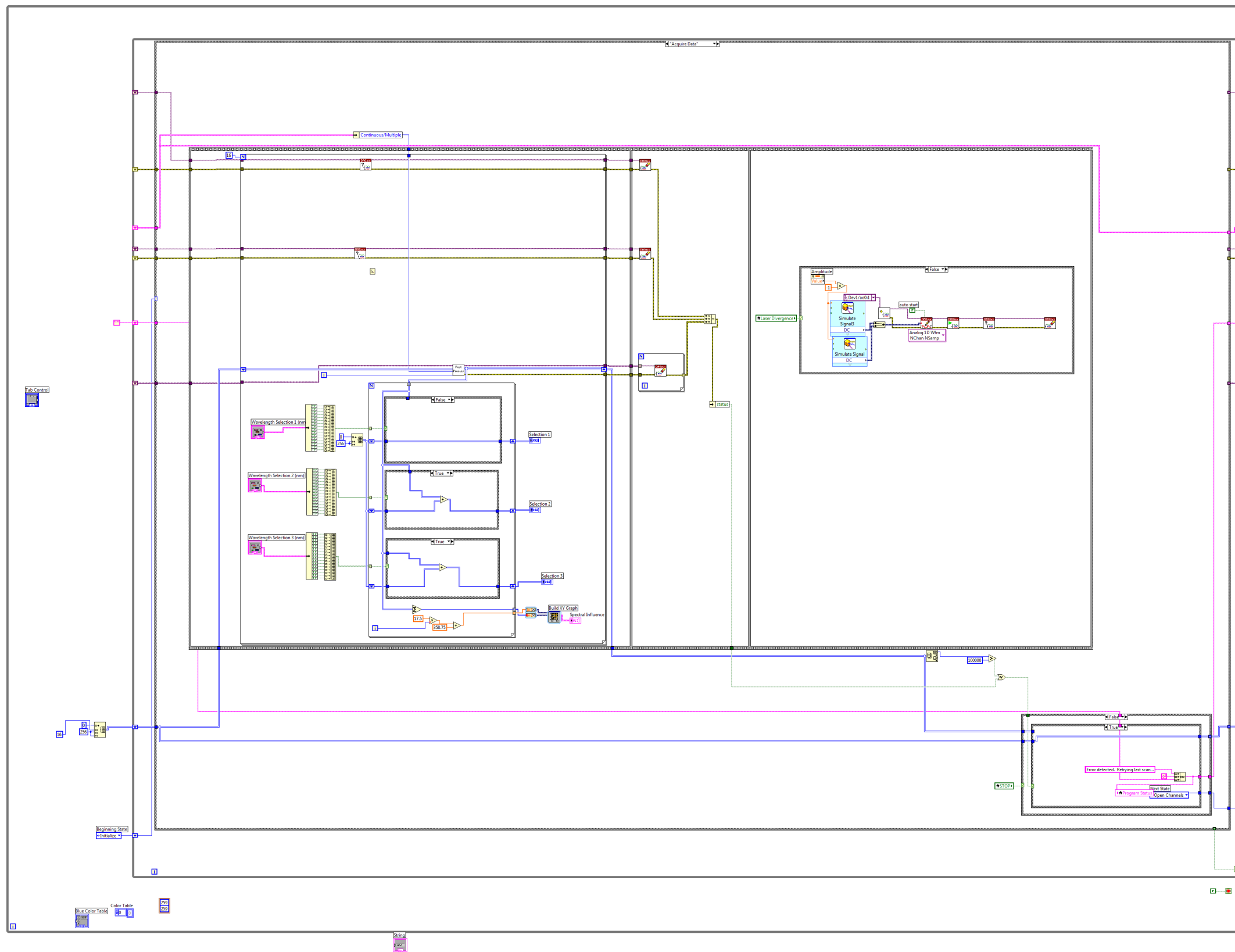
Modification to State S2 – Initialize Channels. Code for channel activation is replicated to activate all channels of both counter cards. Acquisition method changed from DMA to Interrupt to prevent buffer overflow errors.



Modification to State S3 – Acquire Data. Data is acquired from all 16 channels of the counter card. Using the same code as NOMS, the code is replicated with the only change being the corresponding channel number. The data is compiled together as a 3-dimensional array before exiting the sub-vi.



Based on the array of channels selected on the front panel, only the active indices of the array are pulled out and integrated together. Summed data is then shown on-screen.



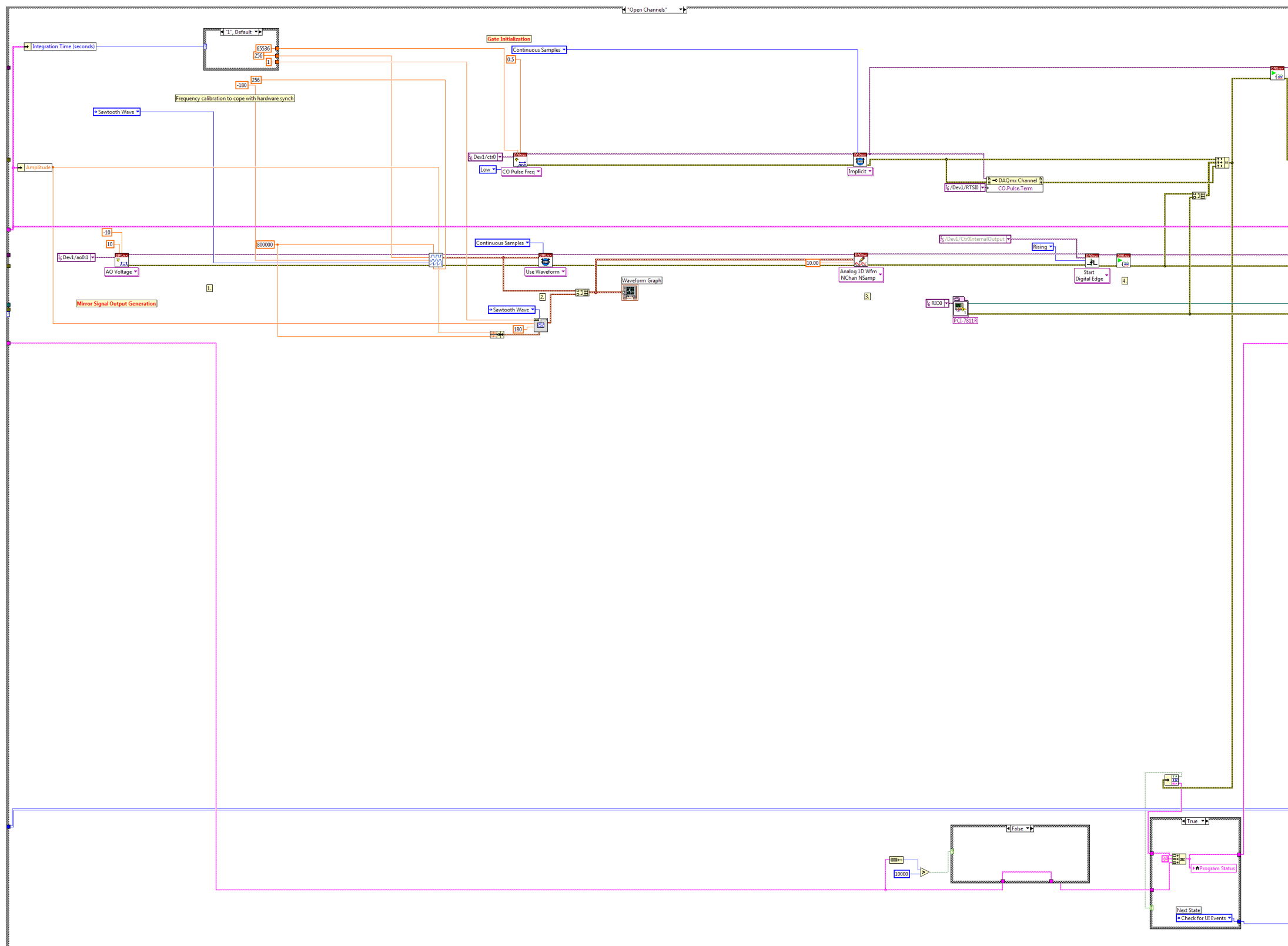


## **APPENDIX C**

### **NOMISISV2 SOURCE CODE**

Only modifications from NOMISISv1 are shown. Code not shown can be assumed to match that of NOMISISv1.

Modification to State S2 – Activate Channels. Pixel clock is transferred to the FPGA via RTSI channel. FPGA reference is opened instead of activating any counters.

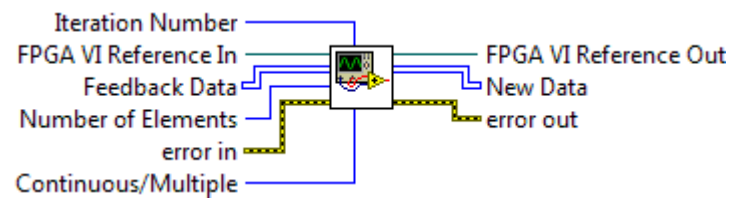


## FPGAread.vi

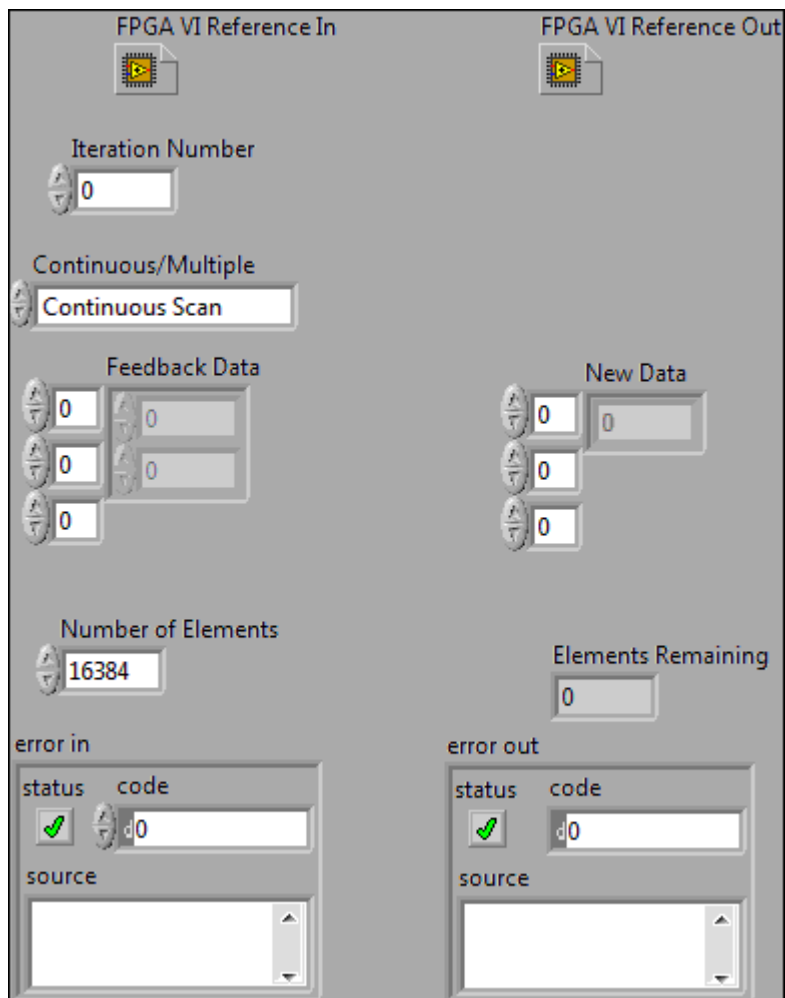
Sub-vi used to acquire and process pulses from the FPGA data stack. This sub-vi replaces the one for data processing in NOMSISv1.

---

### Connector Pane

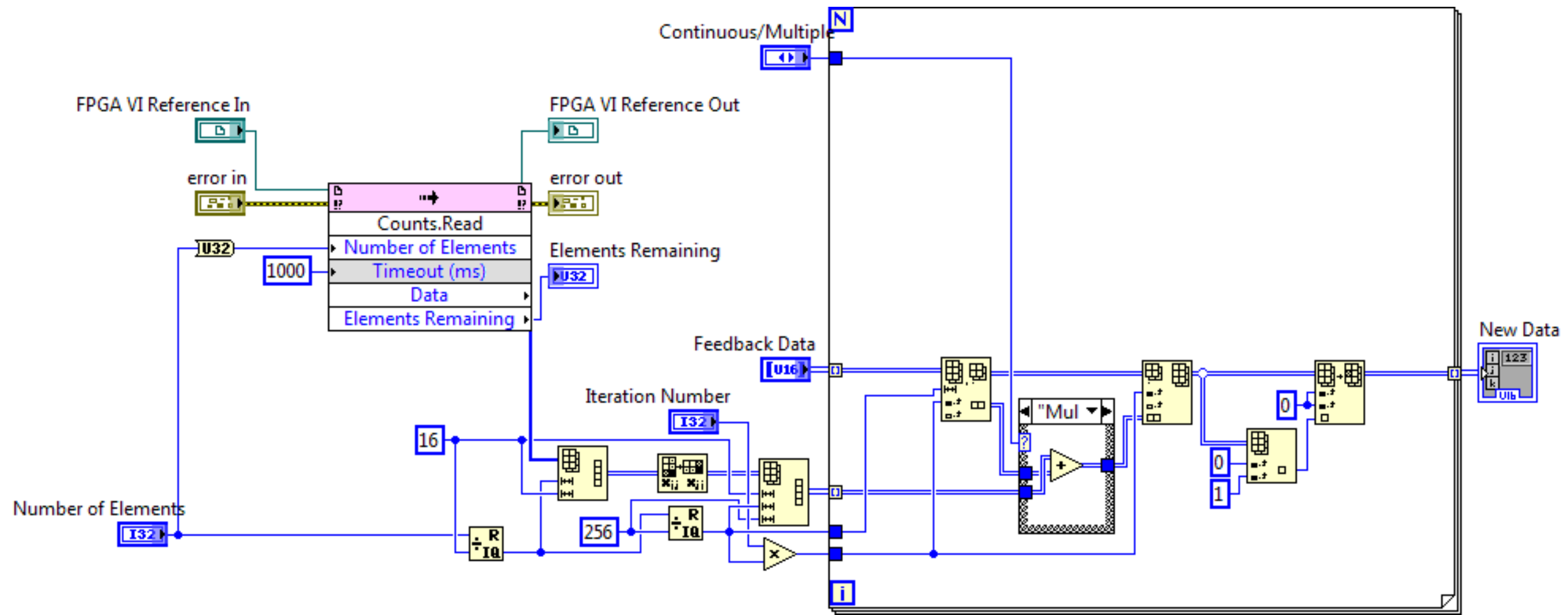


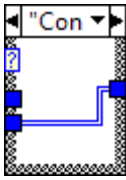
## Front Panel



## Block Diagram

Acquiring data within FPGA is simplified due to the usage of a data stack. The Invoke Node pulls data from the stack and immediately processes it into a NOMSIS 3-dimensional array.

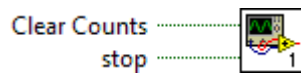







---

## FPGACount16.vi

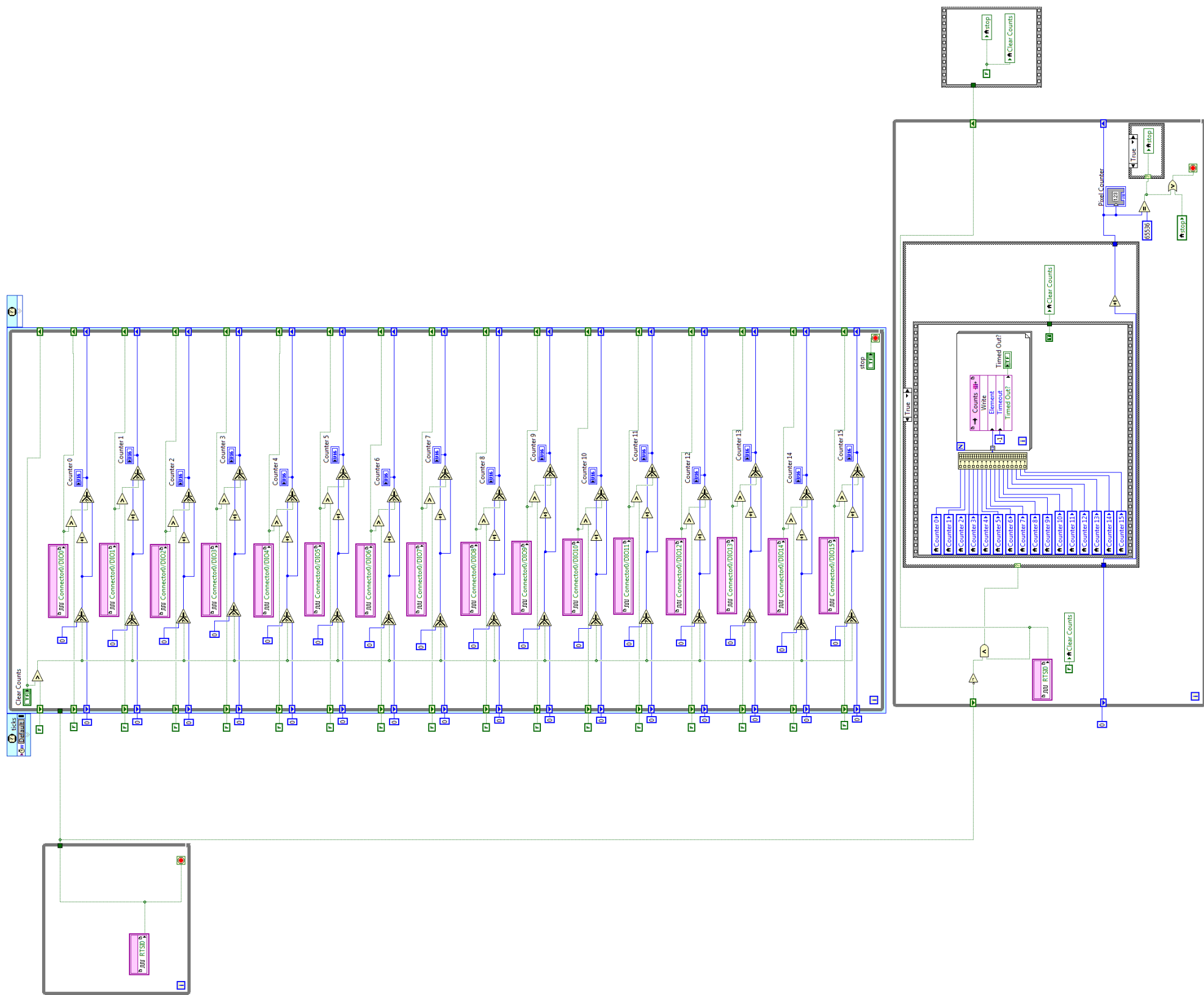
FPGACount16.vi represents the source code used for synthesis into the HDL bitfile. Once compiled, the bitfile is stored on the hard drive and acts as a standalone representation of the source code. The code is referenced directly by State S2.

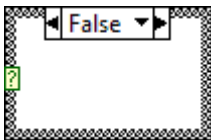
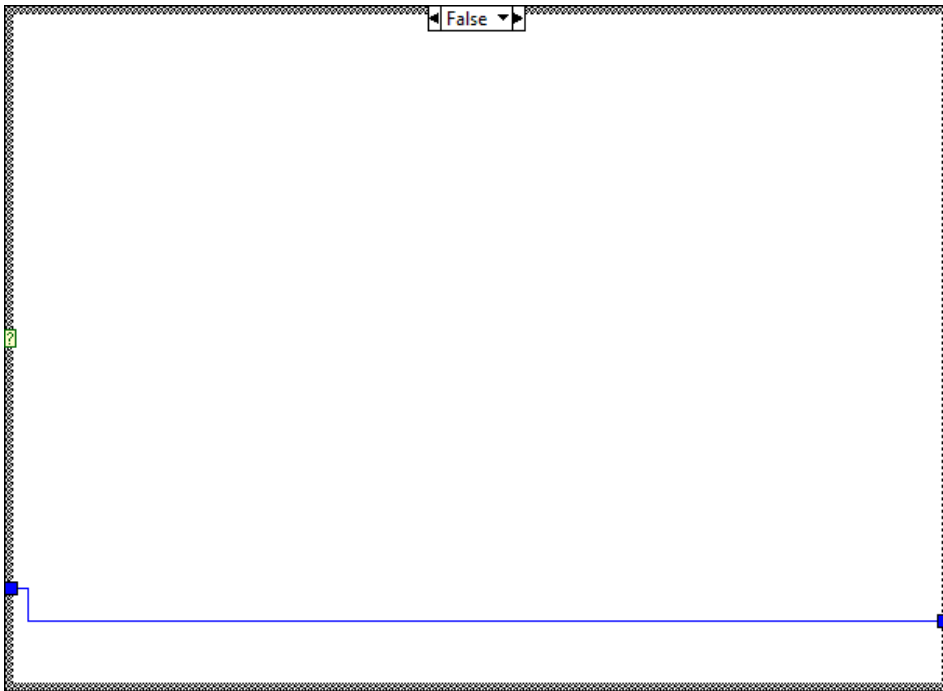


Counter 0	<input type="text" value="0"/>	
Counter 1	<input type="text" value="0"/>	
Counter 2	<input type="text" value="0"/>	
Counter 3	<input type="text" value="0"/>	
Counter 4	<input type="text" value="0"/>	Clear Counts
Counter 5	<input type="text" value="0"/>	
Counter 6	<input type="text" value="0"/>	Pixel Counter
Counter 7	<input type="text" value="0"/>	<input type="text" value="0"/>
Counter 8	<input type="text" value="0"/>	Timed Out?
Counter 9	<input type="text" value="0"/>	
Counter 10	<input type="text" value="0"/>	stop
Counter 11	<input type="text" value="0"/>	
Counter 12	<input type="text" value="0"/>	
Counter 13	<input type="text" value="0"/>	
Counter 14	<input type="text" value="0"/>	
Counter 15	<input type="text" value="0"/>	

The FPGA receives trigger signal sent over RTSI from the DAQ card. Upon activation, the FPGA-based digital lines act as pulse counters by comparing for pulse transitions as mentioned within the text. Upon each rising edge of the pixel clock, the current value of the counter is stored into the FPGA data stack and reset to zero.







## VITA

Anthony Chien-der Lee received his Bachelor of Science degree in electrical engineering from The University of Texas at Austin in 2004. Shortly afterwards, he entered the graduate program in May 2005 at Texas A&M University in College Station. He received his Doctor of Philosophy degree in biomedical engineering in August 2011, and will enter the Master of Business Administration program in the Mays Business School immediately afterwards. His research interests include medical instrumentation and imaging systems. He plans on entering the medical device industry upon completion of his education.

Mr. Lee may be reached at 337 Zachry Engineering Center, Biomedical Engineering, 3120 TAMU, College Station, TX 77843-3120. His cellular number is 713-261-3841, and e-mail address is AntLee29@gmail.com.